Julia Kohlbacher, BSc

Analysis of phosphorylation sites of ATGL regulators CGI-58 and G0S2

MASTERARBEIT

zur Erlangung des akademischen Grades

Master of Science

Masterstudium Biochemie und Molekulare Biomedizin

eingereicht an der

Technischen Universität Graz

Betreuerin

Assoz. Prof. Priv.-Doz. Dipl.-Ing. Dr.techn. Ruth Birner-Grünberger

Institut für Pathologie

Medizinische Universität Graz

Graz, November 2019

EIDESSTATTLICHE ERKLÄRUNG

Ich erkläre an Eides statt, dass ich die vorliegende Arbeit selbstständig verfasst, andere als die angegebenen Quellen/Hilfsmittel nicht benutzt, und die den benutzten Quellen wörtlich und inhaltlich entnommenen Stellen als solche kenntlich gemacht habe. Das in TUGRAZonline hochgeladene Textdokument ist mit der vorliegenden Masterarbeit identisch.

Datum

Unterschrift

Acknowledgments

First and foremost, I would like to thank my thesis advisor Dr. Ruth Birner-Grünberger for her continuous support, guidance and most of all her patience throughout my time working in her team. Her positive attitude and the professional, but also very warm working environment gave me an insight into various research subjects and broadened my horizon regarding countless analysis techniques.

I would like to thank Laura Liesinger, Tamara Tomin, Anita Sahu-Osen, Petra Krenn, Barbara Darnhofer, Stefan Spörk and Matthias Schittmayer-Schantl for their help with my many questions in the lab and for providing their constant support. Special thanks go to Jürgen Gindlhuber for his assistance and continuous support throughout all the microscopy experiments, which would not have been possible without him.

Last but not least, I am very grateful for my friends and family, who stood beside me through this experience and encouraged me in every way possible to complete this task.

Abstract

The term lipolysis describes the three-step process of the complete hydrolysis of triacylglycerides to three non-esterified fatty acids (NEFA) and glycerol that displays one of the most important ways to supply the body with energy in form of NEFA. Adipose triglyceride lipase (ATGL), the predominant triacylglyeride lipase in adipocytes, catalyzes the first and rate-limiting step in lipolysis and its activity is regulated by two proteins: Comparative Gene Identification 58 (CGI-58) and G0/G1 switch Gene 2 (G0S2). Consequentially, these two proteins display important switches concerning lipolysis control and worthwhile research objects to shed light on the complex regulation methods of lipolysis. The main aim of this thesis is investigating the influence of the phosphorylation site (S239) and docking site (Y330) of CGI-58 on CGI-58's subcellular localization.

The first part of this thesis provides a theoretical background by giving an overview of the properties of several major proteins involved in lipolysis (CGI-58, G0S2, Perilipin 1/5 and ATGL) as well as analyzing selected literature regarding their role and impact on lipolysis regulation. Subsequently, in the first experimental part of the thesis, the generation of various mutated versions of CGI-58, G0S2, Plin1, Plin5 and ATGL via site-directed mutation for following experiments is described in detail. The second part describes the analysis of COS-7 cells expressing different mutated variants of CGI-58 in combination with Plin1 via fluorescence- and immunofluorescence microscopy regarding their subcellular localization. Finally, an approach is made to examine CGI-58's phosphorylation state after incubation with different kinases (PKA/PKG) via LC/MS experiments, focusing on phosphorylation site Ser239, as it is speculated that the phosphorylation state of CGI-58 has an impact on its capability to activate lipolysis.

Although this study has only provided preliminary results, all used methods were critically examined, and troubleshooting as well as further approaches are discussed in detail.

Zusammenfassung

Als Lipolyse bezeichnet man den Vorgang des vollständigen Abbaus von Triacylglyceriden zu freien Fettsäuren und Glycerol, um den Körper mit Energie in Form dieser Fettsäuren zu versorgen. Adipozyten-Triglycerid-Lipase (ATGL) katalysiert den ersten und geschwindigkeitsbestimmenden Schritt der Lipolyse, den Abbau von Triacylglyceriden zu Fettsäuren und Diacylglyceriden. Comparative Gene Identification 58 (CGI-58) und G0/G1 switch Gene 2 (G0S2) stellen als Regulatoren von ATGL essentielle Kontrollpunkte in der Lipolyse dar und werden somit zu wichtigen Forschungsobjekten, um den Prozess der Lipolyse vollständig aufzuklären.

Zu Beginn dieser Arbeit wird versucht, mit Hilfe von Literatur auf dem neuesten Stand der Forschung einen guten theoretischen Überblick über die Eigenschaften eigener Proteine (CGI-58, G0S2, Perilipin 1/5, ATGL) und deren Einflüsse auf den Prozess der Lipolyse zu geben. Das Hauptziel dieser Masterarbeit ist es, den Einfluss einer möglichen Phosphorylierungsstelle (S239) und einer Bindungsstelle (Y330) von CGI-58 auf die subzelluläre Lokalisation des Proteins zu untersuchen. Dies sollte über die Co-Expression verschiedener mutierter CGI-58 Konstrukte mit Perilipin 1 (Plin1) in COS-7 Zellen und deren darauffolgende Untersuchung via Fluoreszenz- oder Immunofluoreszenz-mikroskopie erreicht werden und wird in Teil 2 dieser Arbeit detailliert diskutiert. Der erste praktische Teil der Arbeit beschäftigt sich mit der Einführung von Mutationen in CGI-58-, G0S2-, Plin1-, Plin5- und ATGL- Wildtyp- Gene mit Hilfe von „site-directed mutation kits“. Abschließend wurde die Phosphorylierung von CGI-58 durch zwei verschiedene Kinasen (PKA und PKG) mittels LC/MS Analysen untersucht, da der Einfluss der Phosphorylierung von CGI-58 auf die Aktivierung der Lipolyse seit Jahren das Interesse der Forschung erweckt. Dabei wurde spezielles Augenmerk auf die Phosphorylierungsstelle Ser239 gelegt.

Obwohl diese Arbeit nur vorläufige Ergebnisse geliefert hat, wurde darauf geachtet, alle Methoden, sowie Troubleshooting und den Zugang zu Folgeexperimenten genauestens zu diskutieren.

Abbreviations

ABC	Ammonium bicarbonate
ABHD5	Alpha-beta hydrolase domain-containing 5 (see also CGI-58)
Akt	Protein kinase B
ATGL/mATGL	Adipose triglyceride lipase / murine Adipose triglyceride lipase
ATP	Adenosine triphosphate
BAT	Brown adipose tissue
BAY	BAY 59-9435 (HSL inhibitor)
BiFC	Bimolecular Fluorescence Complementation
Bis-Tris	Bis(2-hydroxyethyl)amino-tris(hydroxymethyl)methane
BMI	Body Mass Index
BSA	Bovine Serum Albumin
cAMP	3',5'-cyclic adenosine monophosphate
cDNA	Complementary DNA
CGI-58/mCGI-58	Comparative Gene Identification 58 / murine CGI-58
cGMP	3',5'-cyclic guanosine monophosphate
COPI	Coat Protein Complex I
COS-7 cells	CV-1 in Origin with SV40 (kidney cells of Cercopitheous arthiops)
cRAP	Common Repository of Adventitious Protein
Da	Dalton
DAG	Diacylglycerol
DMEM	Dulbecco's Modified Eagle's Medium
DTT	Dithiothreitol
E. coli	Escherichia coli
EDTA	Ethylenediaminetetraacetic acid
FA	Fatty acid
FABP	Fatty acid binding protein
FRET	Förster Resonance Energy Transfer
G0S2/mG0S2	G0/G1 switch Gene 2 / murine G0/G1 switch Gene 2
GaAsP	Gallium arsenide phosphide

HPLC	High Performance Liquid Chromatography
HSL	Hormone sensitive lipase
IAA	iodoacetamide
IBMX	3-Isobutyl-1-methylxanthin
IgG	Immunoglobulin G
kDa	Kilodaltons
LB-Agar	Luria Bertani-Agar
LC	Liquid chromatography
LC-MS	Liquid chromatography - mass spectrometry
LC-MS/MS	Liquid chromatography - tandem mass spectrometry
LD	Lipid droplet
LDS	Lithium dodecyl sulfate
LSDAP	Lipid storage droplet protein (see also Plin5)
m/z	Mass to charge ratio
MAG	Monoacylglycerol
MALDI-TOF	Matrix-assisted laser desorption/ionization - Time of flight
MGL	Monoacylglycerol lipase
MOPS	3-(N-morpholino) propane sulfonic acid
MS	Mass spectrometry
NCBI	National Center for Biotechnology Information
NEFA	Non-esterified fatty acid
NLSD-I	Neutral lipid storage disease with ichthyosis
NSLD	Neutral lipid storage disease
NSLD-M	Neutral lipid storage disease with myopathy
OPA1	Optic atrophy 1
OXPAT	PAT-protein expressed in highly oxidative tissue (see also Plin5)
PAT	Perilipin, ADRP and TIP47
PBS	Phosphate-buffered saline
PCR	Polymerase Chain Reaction
PDE3B	Phosphodiesterase 3b

PKA	cAMP-dependent protein kinase
PKG	cGMP-dependent protein kinase
Plin/mPlin	Perilipin/ murine Perilipin
PMT	Photomultiplier tube
PNPLA	Patatin-like phospholipase domain containing
PSM	Peptide spectrum match
PTM	Post Translational Modification
RCF	Relative Centrifugal Force
RPM	Revolutions per minute
RSLC	Rapid Separation Liquid Chromatography
RT	Room Temperature
SDM	Site-directed mutagenesis
SDS	Sodium dodecyl sulfate
SDS-PAGE	Sodium dodecyl sulfate polyacrylamide gel electrophoresis
T2DM	Type 2 diabetes mellitus
TAG	Triacylglycerol
TCA	Trichloroacetic acid
TD	Transmission detector
TEV	Tobacco Etch Virus
TFA	Trifluoroacetic acid
TIP47	Tail-interacting protein of 47 kDa
Tris	Tris(hydroxymethyl)aminomethane
UCP1	Uncoupling Protein 1
WAT	White Adipose Tissue
WHO	World Health Organization
WT	Wild-type
x-Gal	5-bromo-4-chloro-3-indolyl-beta-galaktopyranoside

Table of Contents

Acknowledgments 3

Abstract 4

Zusammenfassung 5

Abbreviations 6

Introduction 10

Site Directed Mutagenesis – Part I 21

- Background 21
- Experimental procedure 21
- Part I: Results and Discussion 24

COS-7 Immunomicroscopy – Part II 30

- Background 30
- Experimental procedure 30
- Part II: Results and Discussion 35

PKA/PKG Assay – Part III 61

- Background 61
- Experimental procedure 61
- Part III: Results and Discussion 65

Conclusions and Outlook 70

References 72

List of Tables 83

List of Figures 84

Appendix 87

- Tables 87
- Figures 91
- Sequencing Results 96

Introduction

The World Health Organization (WHO) defines overweight and obesity as an "abnormal or excessive fat accumulation that presents a risk to health" [1]. In 2016, more than 1.9 billion adults were considered overweight, with a body mass index (BMI) over 25 kg/m², and 650 million obese, with a BMI over 30 kg/m². For most individuals, an imbalance between the consumption of energy dense foods and decreasing levels of physical activity leads to unhealthy weight gain. However, obesity is additionally influenced by an individual's multigenic background as well as microbial factors, for instance the composition of gut microbiota [1, 2]. Over the last years, obesity has been linked to multiple diseases, such as type 2 diabetes mellitus (T2DM), cardiovascular disease, asthma, osteoarthritis and even certain types of cancers [3–5].

20-35% of the daily calorie intake in a normal human diet comprise of dietary fats and oils containing fatty acids (FA), which do not only serve as most efficient energy source in vertebrates but also represent essential building blocks of life. Their various roles in the cell include building constituents of biological membranes, changing target protein function trough posttranslational modification, and serving as precursors for various lipid mediators [6]. Due to their limited solubility and amphipathic structure, FAs have destructive effects on the cell in high concentrations, which is why they have to be stored in esterified form, as triacylglycerols (TAGs) (see Figure 1) [6–8]. TAGs are esters of glycerol and a varying blend of FAs. They are non-polar, and the vast majority of TAGs are deposited in lipid droplets (LDs) in white adipose tissue (WAT). This form of anhydrous storage makes fat a very efficient energy supplier, thus it can provide approximately six times the energy of an equal weight of hydrated energy sources, for instance glycogen [7–10]. The mobilization of the stored lipids is achieved via hydrolysis of TAG, a process called lipolysis, whereby non-esterified fatty acids (NEFAs) are cleaved off the glycerol backbone of TAGs, releasing the NEFAs into circulation to supply the body with FAs for the various purposes mentioned above [10].

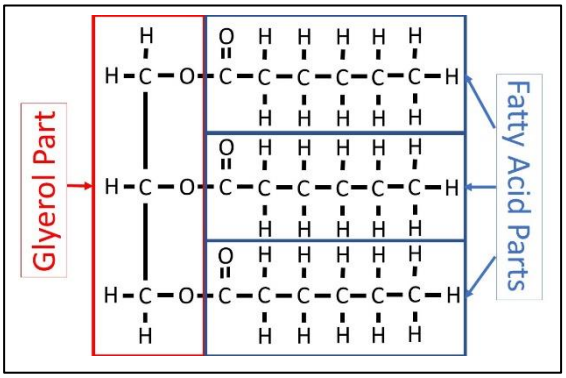

Figure 1: ***Molecular structure of triacylglycerols****. Triacylglycerol (TAG) molecules are built out of a glycerol backbone esterified with three fatty acids.*

In their 2018 paper, Demine et al. summed up the three mechanisms of lipolysis known to date: Macroautophagy and a form of microautophagy of LDs as well as the "classical" lipolysis [2]. Macroautophagy of LDs involves the formation of autophagosomal engulfment of the LD followed by the fusion with lysosomes, and furthermore the digestion of TAG contained in the LDs by lipolytic enzymes. LD degradation by microautophagy of LDs comprises the direct capture of small cytosolic portions by the lysosome in either a non-selective or selective manner, depending on the organelle it

occurs in [2]. The third mechanism - “classical” lipolysis - depicts the main focus of this thesis. It is a highly orchestrated process, in which multiple lipases and their regulators work together to hydrolyze TAG to three non-esterified fatty acids and glycerol in three consecutive steps [2, 11]. The first and rate-limiting step of lipolysis is the cleavage of the first fatty acid of TAG leading to diacylglycerol (DAG), which is catalyzed selectively by adipose triglyceride lipase (ATGL) [12, 13]. The hydrolysis of DAG to NEFA and monoacylglycerol (MAG) by hormone sensitive lipase (HSL) is the second step. In the final step, MAG is hydrolyzed to glycerol and NEFA by monoacylglycerol lipase (MGL) [13]. Multiple regulatory proteins, such as various perilipins, comparative gene identification 58 (CGI-58) and G0/G1 switch gene 2 (G0S2), have been shown to influence the process.

As lipid droplets (LDs) in adipocytes and the liver are respectively the main site for intracellular TAG storage and lipolysis takes place on the surface of said lipid droplets, their basic structure must be discussed [14]. LDs consist of a core of neutral lipids surrounded by a monolayer of phospholipids, storing primarily either cholesterol esters, used for membrane and steroid hormone synthesis, or TAG, which are serving as energy substrates, precursors of signaling lipids, or are used for membrane phospholipid synthesis [15]. On their surface, LDs are coated with LD-associated proteins, which are responsible for signaling, intracellular trafficking and lipid metabolism as well as providing a protective barrier for the accumulated lipids, shielding them from hydrolysis through various lipases [14, 16]. As many as 200 different protein components of LDs have been discovered in proteomic studies, whereas some of those are exclusively found on LDs but others do also localize to other subcellular compartments [15]. Many of these proteins play important roles in the regulation of lipolysis and will therefore be discussed in detail later.

Figure 2 gives a short and basic overview of the complex process of “classical” lipolysis and the involved proteins in adipocytes. Two states of lipolysis are shown: basal and stimulated. In adipocytes, in the basal state of lipolysis (fed state), CGI-58 is bound to perilipin 1 (Plin1) at the lipid droplet surface [17], sequestering CGI-58 from ATGL, hence preventing ATGL co-activation. Under basal conditions ATGL, HSL and probably MGL are primarily located in the cytosol but low levels of ATGL have shown to be associated with LDs, resulting in a low level of basal lipolysis [15], whereas ATGL is additionally bound to its inhibitor G0S2, leading to further decrease in hydrolase activity levels [18]. During periods of starvation (stimulated conditions), the binding of catecholamines by β-adrenergic receptors on the adipocyte cell surface initiates a Gαs-protein mediated signaling cascade that activates adenylyl cyclase, which in turn leads to rising levels of cAMP (3',5'-cyclic adenosine monophosphate) and subsequently to the activation of cAMP-dependent protein kinase (PKA). PKA then phosphorylates CGI-58, Plin1, ATGL, HSL and possibly G0S2, causing the following cascade of events initiating lipolysis: Phosphorylated CGI-58’s release by phosphorylated Plin1, the activation of phosphorylated ATGL by

phosphorylated CGI-58, the translocation of phosphorylated HSL to the LD, and its consecutive binding to phosphorylated Plin1 [15, 19, 20]. ATGL is also recruited to the LD in a Plin1-dependent manner, catalyzing the hydrolysis of TAG to DAG and FFA [15]. Subsequently, DAG is hydrolyzed by the Plin1-bound HSL to MAG and FFA, followed by the last cleavage of MAG into glycerol and the final FFA. [15]

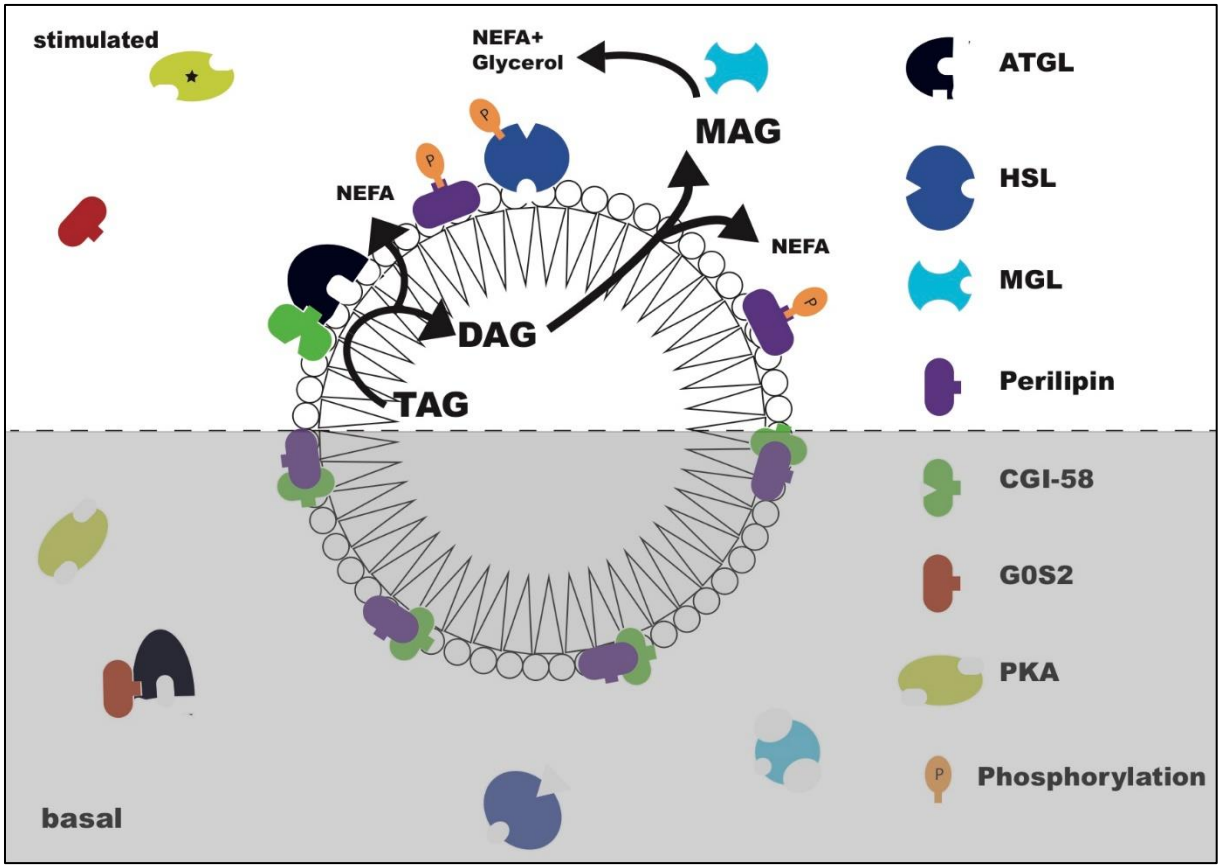

*Figure 2: **Overview of lipolysis in adipocytes**. The sequential degradation of triacylglycerols (TAG) to non-esterified fatty acids (NEFA) contains 3 steps. In the first and rate limiting step adipose triglyceride lipase (ATGL) hydrolyzes TAG to diacylglyerols (DAG) and NEFA. The hydrolysis of DAG to NEFA and monoacylglyerols (MAG) by hormone sensitive lipase (HSL) is the second step. In the final step MAG are hydrolyzed to glycerol and NEFA by monoacylglyerol lipase (MGL). Under basal conditions (grey field), the lipid droplet is coated with perilipin1 (Plin1) which is bound to comparative gene identification-58 (CGI-58), an activator of ATGL. G0/G1 switch gene 2 (G0S2) binds ATGL, and thereby decreases its lipase activity. Under basal conditions, HSL is located in the cytosol and has limited access to TAG stored within the lipid droplets or DAG produced during basal lipolysis. Under catecholamine stimulated conditions (white field), protein kinase A (PKA) is activated and phosphorylates most components of the lipolytic apparatus (CGI-58, Plin1, ATGL, HSL and possibly G0S2). After phosphorylation by PKA, CGI-58 dissociates from Plin1 to activate ATGL and Plin1 recruits HSL as well as ATGL to the LD and to its substrates, so lipolysis is stimulated. See text for details.*

Looking at the antagonist mechanism, the suppression of lipolysis, a key physiological factor comes into the picture: insulin. Additional to its major role concerning the control of cellular growth, proliferation and survival, insulin plays an integral part in the control of metabolic homeostasis [21]. Defects in any of those processes have shown to lead to diverse diseases, such as type 2 diabetes mellitus (T2DM), cardiovascular diseases and cancer [21]. Regarding its regulatory function in lipolysis, insulin postprandially triggers the accumulation and storage of TAG in adipose tissue by promoting the uptake of circulating glucose for de-novo lipid synthesis and FA esterification, besides suppressing lipolysis [22, 23]. The mechanism by which insulin controls lipolysis has not yet been fully elucidated

but it is assumed that its activation of phosphodiesterase 3b (PDE3B) plays an important role therein. Early works by Kitamura et al. showed that the insulin-induced phosphorylation of PDE3B by protein kinase B (Akt) activates the enzyme, leading to downregulation of intracellular cAMP concentrations. This consequently reduces PKA activity and decreases lipolysis to basal levels [23]. PDE3B's role as an important regulator of lipolysis has been generally accepted; however, the part of Akt in the process is heavily debated and it has been suggested that multiple intracellular signaling pathways, Akt-dependent and Akt-independent, have to be involved [23–26]. The fact that protein phosphorylation plays a major role in this and almost all insulin-mediated processes brings us to the next topic: the process of protein phosphorylation as a means of regulation of lipolysis.

Protein phosphorylation and phosphorylation-dependent intracellular signaling affects all basic cellular processes including lipolysis, metabolic maintenance, cell division, proliferation, differentiation, and signal transduction, just to mention a few [27, 28]. Each tissue requires tight regulation of its gene and protein expression according to its unique physiology, which is achieved by tissue-specific phosphorylation patterns of proteins [29]. Basically, phosphorylation is a transient, reversible process and the most common type of post translational modification (PTM), which can be found on various residues, such as serine (Ser/S), threonine (Thr/T), tyrosine (Tyr/Y), hydroxyproline or hydroxylysine [28]. The highly dynamic process is regulated by kinases and phosphatases [30], and this thesis mainly addresses the serine/threonine protein kinases cAMP-dependent protein kinase (PKA) and cGMP-dependent protein kinase (PKG). Kinases have varying mechanisms to assure the specificity of the phosphorylation and the control via local interactions near phosphorylation sites, using consensus sequences is one of them [31]. All proteins phosphorylated by PKA contain the consensus sequence Arg-Arg-X-Ser/Thr-Y (R-R-X-S/T-Y), whereas X represents a small and Y a large hydrophobic residue [7, 32, 33], although other motifs, such as R-X-S-X and K-R-X-X-S-X, have also been encountered [33]. Although both PKA- and PKG- regulated pathways mediate adipocyte lipolysis, PKG has been deemed responsible for exercise-induced lipid mobilization in particular. PKG is activated by elevated cGMP (3',5'-cyclic guanosine monophosphate)-levels, which are in turn caused by natriuretic peptides that are released mainly from the heart during exercise [34]. In 2003, Seneges et al. revealed that PKG activates the lipolytic cascade via phosphorylation of Plin1 and HSL, like PKA [35]. As a matter of fact, even its consensus sequence X-S-R-X, resembles the one of PKA [36]. As the phosphorylation of various proteins has been shown to have severe impact on lipolysis, the involved proteins, their structure, and their respective phosphorylation sites will now be discussed thoroughly.

ATGL – Adipose Triglyceride Lipase

ATGL, as the predominant TAG lipase in adipocytes, catalyzes the first and rate-limiting step in lipolysis, playing an essential role in basal and stimulated lipolysis. It was first discovered in 2004 by various research groups and is also known by the names patatin-like phospholipase domain containing-2

(PNPLA2), desnutrin or phospholipase A2ζ [6, 10, 37, 38]. ATGL is one of a family of nine PNPLA genes and represents the only robust TAG-hydrolase therein [6]. The lipase is expressed mainly in adipose tissue, but lower levels can be detected in virtually all other tissues including liver, testis, heart and skeletal muscle [10]. Orthologues of the enzyme can be found in essentially all eukaryotic species [11]. In terms of ATGL's significance in lipolysis, alterations in ATGL expression or activity should have a considerable impact on TAG storage in cells [39]. It would be reasonable to assume that ATGL knock out or knock down would lead to rising levels of accumulated TAGs, considering the absence of the prevalent TAG lipase. This was confirmed by studies showing that the loss of function of either ATGL or its co-activator CGI-58 causes forms of neutral lipid storage disease (NLSD). NLSD is characterized by abnormal accumulation of TAG in multiple organs and tissues [12, 40], the ectopic build-up of TAG leads to various defects on cellular, tissue and whole body level. Several studies conducted with ATGL-deficient mice showed that the absence of ATGL lead to an overall defect in energy homeostasis, as well as myopathy in cardiac muscle and defective thermogenesis in brown adipose tissue (BAT) [22]. Increased glucose tolerance and insulin sensitivity of these specimen were detected [22, 41], which may be explained by compensatory glucose utilization/insulin sensitivity following impaired lipolysis, TAG accumulation and reduced plasma-FA levels [13, 42] . Furthermore, ATGL's role in cancer was the topic of various studies: Das et al. showed that through reduced FA- mobilization and additional effects ATGL-deficient mice were protected from cancer-induced cachexia [43]. Zagani et al. found that the knockdown of ATGL in "non-small cell lung carcinoma" cell lines leads to decreased cell growth and motility as well as promoted apoptosis, making ATGL a potential target for chemotherapy [44]. This stands in contrast to Tomin et al., who found that ATGL knockout in A549 lung cancer cells increased motility by activation of SRC kinase [45]. Al-Zoughbi et al. proposed a possible role of ATGL as a tumor suppressor or immunohistological marker, because they linked ATGL expression levels with cancer cells as well as the malignancy of tumors [46].

ATGL's structural components have been investigated thoroughly in previous studies. Murine ATGL is a 486 amino acid long protein with a mass of approximately 54 kDa, whereas its human orthologue contains 504 amino acids with a sequence identity of 86% [10]. Although ATGL shares several common motifs with other known TAG lipases, it contains an unusual catalytic dyade (Ser47 and Asp166) [47–49], and its TAG-hydrolase activity was shown to be inhibited by permutation of the nucleophilic residue (Ser47) to alanine [12, 50]., ATGL harbors an α/β hydrolase fold and a G-X-S-X-G-site, containing the active Ser47 residue in its N-terminal patatin-homology domain [10], and the N-terminal region stretching from amino acid residues 1 to 254 harbors all catalytic activity as well as the capacity to interact with its regulators CGI-58 and G0S2 [51]. Experiments with truncated variations of ATGL revealed that its C-terminus is responsible for the proteins proper cellular localization, and it has been suggested that it may even contain an auto-regulatory element suppressing the enzyme's activity [51,

52]. In the basal state of lipolysis, ATGL is found in the cytosol as well as at the LD [17]; but after adrenergic stimulation the lipase (like HSL) localizes to the LD in a Plin1-phosphorylation dependent manner [18, 40, 53]. Kobayashi et al. deemed ATGL's C-terminus responsible for localization at the LD, after finding that, due to a mutation causing the loss of the C-terminus, patients develop NLSD-M (NLSD with myopathy), which led to the additional assumption that correct enzyme localization is a requirement for proper enzyme activity [54].

Studies of Eichmann et al. concerning ATGL's hydrolysis activity and its specificity regarding the preferred cleavage position of the long-chain fatty esters in the TAG revealed that ATGLs preference of TAG hydrolyzation at their sn2-position of the glycerol backbone, which interestingly changes to the sn1 position when co-activator CGI-58 is bound [55].

As previously mentioned, lipolysis activation includes the phosphorylation of ATGL and possible phosphorylation sites for human ATGL at residues Ser404, Ser428 and Thr372, and for murine ATGL (mATGL) Ser406 and Ser430 were identified [47, 56, 57]. Regarding their influence on lipolysis, it has been observed that phosphorylation of Ser404 results in TAG-hydrolase activity increase, and that Thr372 phosphorylation plays a critical role in ATGL's cellular localization as well as its lipolytic activity [47, 56, 57]. Although the roles of multiple phosphorylation sites have already been clarified, it has yet to be ascertained which kinases catalyze the reactions, since prior researches deemed either PKA or AMPK responsible [47, 58, 59]. These previous reports were partially contradictory, which is why differences regarding the responsible type of kinase as well as differences in cell and tissue type must be examined in greater detail.

To summarize, as a centerpiece of the lipolytic apparatus, ATGL's structure and its phosphorylation state as well as its lipase activity, localization and its interaction with regulatory proteins represent points of interest that must be investigated in great detail in future research of lipolysis [17, 50, 51, 60].

CGI-58 – Comparative Gene Identification 58

CGI-58 is an important co-activator of ATGL and also known as alpha-beta hydrolase domain-containing 5 (ABHD5) or 1-acylglycerol-3-phosphate O-acyltransferase [61]. It is a member of the alpha-beta hydrolase family, containing a "pseudo-catalytic triad" (Asn153/His327/Asp301), which lacks a nucleophile serine and therefore exhibits no hydrolytic activity [40, 61]. CGI-58 is expressed in practically all murine tissues, whereas adipose tissue and testis show high expression levels, and liver, muscle, kidney and heart show low expression levels [50, 62]. Researchers first identified CGI-58 in 2000, and after recognizing its connection to NLSD-I (NLSD with ichthyosis), it was also examined as a protein potentially taking part in lipid storage and lipolysis [40, 63, 64]. NLSD patients show excessive ectopic accumulation of lipids in multiple tissues; however, the disease's characteristics vary, depending on the presence of either ATGL- or CGI-58 mutations [40]. Patients with defective CGI-58

develop NLSD-I and frequently exhibit severe liver disease [65–67] and neurological defects, whereas patients with defective ATGL expression develop NLSD-M, rarely showing fatty liver disease or ichthyosis [40, 68]. The fact that ATGL and CGI-58 mutations lead to varying metabolic phenotypes suggests that CGI-58 also has ATGL-independent functions [40, 50, 68, 69]. CGI-58 influences lipolysis and consequentially lipid homeostasis in various tissues, such as skin, skeletal muscle and heart muscle, liver, and of course adipose tissue [70]. CGI-58's role as a co-activator during ATGL-mediated catecholamine-stimulated lipolysis in adipocytes was first revealed by Lass and colleagues in 2006 [50] and then confirmed by multiple independent research groups [17, 60, 70, 71]. After showing that adipose-selective overexpression of CGI-58 did neither increase basal nor stimulated lipolysis in adipocytes, Lord et al. proved that CGI-58 expression is required for maximal stimulation of ATGL-mediated lipolysis in WAT [68]. CGI-58's involvement in lipolysis in adipocytes is definitely one of its best characterized, but recently even more functions of CGI-58 have been elucidated: The realization that the NLSD-I's metabolic phenotype and CGI-58 mutations are associated and the finding that global CGI-58 knockout mice died after several days due to a skin barrier defect [69] lead to further studies concerning CGI-58's role in skin cells. Kien et al. did research about this linking CGI-58 to the stimulation of PNPLA1-mediated ω-O-acylceramide biosynthesis, which in turn is essential for the formation of a functional skin permeability barrier [72]. Regarding its function in liver cells, Lord and colleagues found that CGI-58 regulates hepatic TAG storage and inflammation in an ATGL-independent manner [68]. Additionally, up until now CGI-58 has been shown to influence metabolism, tumor progression, skin barrier formation, and even viral replication [73–76].

CGI-58's essential role in ATGL-activation has been thoroughly examined, and though the mechanism itself has not yet been identified, a basic understanding of the interaction has been gained, and structural determinants of CGI-58 involved have been analyzed. Sanders et al. confirmed that the C-terminal region (amino acids 277-351) in murine CGI-58 is critical for ATGL activation, and the therein contained highly conserved residues Arg299, Gly328 and Asp344 play essential roles [76]. Predicted 3D-models show that the three residues are located closely to each other on the CGI-58 binding surface, and a mechanism was suggested in which Gly328 may interact with the membrane-phospholipids of LDs to allow favorable interactions of Arg299 and Asp344. Additionally, mutagenesis analysis indicates that the negative residue Asp344 is crucial for ATGL activation [76]. Another residue - Tyr330 (Y330) - has been shown to pose as a docking site for endogenous and/or synthetic binding partners [70]. The N-terminal region of CGI-58 contains a Trp-rich hydrophobic stretch, which is essential for the localization of CGI-58 to LDs. The first 30 N-terminal residues have found to be crucial for ATGL activation [77], whereby the removal of amino acids 10-31 resulted in failing CGI-58 localization at the LD along with its ATGL-activation [77]. In 2015, this sequence was shown to serve as a LD-anchor for CGI-58 [78].

As previously mentioned, PKA-meditated posttranslational modification of CGI-58 is also involved in ATGL activation. Ser239 is contained in the PKA-consensus sequence (Arg^{236}-Lys-Tyr-Ser-Ser or R^{236}-K-Y-S-S) [32, 33] and was identified as a critical phosphorylation site influencing the process of releasing sequestered CGI-58 from Plin1 [79]. Mutation analysis by Sahu et al. showed that mutation of Ser239 to alanine inhibited the dispersion of CGI-58 from the perilipin scaffold, therefore inhibiting CGI-58's interaction with and co-activation of ATGL [17, 79]. In this thesis, it was attempted to examine the influence of fatty acid binding by Tyr330 of CGI-58 in this process. For this purpose, co-localization studies of CGI-58 Tyr330 and Ser239-Tyr330 double mutants, and analysis of their properties regarding basal and stimulated lipolysis were performed.

G0S2 - G0/G1 switch protein 2

ATGL is not only regulated by CGI-58. In 2010, Yang et al identified G0/G1 switch protein 2 - also known as G0S2 - as a specific inhibitor for ATGL. Its name originates from its first identification in cultured mononuclear cells during the drug-induced cell cycle transition from G0 into G1 phase by Russel and Forsdyke in 1991 [18, 80, 81]. Several studies show the involvement of G0S2 in various cellular processes, such as cell proliferation, apoptosis, oxidative phosphorylation, or even carcinogenesis [82–85]; however, it has been suggested that G0S2's main function lies in its role as molecular brake on TAG catabolism [86]. The impacts of G0S2 on lipolysis and whole body metabolism were investigated using G0S2 knockout mice, leading to the following revelations: G0S2-knockout mice are lean, resistant to weight gain induced by high fat diet, and their glucose tolerance and insulin sensitivity are increased [87–89]. Their energy metabolism shifts to enhanced lipid metabolism and elevated thermogenesis [44]. As previously stated, the main purpose of WAT is the storage and, if needed, the release of energy, whereas in brown adipocytes, the respiratory chain is uncoupled from ATP-synthesis in mitochondria by tissue specific expression of mitochondrial uncoupling protein (UCP1), resulting in the dissipation of the chemical energy as heat, also known as adaptive thermogenesis [2, 90, 91]. The white adipose tissue of the G0S2 knockout mice showed higher levels of lipase activity and enhanced stimulation of lipolysis as well as elevated expression levels of genes linked to thermoregulation and oxidation, which indicates browning [88], whereby the term browning refers to the development of beige adipocytes in WAT in response to various activators [91]. It has been suggested that browning of WAT in these subjects consequently leads to the reported higher cold tolerance [88].

G0S2 is highly expressed in murine WAT, BAT and liver as well as in moderate levels in heart tissue, skeletal muscle and the lung [18, 89], and both in human and mouse, the G0S2 gene translates to a 103 amino acid long small basic protein [92]. Studies revealed that G0S2 binds ATGL directly, and that their bond is formed between the hydrophobic domain of G0S2 and the patatin-like domain of ATGL [18]. G0S2 colocalizes with ATGL, suppressing its hydrolase activity in the basal state, and even accompanies the lipase to the LD after lipolysis stimulation, but the exact regulatory mechanism has

not yet been cleared up [93]. Nevertheless, studies suggest that there is an interdependent relationship between G0S2's and ATGL's localization at the LD since C-terminally truncated versions of ATGL, incapable of localizing at the LD by itself, were anchored to the LD after co-expression with G0S2 [93]. Further experiments with C- and N-terminally truncated versions of G0S2 showed that a hydrophobic stretch from Lys20 to Ala52 is essential for ATGL inhibition, and that ATGL regulation via CGI-58 and G0S2 takes place independently following a non-competitive mechanism [18, 39, 51, 60]. Testing G0S2's interaction with other lipases, including HSL and MGL, revealed that G0S2-mediated inhibition is specific to ATGL [39]. Seeing that the binding of CGI-58 alone is not enough to activate ATGL when bound to G0S2, keeping the non-competitive mechanism of inhibition in mind, it can be assumed that additional regulatory events, such as post-translational modification of G0S2, may affect the whole activation-inhibition-interplay [93].

Perilipins

Finally, LD-coating scaffold proteins called perilipins play a very important role in the control of TAG turnover. In mammals, lipid droplets have been shown to always contain perilipins (Plins) [15] but their expression varies from cell type to cell type. Different forms of perilipins (Plin1-5), and even splicing variations, are expressed [94]. The Plins are collectively referred to as the family of PAT proteins, which received its designation by the original names of their founding members Plin1, 2 and 3: **p**erilipin, **A**DRP (adipose differentiation-related protein or adipophilin) and **T**IP47 (tail-interacting protein of 47 kDa) [95, 96]. Differences in expression patterns as well as distinctions concerning the Plins stability can be obtained: Plin1, 4 and 5 are expressed in a limited number of tissues, whereas Plin2 and 3 are expressed ubiquitously. Additionally, studies showed that Plin1 and 2 exist exclusively in association with LDs, whereby Plin3-5 have been shown to remain stable in the absence of LD binding as well bound to other cellular components [15, 94]. My studies focused on Plin1 and Plin5, being the predominant perilipins present in cell models regarding our research topic.

Plin1 is abundantly expressed only in adipocytes in WAT and BAT and at lower levels in steroidogenic cells of the adrenal cortex, the testis and ovaries, in other words β-adrenergic stimulable cells [97, 98]. Plin1 was shown to act as a gatekeeper, restricting adipose lipolysis under basal (fed), and even somehow under stimulated conditions. Under basal conditions, regulation is achieved through the following mechanisms: Firstly, Plin1 restricts the access to the lipids stored in LDs by building a barrier shielding the TAG from cytosolic lipases, like ATGL and HSL [97, 99, 100]. The second mechanism is the sequestration of CGI-58 by Plin1 to prevent its interaction with ATGL, thereby reducing basal lipolysis levels [17, 62, 101, 102]. The last regulation method connects to the impact of elevated insulin levels during the basal state on lipolysis. The previously discussed insulin-mediated control of lipolysis (see

above for details) leads to lower levels of phosphorylation of Plin1 and the aforementioned lipases, causing lower levels of TAG hydrolysis [22–24].

As stated previously, stimulation of lipolysis leads to phosphorylation of Plin, and early studies revealed that Plin1 is one of the most highly phosphorylated proteins in association with LDs [103]. Murine Plin1 is a 517 amino acid long protein that contains 6 predicted PKA consensus sequences (R-(R/K)-X-S) for serine phosphorylation, although recent phosphoproteomic analysis revealed that no less than 27 possible phosphorylation sites (Ser/Thr-residues) for PKA and other kinases are present [15, 21, 29, 104]. The six originally predicted sites (Ser81, Ser222, Ser276, Ser433, Ser492, and Ser517) have already been thoroughly investigated by various groups [29, 105, 106]. Mutagenesis analysis of the three N-terminal phospho-sites showed that PKA-mediated phosphorylation of Ser81, Ser222, and Ser276 is critical for recruitment of HSL to perilipin-coated LDs [105, 106], and consequently maximizing levels of lipolysis. Therefore, Plin1 can be considered as a regulator of stimulated lipolysis, in the sense that only the phosphorylation of HSL and Plin1 causes the recruitment of HSL from the cytosol to the LD, so that HSL binds Plin1, thus gaining access to the stored lipids [100, 105]. The C-terminal phosphorylation sites Ser492 and Ser514 turned out to be responsible for the interaction with CGI-58, whereas phosphorylation of either of both sites leads to the rapid release of the ATGL activator [17]. Additionally, research showed that the C-terminal sequence from amino acids 382 to 429 is necessary for correct binding of CGI-58 [62]. To sum up, Plin1 coordinates lipolysis through the regulation of lipase access to the LD, ATGL access to CGI-58, and the provision of a docking site at the LD for HSL.

The second perilipin we examined more thoroughly in the context of lipolysis regulation was Plin5. Plin5 was discovered by several groups and originally given various names, such as lipid storage droplet protein 5 (LSDAP), PAT-1, and OXPAT (a combination of PAT and the origin of its expression in oxidative tissue) [107, 108]. Murine Plin5 is a 463 amino acid long LD-associated protein that coordinates lipolysis in oxidative tissue, such as BAT, cardiac and skeletal muscle, and to a lesser extent in liver [15, 108–110]. Its N-terminus contains an HSL binding site that is also conserved in Plin1-3, and its C-terminus includes overlapping binding sites for ATGL and CGI-58 [105, 111–113]. Plin5 recruits HSL, ATGL and CGI-58 to the LD under basal conditions but restricts TAG turnover through the following mechanisms: One factor is the mutually exclusive binding of Plin5 to either ATGL or CGI-58 [113]. As only the binding of one of the proteins to Plin5 is possible, Plin5's interaction with ATGL and consecutively the activation of lipolysis is inhibited up until the stimulation of lipolysis, induced by the release of CGI-58 [15]. The other factor is the influence of phosphorylation on the activation of lipolysis, which was revealed after showing that the binding of HSL to the LD protein scaffold alone is insufficient to promote lipolysis [105]. Studying the PKA-mediated phosphorylation and lipolysis stimulation regarding Plin5 phosphorylation sites, Ser155 has been identified as a target, since it is contained in a

PKA consensus sequence, and mutation to alanine leads to a decrease of PKA-mediated lipolysis stimulation [111, 114]. Additionally, evidence for in vivo phosphorylation of Plin5 at residues Ser155, Ser161 and Ser163 has been found in phosphoproteomics studies [115–117]. Plin5 knockout and overexpression experiments showed that Plin5 plays an important role in energy homeostasis, especially in heart tissue [118–122]. Plin5 null mice showed impaired TAG storage capacity in heart tissue and elevated levels of FA oxidation in cardiomyocytes. Both can be explained by increased TAG turnover due to absent protection of the LD-contained TAG through Plin5 [118–120]. Additionally, a change of TAG storage in muscle and liver of Plin5 null mice was detected. Intriguingly, the TAG content of oxidative muscle tissue (red quadriceps) was decreased but glycolytic muscle tissue - such as the white quadriceps - were not influenced compared to wild-type mice [120]. In liver, the TAG content in cells was decreased, especially after the mice received a high fat diet [123]. Various studies showed that the opposite can be examined in Plin5 overexpression experiments. Overexpression of Plin5 lead to elevated TAG storage levels in LD in murine cardiomyocytes, increased TAG storage in intramyocellular LDs in skeletal muscle, and interestingly results in a gene expression pattern that favors FA oxidation metabolism in intact cultured cells [107, 121, 122, 124]. These findings are supported by previous studies showing that Plin5 overexpression causes increased TAG content due to diminished TAG turnover [107, 109, 111, 114].

The proteins described in the previous paragraphs play a major part in the lipolytic apparatus and changes in expression levels or in their sequence, even though point mutations can have huge impacts on lipolysis. Considering the critical role of PKA-mediated phosphorylation and lipolysis stimulation, the phosphorylation sites of every protein and their respective influence on lipolysis represent very important topics of research. In this thesis, the main focus lies on the phosphorylation sites of CGI-58 and their impact on cellular localization and lipolysis activation under basal and stimulated conditions. Part I of the thesis discusses the generation of mutations via site-directed mutagenesis, including mutations of CGI-58 at residues Ser239 (S239), and Tyr330 (Y330). Mutation variants of ATGL, G0S2, Plin1 and Plin5 were prepared for future experiments. Part II discusses fluorescence- and immunofluorescence microscopy experiments, analyzing the co-localization of CGI-58 in wild-type or mutated form with Plin1 wild-type in COS-7 cells. Finally, part III of this thesis addresses the phosphorylation site "R^{236}KYSS" in CGI-58 and the possibility of it being a target sequence for PKG as well as PKA.

Site Directed Mutagenesis – Part I

Background

Plasmids containing wild-type or mutated versions of ATGL, CGI-58, G0S2, Plin1 and Plin5 were needed for expression in further experiments. This chapter will discuss the preparation of plasmids, mutations of genes via site directed mutagenesis, design of primers, experimental procedures and the resulting plasmid sequences as well as the sequencing results.

Experimental procedure

If not mentioned otherwise, chemicals were purchased from Sigma-Aldrich.

Plasmid templates

Murine G0S2- and human G0S2 plasmids were kindly provided by Martina Schweiger (research group of R. Zechner at Karl-Franzens University Graz) [93]. Murine CGI-58- and ATGL plasmids were kindly provided by Juliane Bogner-Strauss (University of Technology Graz) [50]. The plasmid containing human CGI-58 wild-type with an additional Yn-B-tag was kindly provided by David Savage (Cambridge University) [125]. Murine Plin5 wild-type- and Plin5 S155A plasmids were kindly provided by Stephanie Kolleritsch (research group of G. Hämmerle at Karl-Franzens University Graz) [114]. Various plasmids containing fluorescencently tagged versions of murine CGI-58 (mCGI-58), mPlin1, mPlin5 and mATGL, as well as a previously mutated version of mPlin1 were kindly provided by James G. Granneman (Wayne State University School of Medicine, Detroit) [17, 102, 113]. Plasmid maps separately provided by J. Granneman can be found in the appendix (see Figure 28 and Figure 29). Lisa Wechselberger (research group of M. Oberer at Karl-Franzens University Graz) kindly provided us with mCGI-58 DNA cloned into a pET-28b+ vector. The recombinant version of CGI-58 contained an smt3-tag, a 6xHis-tag and a tobacco etch virus (TEV) cleavage site. The sequence provided by the group of M. Oberer can be found in the appendix in Figure 30. All provided plasmids were sequenced before conducting the site-directed mutagenesis (SDM) or any further experiments. Table 6 in the appendix shows a summary of all plasmid templates with contained mutations, the original vectors, the cloning sites and their respective literature reference.

Primer design

SDM primers and sequencing primers were designed according to primer design guidelines defined in the QuikChange protocol [126]. Table 7 and Table 8 in the appendix show all designed primers with their 5'-3'-sequence and additional information to their design and use.

Site-Directed Mutagenesis (SDM)

The basic workflow of the SDM-reaction describes a three-step process: In the initial step - a thermal cycling reaction - the mutant strands are synthesized using the previously designed SDM primers and template plasmids to produce the desired mutations. Secondly, the template plasmids are degraded by DpnI-digestion and in the third and final step, the mutated molecules are transformed into competent cells for nick repair and subsequent plasmid production. The "QuikChange II XL Site-Directed Mutagenesis"- reaction kit (Agilent Technologies, Cat. No. 200521) was used to introduce the mutations. The kit provided all materials for the SDM reaction. Resulting plasmids were transformed into either ultracompetent XL10-Gold-cells (provided with Agilent-kit) or SIG-10 cells (Sigma-Aldrich, Cat. No. CMC0001). Experiments were conducted following the protocol provided by Agilent Technologies [126], therefore only changes to this protocol are noted as follows.

Changes to the QuikChange II XL Site-Directed Mutagenesis protocol

Mutant strand synthesis reaction (thermal cycling)

50 ng of DNA template and 125 ng of each primer were used for each SDM reaction. The composition of the reaction mixes can be found in the provided protocol [126]. The polymerase chain reaction (PCR) program used for the majority of the experiments can be found in Table 1. Because of different primer properties and consequently distinct annealing temperatures, the protocols for a handful of PCR reactions had to be varied: Reactions with all G0S2 primers designed by Anita Sahu (see Table 7) were conducted with an initializing temperature of 98°C and an elongation period of 8 minutes. For reactions with mABHD5 and hABHD5 primers designed by Anita Sahu (see Table 7), the initializing temperature was altered to 98 °C, the annealing temperature to 68 °C and the elongation period was changed to 8 minutes.

Table 1: ***PCR Program used for SDM reactions*** *(alterations for special reactions listed in previous paragraph)*

	Step	**Temperature [°C]**	**Duration [min]**
Start	**Initialization**	95	01:00
16 Cycles	Denaturation	95	00:50
	Annealing	60	00:50
	Elongation	68	06:00
End	Final Elongation	68	07:00
	Final Hold	4	∞

PCR product check with agarose gels

After DpnI digest, the PCR products were examined via agarose gel electrophoresis. 5 µL of the PCR products and 4 µl of the DNA templates (~200 ng) were loaded on a 1% agarose gel in 1X TRIS-Acetate-

EDTA-buffer containing 0.1% GelRed™ (VWR, Cat. No. 730-2957). The gel was run for 1h at 80V and bands were visualized under UV light using the Biorad ChemiDoc XRS+ imaging system with Image Lab Software.

Transformation into XL10-Gold/SIG-10 cells

The transformation into either XL10-Gold cells or SIG-10 cells was performed according to the respective manual [126, 127]. 7 µL of DpnI treated DNA were used for the transformation instead of the proposed amount of 2 µL. Either NZCYM broth, SOC broth (for recipe see Table 9 in the appendix) or company provided recovery medium was used as transformation medium.

Cultivation of E. coli cells on LB-agar

Luria Bertani (LB) agar plates (prepared under sterile conditions according to the manual provided by Sigma Aldrich [128]) were used for cultivation of the transformed cells over night at 37°C.

Glycerol stocks and Miniprep DNA purification

Single colonies of each plate were picked and grown in 10 mL LB-broth containing the appropriate antibiotic for each plasmid. 300 µL of the overnight culture were mixed with 700 µL of sterile 80% glycerol and frozen at -80°C to maintain stocks. The rest of the cells were harvested and the resulting pellet was used for plasmid DNA preparation using the Wizard® Plus SV Minipreps DNA Purification System (Promega, Cat. No. A1330) [129]. The purification was conducted following the protocol provided by Promega, only the elution volume was changed to 60 µl of nuclease-free water. After purification, the concentration of the DNA samples was determined using the Thermo Fisher Scientific NanoDrop 2000 spectrophotometer [130].

Determination of concentration of plasmid DNA

Plasmid DNA concentration was measured using the "Nucleic Acid" application of the Thermo Fisher Scientific NanoDrop 2000 spectrophotometer in pedestal mode, following the provided protocol by Thermo Fisher Scientific [130]. 1 µL of nuclease-free water was used as blank. 1 µL of each prepared DNA sample was measured to determine its DNA content. The measurement of the concentration is based on the sample's absorbance at 260 nm normalized to a 10 mm path length. A ratio of absorbance at 260 nm to absorbance at 280 nm was additionally used to assess the purity of the DNA sample, whereby a ratio of ~1.8 is generally accepted as pure for DNA. The presence of protein, phenol or similar contaminants which absorb strongly near 280 nm would lead to a lower ratio.

Sequencing of plasmid DNA samples

All used constructs were prepared and sent to be sequenced by LGC sequencing services according to their guidelines [131].

Part I: Results and Discussion

The design, the production, and the isolation of plasmids coding for proteins needed in further experiments, as well as the control of plasmid quality and the accuracy of all sequences lay the ground work for further experiments. As SDM reactions involve various steps, a discussion of the primer designing process, the SDM workflow, as well as the consequently obtained results is presented in the following paragraphs.

Primer design displayed the initial step of the experiments. All SDM primers were designed manually following guidelines protocolled in the kit manual [126] and ordered as custom primers from Sigma Aldrich. The person responsible for primer design is protocolled in Table 7. The first step in primer design was to search the DNA sequence of each construct for the codon corresponding to the amino acid about to be exchanged. So, if an exchange from serine to alanine is required, and the original sequence contains the codon "TCT" for serine, a short primer sequence containing the exchanged codon "GCT" for alanine in place of the original "TCT" is generated. As proper binding of the SDM-primers is often an issue during the PCR, codons that vary as little as possible from the original sequence have to be chosen. The main obstacle to the designing process is the choice of a sufficiently long sequence with no palindromic patterns that ideally places the exchanged base/s in the middle of the primer. Additionally, the ideal melting temperature of a primer is 78°C, whereas variation of the G/C content of the primer provides a possibility to change this feature [126].

Starting the SDM reactions, it became clear that the multiple-step workflow could possibly contain a number of sources of error. To facilitate troubleshooting in case of failure of the reaction, multiple control points were implemented into the SDM workflow.

Quality of the chemical components of the kit was controlled via a control reaction, using the pWhitescript™ 4.5-kb control plasmid and control primers. Problems concerning the chemicals or the enzymes delivered with the kit could be excluded as possible sources of error, if the control reaction produced a plasmid product.

The check of PCR-products via agarose gel electrophoresis depicted another control point in the workflow. After thermal cycling was completed, a treatment of the reaction mix with DpnI was conducted. DpnI only digests hemi-methylated or methylated DNA [126], which means that the used template DNA is digested whereas the newly generated PCR product will stay intact. To check plasmid template size and quality, both the purified template plasmids and their respective product after SDM reaction were analyzed via agarose gel. To give an example of these analyses, an agarose gel (see Figure 3) loaded with three SDM reaction products and their templates was selected to discuss all possible outcomes. Lanes 2-4 show the template plasmids and lanes 5-8 the respective SDM reaction products.

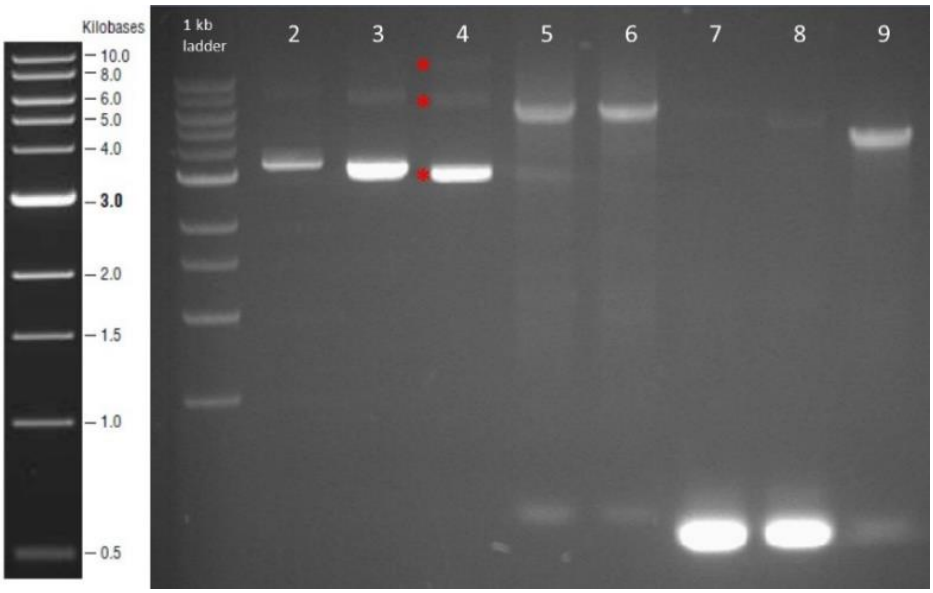

*Figure 3**: 1% Agarose gel run of various SDM reaction plasmid templates and their consecutive SDM-PCR reaction products to control successful amplification** and 1kb DNA ladder with according DNA masses (kb) [132]. 200 ng template plasmids were loaded in lanes 2-4. 5 µL of PCR reaction products were loaded in lanes 5-8. Gel was run for 1 hour at 90 V. Lane 1: 3 µL Quickload 1 kb DNA ladder (NE Biolabs; Cat. No. N0468S); Lane 2: ~6-kb EYFP- N1 plasmid containing the Plin1 A508T Q512L –EYFP gene; Lane 3: 6.1-kb EYFP-N1-vector containing the FL-Plin5-EYFP gene; Lane 4: 5.7-kb EYFP-N1-vector containing the gene for mCGI-58-mCherry; red stars mark open circle, linear and supercoiled versions of the plasmid (from highest to lowest signal); Lane 5: ~6-kb EYFP- N1 vector containing Plin1 A508T- EYFP after SDM-PCR reaction; Lane 6: 6.1-kb EYFP-N1-vector containing the FL-Plin5 S155A-EYFP gene after SDM-PCR reaction; Lane 7 and 8: 5.7-kb Dpn1-digested EYFP-N1-vector containing mCGI-58-mCherry; Lane 9: pWhitescript™ 4.5-kb control plasmid provided with QuikChange Mutagenesis Kit*

The following reactions are presented: reversion of the Q512L mutation in Plin1 A508T Q512L-EYFP cloned into the ~6-kb EYFP-N1 plasmid (lanes 2/5), introduction of S155A-mutation into FL-Plin5-EYFP cloned into a ~6.1-kb EYFP-N1 vector (lanes 3/6) and the introduction of S239A- and S239D-mutations in mCGI-58-mCherry cloned into a ~5.7-kb EYFP-N1 vector (lanes 4/7/8).

Lanes 2-4 contain the plasmid templates and show 3 distinct bands, best visible and marked by red stars in lane 4, one strong (~4 kb) and two faint bands (~8 kb and ~10 kb). The presence of three signals can be explained by the different plasmid conformations. The strongest band at approximately 4 kb represents the supercoiled version, the band at ca. 8 kb the linear conformation, and the top band at 10 kb the nicked conformation of the plasmid [133]. The present signal pattern (lacking signals of small DNA fragments) indicates that the templates were intact and had not degraded or been digested by nucleases. The combination of these results und the fact that the correct sequence was confirmed via sequencing led to the assumption that no problems arose due to template properties and quality.

Lane 5 contained the SDM reaction product Plin1 A508T-EYFP in an EYFP-N1 vector after successful reversion of a previously contained Q512L mutation. The signal observed at ~6 kb fits the aforementioned plasmid size. Additional signals in the lower regions of the gel suggest that broken down DNA template is present, accounting for a working DpnI digest of the template plasmid.

Lane 6 was loaded with the SDM reaction product of the plasmid cloned with FL-Plin5-EYFP after successful introduction of the S155A mutation. A signal pattern comparable to the one in lane 5 indicates a completed SDM reaction with DpnI digest.

The products of the SDM reactions to introduce the mutations S239A (lane 7) and S239D (lane 8) into mCGI-58-mCherry were loaded in lanes 7 and 8. Both lanes only show signals in the lower part of the gels (at approximately 0.5 kDa), pointing to the presence of solely small DNA fragments. This led to the conclusion that only the DpnI digested template DNA and no new PCR product was generated. In search of probable causes of the failed reaction, different factors were excluded due to the control steps. Since the control reaction (lane 9) and the other two SDM reactions had worked properly, the quality of the kit was not responsible. The SDM-primers had already been successfully used for the introduction of the mutation into other CGI-58 constructs with the protocol provided by Anita Sahu (see Table 7); however, they did not work with the newly prepared CGI-58-mCherry construct contained in the EYFP-N1 vector, so primers were examined as a possible error source next. The primer sequence was compared to the sequences of the mCherry-tag and the known EYFP-N1 vector structures (S40V promoter, KanR/NeoR, ColE1 origin), to exclude sequence overlaps. Since there were none found, it was deduced that primer quality could have deteriorated over time, therefore a new set of primers with a slightly shorter sequence was ordered (see Table 7). As properties of SDM primers influence the PCR reaction, the previously used PCR program had to be adjusted, as the respective primer melting- and annealing temperatures required different PCR settings (see Table 1 and chapter experimental procedure for detailed programs). The new primer set in combination with the adjustment of the annealing temperature in the PCR program led to a positive result of the SDM reaction. Only SDM reactions with the CGI-58-mCherry constructs required troubleshooting.

All other mutations worked from the start, leading to the conclusion that all following steps, i.e. the transformation of the plasmids into *E. coli* cells via heat shock, the overexpression and consecutive plasmid preparation and purification worked flawlessly.

The sequencing of all plasmids at LGC sequencing services represented the final check of the SDM reactions.

Sequencing results – Results and Discussion

Sequencing results obtained by LGC sequencing were analyzed using the Web Basic Local Alignment Search Tool on the website of the National Center for Biotechnology Information (NCBI) [134]. Wild-type gene sequences were obtained from the NCBI database and can be found in in the appendix. Sequencing results for all prepared plasmids can be found in the appendix and are presented as follows: Figure 4 shows the DNA sequence of the sequencing result and if the sequencing was covered by the forwards (green background), reverse (red background) or by both (yellow background) primer results. The used primer sequences for all constructs can be found in Table 8. Figure 6 shows the amino acid sequence of the results and the respective coverage by the primers. Sequences were translated using the ExPASy translate tool [135]. Figure 5 and Figure 7 show the legends defining various markings and colors found in the results. Mutated bases/amino acids are marked with red letters, whereby undesired *silent* mutations have white background, but undesired *coding* mutations are additionally marked by a turquoise background. If bases or amino acids were intentionally exchanged by mutations these bases/amino acids were marked with white letters and a dark blue background. Unsequenced areas were marked via magenta background.

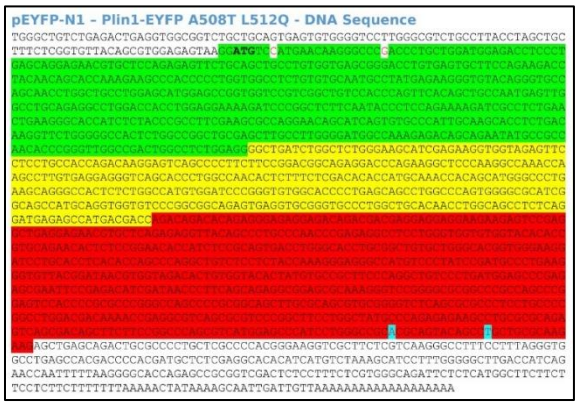

*Figure 4: **DNA sequence of sequencing result of Plin1 A508T L512Q in vector pEYFP-N1**. Green: Sequencing result of forward primer; Red: Sequencing result with reverse primer; Yellow: Overlapping region of both sequencing results*

*Figure 6: **Amino acid sequence of sequencing result of Plin1 A508T L512Q in vector pEYFP-N1.** Green: Squencing result with forward primer; Red: Sequencing result with reverse primer; Yellow: Overlapping region of both sequencing results*

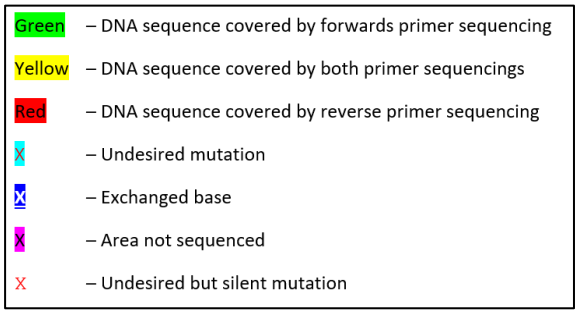

*Figure 5: **Legend explaining features in DNA sequencing results** (see Figure 6)*

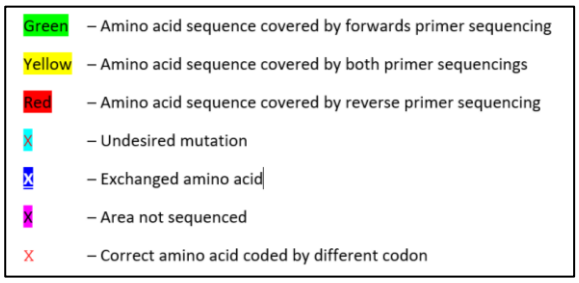

*Figure 7: **Legend explaining features in translated amino acid sequence of sequencing result** (see Figure 5).*

All received plasmids were sequenced to assure their correct sequence (see Table 6 for all information concerning the received plasmids) prior to any experiments. Some sequencing primers were re-ordered as custom primers and, as their sequences were obtained online, the respective online source can be found in Table 8. Most of the received constructs contained no mutations but the exceptions are discussed, as follows.

The Plin1-EYFP construct (sequencing results presented in Figure 4) was delivered under the designation wild-type, but sequencing showed that it contained multiple mutations, and hereafter it was labeled correctly as Plin1-EYFP A508T L512Q. 2 mutated bases (see second line in Figure 4) were found In the DNA sequence, after blasting the result against the NCBI database (red letters/white background). Analysis of the codons showed that the translation of the sequencing result 'ATG-TCC-ATG-AAC-AAG-GGC-CCG' led to the same amino acid translation as the wild-type sequence 'ATG-TCA-ATG-AAC-AAG-GGC-CCA' because the codons TCC and TCA both code for serine and CCG and CCA both code for proline. Granneman et al. noted that all the constructs were generated using cDNA of plasmids or tissues but the exact sequence was not obtained [102]. Despite the fact that these mutations were undesired, they are silent, which is why they were marked in the results, but no repair of the sequence was needed. In the last line, additional mutations were detected (marked by turquoise background in Figure 4). The wild-type sequence 'GCG-CAG-TAC-AGC-CAG' would translate to the amino acid sequence 'AQYSQ'; however, the translation of the sequencing result 'ACG-CAG-TAC-AGC-CTG' resulted in the amino acid sequence 'TQYSL'. These missense mutations were the only undesired coding mutations found in the first sequencings of all received template plasmids. The repair of these mutations had to be the initial step of the experiments, in order to get a correct version of the Plin1 wild-type gene. As the 2 mutations were occurred quite close to each other, changing both in one step came to mind, but this possibility was abandoned, since the primer design would contain too many exchanged bases to assure proper binding during thermal cycling. In consequence, two consecutive SDM reactions were conducted, reversing one mutation after the other. Sequencing results of each step are shown in the appendix (Figure 60, Figure 61 and Figure 62).

Analysis of the received ECFP-C plasmid containing the ECFP-ATGL construct turned out problematic. Based on information concerning plasmid properties provided by Dr. Granneman, the sequencing primers (an EGFP-C forward primer and an EBV reverse primer) were chosen according to the ECFP-C1 vector map obtained by Addgene [136]. This choice led to incomplete sequencing due to issues with the reverse primer. As the ECFP-ATGL gene was cloned into the HindIII site of the vector, it was considered choosing a reverse primer binding to a near sequence. There are mainly restriction sites present in this area of the plasmid, consisting of palindrome sequences. This is why this region was ruled out as a primer sequence, because, as mentioned above, primers containing palindromic sequences tend to build secondary structures, leading to the inhibition of the binding of the template

DNA and furthermore the PCR. It was decided to design a second forward primer, attaching to the center of the already correctly sequenced part of the ATGL-sequence (hence the name of the primer "ATGL fwd middle seq"; see Table 8). After this, a complete and accurate sequencing of the gene was possible. The received version of ECFP-ATGL contained an R30H mutation, which was confirmed by a second sequencing run. However, this mutation exists in functioning versions of the protein, so it was ignored and the construct was used for transfection [37, 137].

The mCherry- tagged mCGI-58 construct, provided by J. Granneman, was cloned into an EYFP-N1 vector. Sequencing with the forward CMV-primer worked, however, the frequently used EGFP-N reverse primer did not lead to any result. As it was known that mCGI-58 was cloned into the plasmid with an N-terminal mCherry-tag, it was decided to design the primer complementary to the mCherry-sequence, leading to successful und complete sequencing of the construct. The mCherry sequence was obtained using the NCBI database (GenBank Accession number: KJ541672) and the sequencing result can be seen in Figure 53.

We were additionally provided with a previously mutated EYFP-tagged version of Plin1. Although designated as Plin1-EYFP S492A S517A, sequencing showed three mutated phosphorylation sites: S433A, S492A and S517A (see Figure 63). As the mutated version was to be used for analyzing the effect of various phosphorylation sites of Plin1, and PKA phosphorylates Plin1 at six different serine residues (S81, S222, S276, S433, S492, and S517) the modification of the protein was protocolled and this Δ3-version of Plin1 was not changed any further [138].

All other received template plasmids did not contain any undesired mutations and were therefore ready for use in further experiments. Figure 38 – Figure 65 in the appendix contain all sequencing results before and after successful SDM reactions.

In conclusion, plasmids containing wild-type and mutated versions of all proteins necessary for the following experiments were correctly prepared and stored ready for further use. The respective sequencing results of all constructs can be found in the appendix. Site-directed mutation via kit displays a fairly easy and convenient possibility to introduce single mutations into plasmids and after the implementation of control steps, as well as the optimization of the process, the production of mutated molecules in a very short period of time was achieved.

COS-7 Immunomicroscopy – Part II

Background

The aim of the conducted fluorescence- and immunofluorescence microscopy experiments was a functional analysis of CGI-58 phosphorylation and docking sites regarding the mechanism of regulation in more detail. As described in the former chapter, different versions of native and fluorescently tagged CGI-58 and Plin1 were generated through SDM-reactions. To analyze the subcellular co-localization and protein interaction under basal and stimulated lipolysis conditions in dependence of phosphorylation, different combinations of wild-type and mutated versions of those proteins were transiently co-expressed in COS-7 cells. In this chapter, first attempts of co-expression in COS-7 cells are going to be discussed, with a special focus on difficulties that arose during the development of the protocol. Examples of fluorescence- and immunofluorescence micrographs are shown, the outcomes of conducted experiments are discussed and compared with other studies.

Experimental procedure

Cell culture

COS-7 (ATCC® CRL-1651™) cells were cultured in Dulbecco's Modified Eagle's Medium (DMEM) supplemented with 10% FBS, 100 units/ml penicillin and 100 µg/ml streptomycin (DMEM+/+) following general procedures [139, 140] .

Preparation of COS-7 cell lysates for SDS-PAGE

To check endogenous protein levels, COS-7 cells were seeded in T-75 flasks and trypsinized at approximately 70-80% confluency. The cell pellet was washed, and the cells were resuspended in 20mM TrisHCl pH 7.5. After sonication and centrifugation, the protein content was estimated via Bradford method. COS-7 lysates containing 50 µg and 25 µg of total protein were loaded on the gel.

To check the overexpression of the fluorescently-tagged proteins, COS-7 cells were seeded in 6-well plates. After 24 hours, transfection was conducted after COSFect protocol [141]. 24 hours after transfection, the cells were trypsinized and centrifuged (800xg/ 5min/ room temperature (RT)). After washing with PBS and another centrifugation step (800xg/ 5min/ RT), the cell pellet was resuspended in 100 µL sample buffer containing reducing agent (Thermo Fisher Scientific). After sonication, the samples were heated to 70 °C for 10 minutes and loaded on the gel after centrifugation (14000 rpm/ 10 min/ RT).

Preparation of control samples for SDS-PAGE

Murine BAT-, murine WAT-, and murine liver lysates were kindly provided by Linda Waldherr and used as positive controls for the Western blot analysis. Because of lysate buffer properties, protein precipitation with trichloroacetic acid (TCA) had to be conducted to prepare the SDS gel samples. 400

µL of H_2O-diluted lysate (100 µg protein) were mixed with 100 µL 50% TCA, vortexed and incubated on ice for an hour. After centrifugation (4°C/10 min/14000 rpm), the supernatant was discarded, and the pellet was washed with ice cold acetone (1 mL). After another centrifugation step (4°C/10 min/14000 rpm), the pellet was air dried and then resuspended in sample buffer. The samples were sonicated and heated to 70 °C for 10 minutes.

SDS-PAGE and Western blotting

SDS-PAGE and immunoblotting on nitrocellulose membrane were performed using standard procedures as follows. Samples were prepared for SDS-PAGE analysis by mixing the respective sample volume with sample buffer (NuPAGE LDS Sample buffer (4X), Thermo Fisher) and reducing agent (NuPAGE Reducing Agent (10x), Thermo Fisher), adjusting to final volume with water. After heating the samples to 70°C for 10 minutes, the samples were loaded on 4-12% Bis-Tris Gels (Thermo Fisher). 7 µL of Novex Sharp Pre-Stained Protein standard (Thermo Fisher, Cat. No. LC5800) were used as molecular weight standard [142]. Gels were run at 200 V for 45 minutes in 1x running buffer (20X NuPage MOPS SDS Running Buffer by Thermo Scientific diluted with water). Subsequently, the gels and nitrocellulose membranes (Thermo Fisher) were equilibrated in transfer buffer (48 mM Tris-HCl, 39 mM glycine, 0.0375% SDS, 20% Methanol, pH 9.2) for 30 minutes and then transferred on the semi-dry blotter (Trans-Blot SD Semi-Dry Transfer Cell, Bio-Rad) for 1 hour at 180 mA without exceeding a voltage of 25 V. After Ponceau S staining, the blots were blocked using either 5% skim milk in TBS-T, 3% BSA in TBS-T, or protein free blocking solution as blocking agents. After 1 hour of blocking at room temperature and a brief washing step with 1X TBS-T, the blots were incubated with the respective primary antibodies over night at 4 °C. Antibodies were diluted with the previously used blocking agent following company protocol. After three washing steps with 1X TBS-T for 10 minutes, the blots were incubated with the respective secondary antibodies, diluted with blocking agent (following company protocol) for 1 hour at room temperature. Proteins were detected using enhanced chemiluminescence reagents and the Bio-Rad Chemidoc System.

Antibodies used for the immunoblotting were anti-CGI-58 mouse monoclonal antibody (Abnova, Cat. No. H00051099-M01), anti-Perilipin-1 rabbit polyclonal antibody (Abcam, Cat. No. ab 3526), anti-ATGL rabbit monoclonal antibody (Cell signaling, Cat. No. 2138S) and anti-Plin5 rabbit polyclonal antibody (Abnova, Cat. No. PAB 12542). Proteins were detected using horseradish peroxidase linked secondary antibodies (Cell Signaling, Cat. No. 7074S and 7076S) and enhanced chemiluminescence reagents (GE Healthcare, Cat. No. RPN 2018).

Choice of transfection reagent and β-galactosidase assays

To test the transfection efficiency of various transfection reagents with COS-7 cells, β-galactosidase assays were conducted with three different transfection reagents: COSFect, FuGENE6® and

Lipofectamine3000 [141, 143, 144]. COS-7 cells were seeded in 24 well plates. The transformations with β-galactosidase expressing lacZ vector [145] were conducted according to the protocol of each aforementioned transfection reagent [141, 143, 144]. COSFect was used in ratios 1:1 and 2:1 (µl reagent: µg DNA), FuGENE6 in ratio 6:1, and Lipofectamine in ratios 6:1 and 1.5:1. To determine the influence of the transfection reagent on the cells over time, the transfection reagent was removed after either 4 hours or 22 hours. 24 hours after transfection, the cells were fixed with 4% formaldehyde in PBS and the β-galactosidase-assay was performed. The cells were washed with PBS and 200µL of 0.2% 5-bromo-4-chloro-3-indolyl-beta-galaktopyranoside (x-Gal) in reaction solution (10mM Phosphate-buffer (pH7), 150mM NaCl, 1mM $MgCl_2$, 3.3mM $K_4Fe(CN)_6$ *3 H_2O, 3.3mM $K_3Fe(CN)_6$) were added to each well. After incubation at 37°C for approximately 30 minutes and washing with PBS, pictures were taken on an Olympus IX51 inverted microscope.

Fluorescence microscopy using the Olympus IX51 inverted microscope

In early stages of the experiments, the expression of plasmids and their co-expression in COS-7 had to be checked. Plasmids containing wild-type mCGI-58-mCherry, wild-type ECFP-ATGL and wild-type Plin5-EYFP were used in these experiments (see chapter 1 for details). COS-7 cells were cultured following standard procedures. Cells were seeded in either 6-well or 24-well plates and, 24 hours after seeding, transfection with Fugene6 was conducted following protocol [143]. After primarily achieving successful transfection with the individual plasmids, co-transfection with the plasmid containing mCGI-58-mCherry and the Plin5-EYFP was conducted. 24 hours after transfection, the expression of the respective proteins was checked via fluorescence microscopy using the Olympus IX51 inverted microscope. Used fluorescence filters are shown in Table 2.

*Table 2: **Filterset of Olympus IX51 inverted microscope** with excitation- and emission wavelengths and the respective fluorophores visualized within conducted experiments*

Filter Name	Excitation Wavelength [nm]	Emission Wavelength [nm]	Dichroic Mirror [nm]	Used for fluorophore
U-MWIB2	460-490	510 IF	505	ECFP/EYFP
U-MWIG2	520-550	580 IF	565	mCherry

Fluorescence microscopy

COS-7 cells were seeded in 24-well glass bottom plates. After 24 hours, the cells were transfected following COSFect protocol using a ratio of 2:1 of µl COSFect-reagent to µg DNA [141]. For co-transfections, 0.2 µg of each corresponding plasmid, thus 0.4 µg of DNA in total, were mixed with 0.8 µL of COSFect reagent per well. 24 hours after transfection, cells were washed with PBS and in the next step, lipid loading was performed, using DMEM+/+ containing 200 µM oleic acid complexed to fatty acid free BSA at a 4:1 molar ratio [146]. To stimulate lipolysis, 36 hours after transfection cells were

incubated with 10 µM forskolin and 0.5 mM IBMX in DMEM containing 2% fatty acid free BSA for 30 minutes. For basal conditions, cells were incubated with DMEM containing 2% fatty acid free BSA for 30 minutes. Cells were fixed with 4% formaldehyde in 1X PBS for 30 minutes at room temperature. After washing the cells 4 times with 1X PBS, lipid droplets staining was obtained using either LipidTox Deep Red (Thermo Fisher Scientific, Cat. No. H34477) in a 1:500 dilution in 1X PBS or Bodipy 439/503 (Thermo Fisher Scientific, Cat. No. D3922) at a final concentration of 1 µg/mL in 1X PBS for 30 minutes at room temperature under light exclusion. Nuclei were stained with Hoechst33342 (Thermo Fisher Scientific, Cat. No. H3570) at a final concentration of 60µg/mL in 1X PBS for 5 minutes at room temperature under light exclusion. After washing 3 times with 1X PBS, the cells were examined with the Nikon A1 confocal laser scanning microscope (CLSM) system using a CFI Apochromat Lambda S 60 x Oil objective (Apo 60x Oil λS DIC N2; NA: 1.4). Optical sections were taken at 0.4 µm z-axis intervals. Representative micrographs show a maximum intensity z-projection. The channels used for each fluorophore or dye are summarized in Table 3. Images were processed using ImageJ software using the processing package Fiji.

Table 3: ***Channel settings used for fluorescence microscopy on Nikon A1 confocal laser scanning system***

Channel Name	Excitation Wavelength [nm]	Emission Wavelength [nm]	Channel modality
Hoechst33342	402.6	500/550	Laser Scan Confocal, PMT
eGFP	488.0	570/620	Laser Scan Confocal, GaAsP
mCherry	561.3	663/738	Laser Scan Confocal, GaAsP
LipidTox	642.6	663/738	Laser Scan Confocal, PMT
TD	488.0	N/A	Laser Scan Confocal, TD

Immunofluorescence Microscopy

COS-7 cells were prepared as mentioned in the previous paragraph up to fixation. After fixation, cells were washed with 1X PBS four times to remove all formaldehyde and then blocked with 1X PBS containing 0.1% Tween20 and 2% skim milk for 1 hour at room temperature. All antibody dilutions were prepared using antibody diluent (1X PBS containing 0.1 mg/ml saponin and 2% BSA). After washing the cells with antibody diluent 2 times, primary antibody incubation with a 1:200 dilution of anti-CGI-58 mouse monoclonal antibody (Abnova, Cat. No. H00051099-M01) and a 1:200 dilution of anti-Perilipin-A rabbit polyclonal antibody (Abcam, Cat. No. ab 3526) overnight at 4°C was conducted. After washing 4 times for 10 minutes with 1X PBS, the cells were incubated with a 1:5000 dilution of anti-rabbit Alexa Fluor 647 (Molecular Probes, Cat. No. A31573) and a 1:500 dilution of Cy3-marked goat polyclonal secondary antibody to mouse IgG (Abcam, Cat. No. ab97035) for 1 hour at room temperature under light exclusion. After washing, nuclei and lipid droplets were stained with Hoechst33342 and Bodipy 439/503 (see former paragraph for details) and 2 final washing steps with

1X PBS were performed. Then, the cells were examined with the Nikon A1 confocal laser scanning microscope system, as mentioned in the previous paragraph, using the channels in Table 4. Images were processed using ImageJ software using the processing package Fiji.

Table 4: ***Channel settings used for immunofluorescence microscopy on Nikon A1 confocal laser scanning system***

Channel Name	**Excitation Wavelength [nm]**	**Emission Wavelength [nm]**	**Channel modality**
DAPI	402.6	500/550	Laser Scan Confocal, PMT
BODIPY 493/503	488.0	570/620	Laser Scan Confocal, GaAsP
Cy3 dye–labeled IgG antibody/pH 7.2	561.3	663/738	Laser Scan Confocal, GaAsP
Alx647	642.6	663/738	Laser Scan Confocal, PMT
TD	488.0	N/A	Laser Scan Confocal, TD

Part II: Results and Discussion

Fluorescence- or immunofluorescence microscopy have for some time been the go-to methods to analyze protein-protein interactions. The examination of the interplay of several components of the lipolytic apparatus in vivo displays an important step to elucidate the complicated process in its full extent. The experiments involved cell culture, cell transformation, lipolysis stimulation, and, in the end, the visualization of either fluorescence or immunofluorescence. The many steps taken in this process are now to be discussed regarding the achieved results and possible troubleshooting techniques.

Pre-Tests of Fluorescence and Immunofluorescence experiments

COS-7 cells

The mammalian expression system chosen for these experiments was the COS-7 cell line, as it was used in previously conducted studies regarding this topic [17, 50, 79]. It derived from kidney cells of Cercopitheous arthiops, the African green monkey, and was obtained by the transformation of CV1-cells with an origin-defective version of the SV40 virus, which codes for wild-type T antigen [147]. Its name originates from **C**V-1 in **O**rigin with **S**V40 genes [140]. As COS-7 cells had been used frequently before, standard protocols for the transformation, expression and visualization had already been established and only fine-tuning of the individual steps had to be accomplished.

Endogenous protein levels in COS-7 cells

Before starting the overexpression experiments in COS-7 cells, endogenous expression of the proteins of interest had to be checked making sure endogenous proteins would not affect the experiments. To check these levels, COS-7 lysates and positive controls for each protein of interest were examined via Western blot analysis.

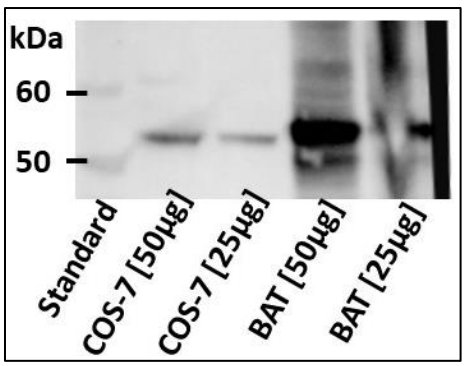

*Figure 8: **Endogenous ATGL is expressed in COS-7 Lysates**. Endogenous protein expression was analyzed in whole COS-7 cell lysates (50/25 µg of total protein loaded) by immunoblotting with anti-ATGL rabbit monoclonal antibody. Murine brown adipose tissue (BAT) lysates (50/25 µg of total protein loaded) were used as positive controls. mATGL size: 53.657 kDa.*

Murine BAT was used as positive control to check expression of ATGL, since murine ATGL (mATGL) is highly expressed in murine WAT and BAT [10]. The used antibody detects endogenous levels of total murine and human ATGL, and would also be predicted to react with rat ATGL due to sequence homology. Since no epitope sequence was provided by Cell Signaling, it was assumed that endogenous ATGL expressed in COS-7 cells would also be detected due to sequence homology [148]. As mATGL has a mass of 53.657 Da [137] and a strong signal at the molecular weight of approximately 55 kDa can be seen in all of the lanes (see Figure 8), it was concluded that endogenous ATGL is present in all of the examined samples, though at lower expression levels in

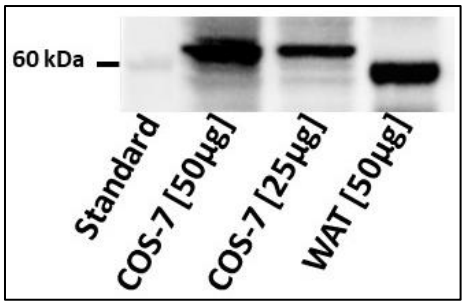

Figure 9: ***Endogenous Plin1 may be expressed in COS-7 Lysates.*** *Endogenous protein expression was analyzed in whole COS-7 cell lysates (50 µg of total protein loaded) by immunoblotting with anti-Perilipin-1 rabbit polyclonal antibody. Murine white adipose tissue (WAT) lysates (50/25 µg of total protein loaded) were used as positive controls. mPlin1 size: 55.596 kDa.*

COS-7 lysates. Since the expression of functioning ATGL in virtually all organs has been previously shown [149], it was not completely unexpected to show endogenous expression in this mammalian system.

Plin1 expression was checked using murine WAT lysate as positive control, since significant expression of perilipin 1 had been established in adipocytes of white and brown adipose tissue [19]. Murine Plin1 has a molecular weight of 55.596 kDa [150]. The positive control (WAT) (see Figure 9) shows a strong band at approximately 55 kDa, which fits the expected mass. The COS-7 lysate shows various bands but the strongest one at 60 kDa seems to be too high to fit the molecular weight of Plin1. The used antibody (Abcam, Cat. No. ab 3526) binds to the epitope "EPILGRTQYSQLRKKS". A search in the NCBI-database showed no entries concerning perilipin 1 in Cercopithecus Aethiops so no comparison was possible and an additional search of the epitope sequence against a protein database of the original organism led to no results. However, Kimmel et al. report that mammalian proteomes contain several forms of Plin [94]. As COS-7 cells are mammalian kidney cells, it stands to reason that some form of Plin could be expressed and may be visualized with the used antibody, due to the sequence homology mammalian Plins share [94]. Additionally, the used polyclonal antibody by definition contains different isotypes of immunoglobulins showing varying degrees of affinity to different epitopes of the antigen, so it is possible that, if other types of perilipins are present in the cell, the antibody could bind other epitopes of those as well [133]. Furthermore, this would explain the unspecific bands produced in both WAT- and COS-7 lysates (not shown). In conclusion, Perilipin 1 could be expressed in COS-7 cells and if the same antibody is used in immunofluorescence, unspecific or endogenous proteins could possibly be detected, which is why the use of a monoclonal antibody could be taken into consideration in subsequent experiments.

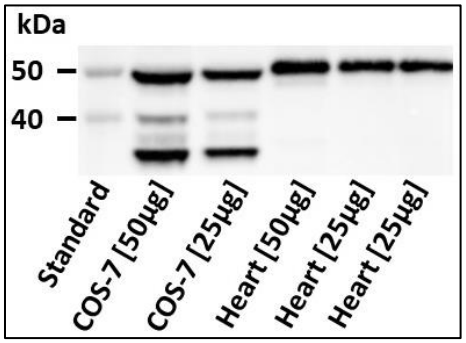

Figure 10: ***Endogenous Plin5 could be present in COS-7 Lysates.*** *Endogenous protein expression was analyzed in whole COS-7 cell lysates (50/25 µg of total protein loaded) by immunoblotting with anti-Plin5 rabbit polyclonal antibody. Murine heart tissue lysates (50/25 µg of total protein loaded) were used as used as positive controls. mPlin5 size: 54.474 kDa*

Plin5 is highly expressed in oxidative tissues, such as heart, liver and BAT, so murine heart tissue lysate was used as positive control [109, 110]. Murine Plin5 (mPlin5) has a molecular weight of 50.474 kDa [108]. All lanes in Figure 10 show a strong band at approximately 50 kDa, which fits the expected mass. Similar signal intensity would suggest equal expression levels of Plin5 in all cell types, since the loaded amount of total protein was identical. The COS-7 lysate band is slightly lower than the ones in the positive control, which

could be explained by the fact that the sequence of Plin5 expressed by COS-7 cells varies. The COS-7 lysates also show a strong band at approx. 35 kDa, which could be accounted to low specificity of the antibody, the type of the antibody (polyclonal) or the fact that expression of other Plins in mammalian cells would not be surprising, as mentioned above. Nevertheless, if the absence of Plin5 is critical, further experiments must be conducted to assure that endogenous Plin5 is not present in COS-7 cells or another cell type has to be chosen for expression. Additionally, the use of a monoclonal antibody could be taken into consideration.

CGI-58 is highly expressed in adipose tissue which is why murine WAT lysate was chosen as positive control for CGI-58 expression [50, 62]. Additionally, purified murine CGI-58 was used as a second positive control. The positive controls in Figure 11 both show bands at approximately 40 kDa, which fits the expected mass of 39.155 Da [61]. The COS-7 lysates show faint bands at approximately 45 kDa. It is assumed that this signal is too high to represent CGI-58. As the same amounts of total protein were loaded on the gel for either COS-7- or WAT-lysates, the signals in the COS-7 lanes are quite faint, in comparison to the control band. In the case of my experiment, the expression of the desired proteins after transfection would ideally lead to the production of large amounts of the proteins, which is why it was decided that the amount of endogenous CGI-58, if actually present, should be negligible. COS-7 cells were used for CGI-58 overexpression in previous experiments by various groups, so it was assumed that no significant amount of endogenous CGI-58 is present in the cells [17, 50, 79].

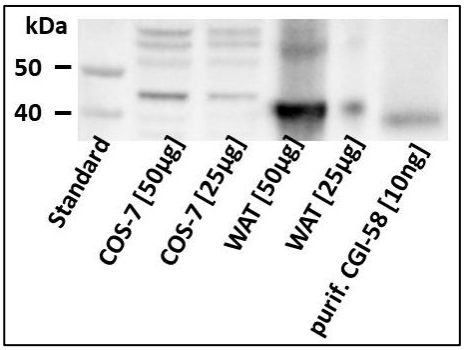

*Figure 11: **Endogenous CGI-58 could be present in COS-7 Lysates.** Endogenous protein expression was analyzed in whole COS-7 cell lysates (50/25 µg of total protein loaded) by immunoblotting with anti-CGI-58 mouse monoclonal antibody. Murine white adipose tissue (WAT) (50/25 µg of total protein loaded) lysates were used as positive controls. mCGI-58 size: 39.155 kDa*

To conclude, the examination of endogenous protein expression in COS-7 cells did not lead to definite results. ATGL expression was detected and the possibility of endogenous expression of Plin1, Plin5 and CGI-58 cannot be excluded via Western blot analysis. For further studies, it would be recommendable to examine COS-7 lysates via other analysis methods, to conclusively show the endogenous expression of proteins involved in desired experiments, consecutively assuring the exclusion of possible interferences of endogenous proteins with results. As various groups had already used COS-7 cells for similar experiments, the handy expression system was nevertheless used for further experiments [17, 50, 79].

Check of protein expression in COS-7 cells after transfection

To check protein expression after co-transfection, COS-7 cells were transfected with two different plasmids: One containing a version of CGI-58-mCherry (wild-type (WT), Y330F, S239A or S239A Y330F) and the other coding for either the Plin1-EYFP WT or the Plin5-EYFP WT gene. Cells were harvested after 24 hours via trypsinization and the lysates were prepared for Western blot analysis according to protocol. 3 blots were prepared using the same lysates to check the expression of every protein. All expressions in COS-7 cells were conducted using plasmids containing the murine versions of the proteins.

To check CGI-58-mCherry expression, descending amounts of purified murine CGI-58 were loaded as a positive control (20, 10 and 5 ng). The very intense signal in lane 4 (20 ng purified CGI-58) at ~40 kDa fits the theoretical size of mCGI-58 (see Figure 12). The strong band at 80 kDa is assumed to be the dimer of the purified protein. All the lanes containing the double-transfected COS-7 samples show strong bands at ~65 kDA, ~58 kDA and ~50 kDa. The expressed versions of CGI-58 contained a mCherry-tag, which has an approximate molecular weight of 26.722 kDa, leading to the total size of ~65.8 kDA for the heterologously expressed protein [151]. As the highest band fits the size of the total construct, it is assumed that the other strong bands represent forms of the constructs that lost parts of the tag in the process of SDS-PAGE sample preparation. The cell lysates containing the mCGI-58-mCherry S239A- construct and the COS-7 control sample only show very faints signals. As the transfection was checked via Ponceau staining (data not shown), and all the lanes the blot displayed similar intensities, it is assumed that the S239A mutated version of CGI-58 was most probably expressed to a lower extend. Poor plasmid quality could be a possible reason for this, which is why a newly prepared plasmid was used in further experiments. Nevertheless, the expression of CGI-58 in all the samples was present and it was concluded that further experiments could be conducted.

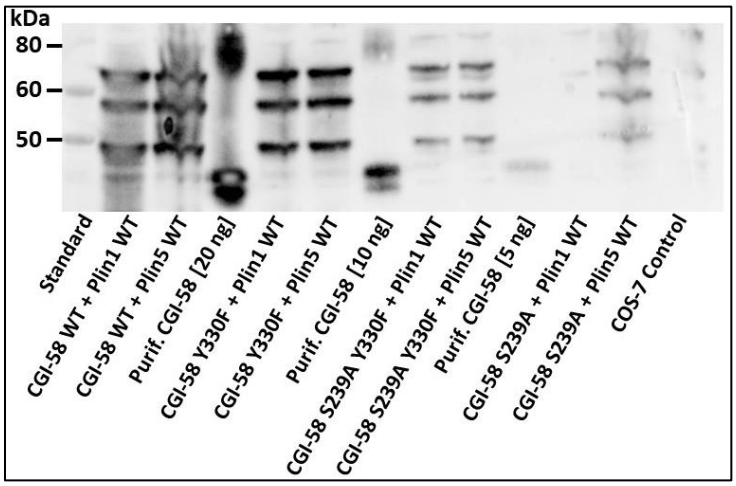

Figure 12: ***Analysis of expression of CGI-58-mCherry-variations in co-transfected COS-7 cells****. Expression of CGI-58 was analyzed in co-transfected COS-7 cell lysates by immunoblotting with anti-CGI-58 mouse monoclonal antibody. COS-7 cells were co-transfected with one plasmid containing a version of CGI-58-mCherry (WT, Y330F, S239A or S239A Y330F) and the other plasmid containing either Plin1-EYFP WT or Plin5-EYFP WT. Purified murine CGI-58 was used as positive control. mCGI-58 size: 39.155 kDa; mCGI-58-mCherry size: ~65.8 kDa*

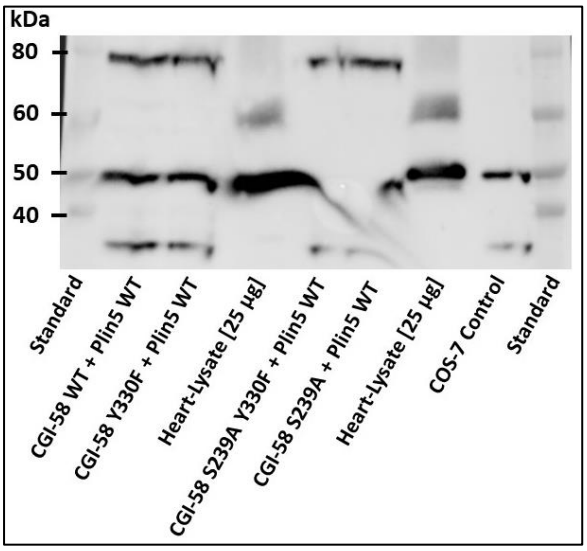

Figure 13: ***Analysis of Plin5-EYFP expression in co-transfected COS-7 cells****. Expression of Plin5 was analyzed in co-transfected COS-7 cell lysates by immunoblotting with anti-Plin5 rabbit polyclonal antibody. COS-7 cells were co-transfected with one plasmid containing a version of CGI-58-mCherry (WT, Y330F, S239A or S239A Y330F) and the other plasmid containing Plin5-EYFP WT. Murine heart lysate was used as positive control. mPlin5 size: 50.474 kDa; mPlin5-EYFP size: ~78.5 kDa*

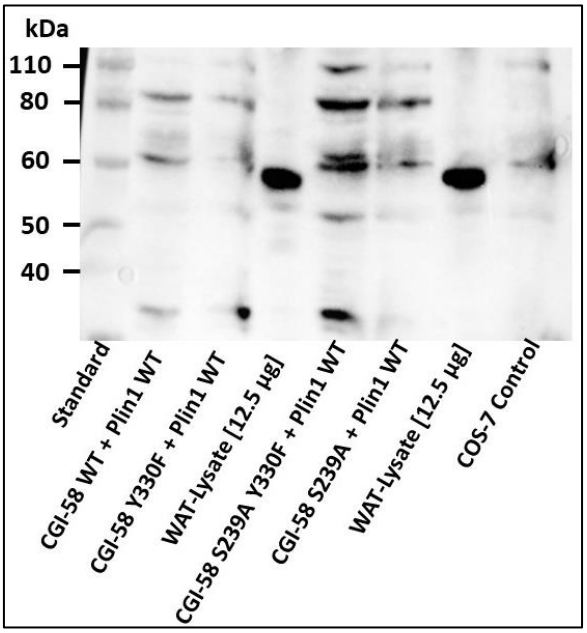

Figure 14: ***Analysis of Plin1-EYFP expression in co-transfected COS-7 cells****. Expression of Plin1 was analyzed in co-transfected COS-7 cell lysates by immunoblotting with anti-Perilipin-1 rabbit polyclonal antibody. COS-7 cells were co-transfected with one plasmid containing a version of CGI-58-mCherry (WT, Y330F, S239A or S239A Y330F) and the other plasmid containing Plin1-EYFP WT. Murine white adipose tissue (WAT) (12.5 µg of total protein loaded) lysate was used as positive control. mPlin1 size: 55.596 kDa; mPlin5-EYFP size: ~83,5 kDa*

The blot in Figure 13 displays all lysates co-expressing CGI-58-mCherry variants and Plin5-EYFP. Murine heart lysate was used as a positive control. The positive control produced strong bands at the correct height of ~50 kDa [108]. A smear appears in lanes 4-6, which renders the bands in this area useless, since the transfer from gel to membrane did not work properly. All double-transfected lysates show bands at ~80, ~50 and ~35 kDa. The signal at 80 kDa fits the size of the intact Plin5-EYFP-construct, containing the 50.474 kDa Plin5 and its ~28 kDa YFP-tag (sequence obtained from UniProtKB), at a total molecular weight of 78.5 kDa [152]. The loss of the YFP-tag would account for the signal at 50 kDa. The signal at 35 kDa is present in all the COS-7 lanes, including the COS-7 control and the Westen blot analyzing endogenous Plin5 (see Figure 10), and the signal is most likely caused by poor antibody specificity. Regarding the signal intensity, the levels of endogenous Plin5 produced by the COS-7 control are only slightly lower than those of the overexpressed Plin5-EYFP construct, without taking into consideration that the total amount of overexpressed Plin5-EYFP is accounted for by the added-up amounts of the 80 kDa and the 50 kDa band. To carry on with experiments involving Plin5 it would be advisable to choose another cell model for expression.

Figure 14 displays the blot loaded with all lysates expressing CGI-58-mCherry and Plin1-EYFP. Murine WAT lysate was used as positive control which showed strong bands at the correct mass of ~56 kDa [150]. There is a second band in the positive control lane at ~110 kDa, which again could be explained by dimer building of the protein. All

double-transfected lysates show bands at ~80, ~60 kDa and ~35 kDa. The overexpressed Plin1 constructs were expressed with a YFP-tag, resulting in a total molecular weight of ~83.5 kDa which fits the highest band in the co-expression-lysate lanes. Again, the loss of the tag most probably accounts for the band at ~60 kDa but would be slightly higher than expected for Plin1 at ~ 56 kDa. The signals at 35 kDa most likely occur due to unspecific reactions of the antibody. It can be assumed that Plin1 is properly overexpressed in all COS-7 lysates but looking at the non-transfected COS-7 control sample it may be possible that Plin1 is endogenously expressed in COS-7 cells.

All in all, it can be concluded that all examined constructs were overexpressed in proper amounts and bound to their desired tags so further experiments could be conducted.

Determination of transfection reagent used via β-Galactosidase assay

Mammalian cells can be transfected using different mechanisms leading from virus-mediated, biological methods to chemical methods using cationic polymers or lipids and even physical principles, like direct injection, electro- or sonoporation, or even using magnetic nanoparticles, just to mention a few examples [153]. The ideal method would combine high transfection efficiency, low cell toxicity and minimal effects on the normal physiology with easy use and high reproducibility [153]. The availability of products or machines in the lab has to be taken into consideration as well. As our lab had worked with a lot of chemical methods using transfection reagents, like lipofectamine and FuGENE6, before, and these methods represent a fast and convenient way to transfect mammalian cells, it was decided to choose this method of transfection. As COS-7 was set as the cell model, research into the subject lead us to COSFect, a specialized transfection reagent for COS-cell lines. Factors influencing transfection rate, like cell health, viability, confluency, and presence of serum or antibiotics were all taken into consideration and ideal conditions for the transfections were guaranteed [141]. The final choice of transfection reagent was made by performing β-galactosidase assays. The colorimetric assay is based on the expression of β-galactosidase in cells transfected with a vector cloned with the LacZ gene and its reaction with 5-bromo-4-chloro-3-indolyl-beta-galaktopyranoside (x-Gal). In successfully transfected cells, x-Gal is cleaved to galactose and 5-bromo-4-chloro-3-hydroxyindole by β-galactosidase; the indole is further dimerized and oxidized to 5,5'-dibromo-4,4'-dichloro-indigo leading to a bright blue product that can be visually detected [154]. Additional to transfection efficiency, cell toxicity of the transfection reagents was checked. Early experiments had shown that incubation with various transfection agents over longer periods of time led to the death of a considerable number of cells. To check if a shorter amount of time would benefit the experiment regarding cell survival numbers, the assays were conducted under two conditions: Incubation with transfection reagent for 22 hours or exchange of the transfection mix with normal culture medium after 4 hours.

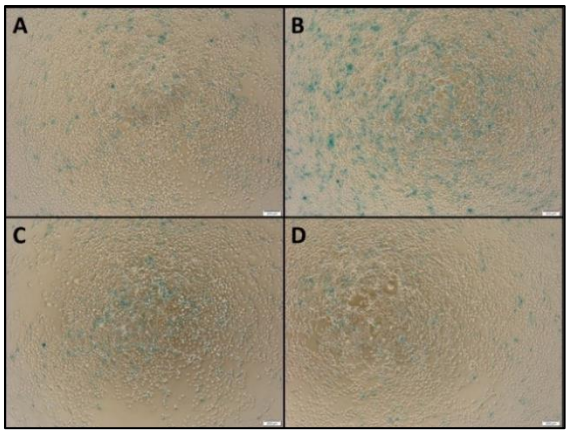

Figure 15: ***COSFect in ratio 2:1 delivered best transfection results in β-galactosidase assay after 4 hours of incubation.*** *COS-7 cells were grown under standard conditions. Transfection with LacZ-gene cloned in pcDNA HisMax C vector was performed with various transfection reagents. Transfection reagent mix was exchanged with culture medium after* ***4 hours*** *Scale bar: 200 µm.* ***A*** *Transfection with COSFect in ratio 1:1 (µl reagent: µg DNA)* ***B:*** *Transfection with COSFect in ratio 2:1* ***C:*** *Transfection with Lipofectamine in ratio 0.75:1* ***D:*** *Transfection with FuGENE6 in ratio 6:1*

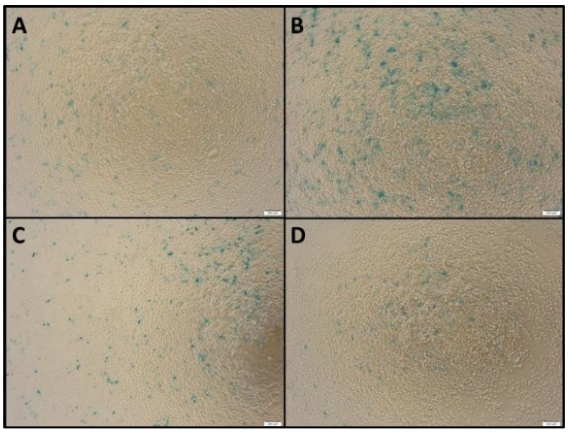

Figure 16: ***COSFect in ratio 2:1 delivered best transfection results in β-galactosidase assay after 22 hours of incubation.*** *COS-7 cells were grown under standard conditions. Transfection with LacZ-gene cloned in pcDNA HisMax C vector was performed with various transfection reagents. Transfection reagent mix was exchanged with culture medium after* ***22 hours****. Scale bar: 200 µm* ***A*** *Transfection with COSFect in ratio 1:1 (µl reagent: µg DNA)* ***B:*** *Transfection with COSFect in ratio 2:1* ***C:*** *Transfection with Lipofectamine in ratio 0.75:1* ***D:*** *Transfection with FuGENE6 in ratio 6*

Figure 15 shows the results of transfections with a medium change after 4 hours. It was observed that transfection with COSFect in a ratio of 2:1 led to the best transfection efficiency. Figure 16 shows the same pattern with no grave differences regarding cell survival caused by the lack of change of medium. Differences in confluency can be explained by the slight basin shape of the wells (higher cell density in the center) and that pictures were taken at varying positions within each well. Ultimately, COSFect (in the ratio 2:1) was used as transfection reagent in all following transfections and the incubation time for the reaction mix was set at 24 hours since no severe cell toxicity was observed.

Primary transfection tests – Fluorescence microscopy

For primary transfection tests, COS-7 cells were transfected with plasmids containing mCGI-58-mCherry, ECFP-ATGL and/or wild-type Plin5-EYFP. These primary tests served the purpose of checking if co-expression in COS-7 cells was detectable via fluorescence microscopy. Since visualization of nuclei, lipid droplets and all involved proteins has to be conducted with only a limited number of channels available to assure correct and concrete results, the set-up has to be designed thoughtfully.

As the first co-expression experiments were visualized on an Olympus IX51 inverted microscope, the properties of each fluorophore, excitation and emission spectra of the fluorescence tags, were compared to the instrument's available filter sets and chosen correspondingly. They are noted in Table 2 in experimental procedures. The filter settings of filter "U-MWIB2" corresponded best to fluorophore properties of ECFP and EYFP and filter "U-MWIB2" was chosen for visualization of mCherry-marked

constructs. Figure 17 shows the excitation (Ex; dotted lines) and emission (Em; continuous lines) spectra of the three fluorophores.

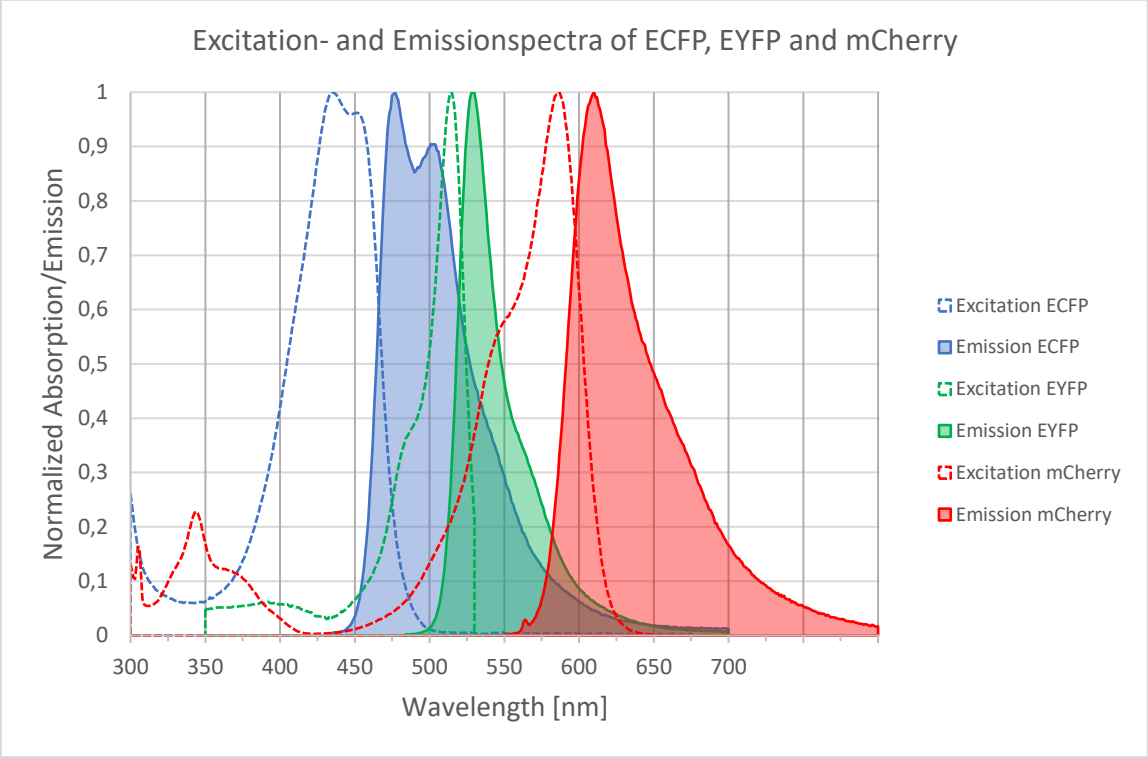

Figure 17: ***Excitation and emission spectra of ECFP (blue), EYFP (green) and mCherry (red).*** *Spectrum data obtained from https://www.fpbase.org/. ECFP: Excitation Maximum (Ex_{Max}): 435nm, Emission Maximum (Em_{Max}): 475 nm); EYFP: Ex_{Max}: 514 nm; Em_{Max}: 527 nm; mCherry: Ex_{Max}: 587 nm; Em_{Max}: 610 nm)*

Regarding the filter settings (see Table 2 in experimental procedures of this chapter), the excitation wavelength of filter "U-MWIB2" at 460-490nm could, to a certain extent, excite either ECFP, EYFP or mCherry, which could possibly lead to excitation crosstalk, a phenomenon occurring when multiple fluorophores are excited with a single excitation wavelength [155]. Regarding the fact that the filter "U-MWIB2" is a long pass filter and detects emissions of higher wavelengths than 510 nm, the detection of ECFP-, EYFP- and mCherry signals is possible. However, the mCherry signal would be considerably fainter, since the excitation of mCherry at wavelengths between 460 and 490 nm would result in an excitation efficiency of maximum 8.41%, compared to the excitation of either ECFP, with an excitation efficiency maximum of 85.73%, or EYFP, with a maximum of 39.04%. As the constructs were provided and had previously been used by Dr. Granneman and his team, literature concerning microscopy experiments with these tagged proteins was studied. In 2005, Moore et al. visualized the co-expressed ECFP- and EYFP-tagged proteins using Argon lasers at 458 and 514 nm respectively for the excitation and band pass filters from 480-520nm for ECFP and 535-590nm for EYFP [156]. In these settings, EYFP would be excited with 87.83% efficiency and ECFP with 87.14% in their respective channels. However, regarding the spectra of each fluorophore, it can be obtained that the excitation at 458 nm and 514 nm would lead to excitation of both fluorophores, which leads to a possibility of

crosstalk. To be more precise, the settings used for the ECFP-construct would lead to 6.2% crosstalk produced by EYFP and the ECFP construct would lead to 0.2% crosstalk in the EYFP-channel. These factors have to be taken in to consideration for correct evaluation of the results. Since, in the case of my experiments, the used set-up for the Olympus IX51 inverted microscope was only used for pre-tests and not for further experiments, it was not further optimized.

The overlap of emission and excitation spectra of different fluorescence tags can of course also be used to one's advantage, taking into account the examination of protein interaction via Förster resonance energy transfer (FRET). In fact, Granneman et al. used this approach in 2009 to examine ECFP-CGI-58 dispersion from PlinA-EYFP after PKA-stimulation of lipolysis in 3T3-L1 cells, whereby the disruption of the FRET signal, which was previously created by the co-localization of the two tagged proteins, proved the delocalization of CGI-58 [17, 102]. Another elegant solution concerning the validation of protein interaction would be Bimolecular Fluorescence Complementation or BiFC. The principle of this method lies in the fusion of a non-fluorescent fragment of a reporter-protein (for instance EYFP) to the proteins whose interaction one would like to examine. In case of YFP, one interaction partner would be attached to an N-terminal (Yn) - and the other to a C-terminal (Yc) fragment of the reporter. If in close enough proximity, the fragments form the fully fluorescent reporter-protein and interaction of the two parts can be confirmed [102, 157]. The method is even sensitive to the orientation of the interacting proteins which was underlined by an experiment conducted by Granneman et al. using CGI-Yn and Plin-Yc constructs. Having used combinations of either N-terminal of C-terminal tags for either of the proteins, the group showed that the interaction between CGI58-Yn and Plin-Yc led to the most intense signal for all tested combinations, proving specificity of their interaction regarding their orientation towards each other [102].

Figure 18 displays COS-7 cells successfully co-transfected with both fluorescently-tagged proteins, whereas the green signals in Figure 18B represent Plin5-EYFP and Figure 18C shows red signals for CGI-58-mCherry. Since this experiment served the sole purpose of showing if co-expression is possible and detectable, no pictures with higher resolution were taken. Straightaway, the micrographs in Figure 18 B and C seem identical, regardless of the different colors. At this magnification, merely the whole cell is visible, and, with the used filter settings, crosstalk of approximately 19.95% is possible. Nevertheless, regarding the fact that the co-expression had also been confirmed via Western blot and the signals of each channel were very well defined, it was assumed that co-expression had worked and experiments were resumed using microscopes equipped with more sophisticated technical properties, to analyze the protein's subcellular localization in further experiments.

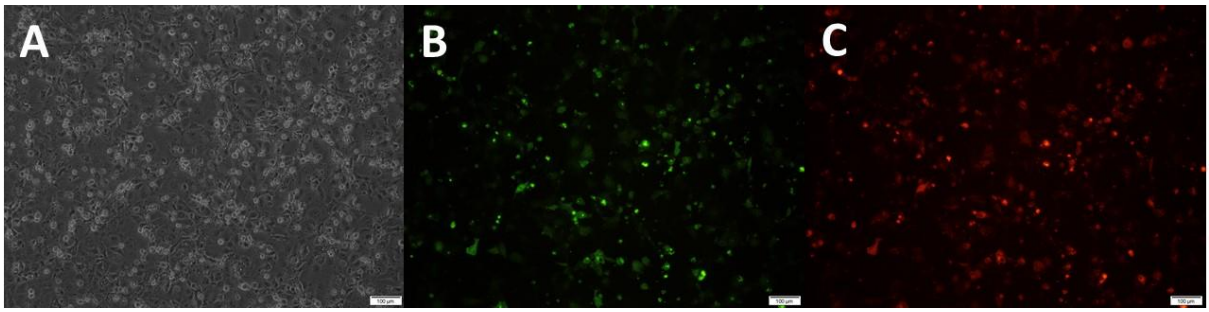

Figure 18: ***mCGI-58-mCherry and Plin5-EYFP expression of transfected COS-7 cells.*** *COS-7 cells were seeded in 6-well plates. After 24 hours transfection with 2 µg EYFP-N1 plasmid containing FL-Plin5-EYFP and 2 µg EYFP-N1 plasmid containing mCGI-58-mCherry per well. Visualization 24 hours after transfection via Olympus IX51 inverted microscope with 10x CPlan FL, 0.3 PhC, NA 0.3 objective. A: Brightfield B: U-MWIB2 fluorescence filter. YFP-tag: Exposure time: 200ms, well defined signals. C: U-MWIG2 filter. mCherry-tag: Exposure time: 200ms, well defined signals. Scale Bars: 100 µM*

The CGI-58-mCherry- and Plin5-EYFP constructs showed promising results; however, the expression of ECFP-ATGL had yet to be shown. Repetitive tests of ECFP-ATGL expression in COS-7 cells via fluorescence microscopy showed poor results, producing only very faint signals (see Figure 19B). Although problematic, the combination of filter-fluorophore properties (MWIB2 filter) should have led to detectable fluorescence signals, if the fluorescently-tagged protein had been expressed strong enough. As the intensity of the signal was very low, compared to earlier experiments with EYFP and mCherry, it was decided that the problem regarding the expressed protein did probably lie elsewhere, which meant that the construct had to be examined in greater detail.

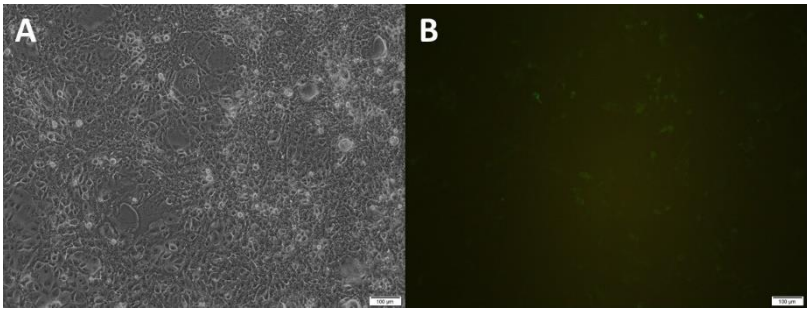

Figure 19: ***Very low ECFP-ATGL expression in transfected COS-7 cells.*** *COS-7 cells were seeded in 24 well plates. After 24 hours transfection with 0.5 µg ECFP-C1 plasmid containing ECFP-ATGL per well. Visualization 24 hours after transfection via Olympus IX51 inverted microscope with 10x with 10x CPlan FL, 0.3 PhC, NA 0.3 objective.* ***A*** *Brightfield* ***B*** *U-MWIB2 fluorescence filter. Exposure time: 200ms. Very faint signals can be obtained. Exposure time: 200 ms. No fluorescence signals present. Scale Bar: 100µm*

The first possible error sources that came to mind were either poor plasmid quality, due to incorrect preparation or poor storage conditions, or a damaged sequence of the CFP-tag (only the ATGL sequence was checked via sequencing but not the ECFP-tag itself). As new plasmid preparations were tested and did not lead to better fluorescent signals (not shown), it was decided to check protein expression. ECFP-ATGL-transfected COS-7 cells were harvested, and a Western blot analysis of the lysate was performed. Murine BAT-lysates with total proteins amounts of 5, 10 and 25 µg were used as positive controls. To exclude plasmid preparation as cause of the problem, two different preparations of ECFP-ATGL were examined. Signals can be detected at approximately 55 kDa in the

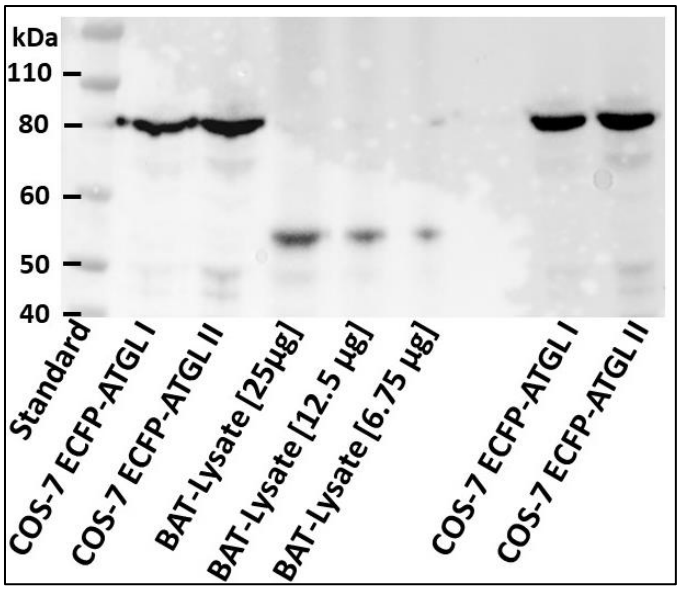

Figure 20: ***ECFP-ATGL is expressed in transfected COS-7 cell lysates****. Overexpression of ECFP-ATGL was analyzed in transfected COSos-7 cell lysates by immunoblotting with anti-ATGL rabbit monoclonal antibody. COS-7 cells were transfected with wild-type ECFP-ATGL. ECFP-ATGL I and II refer to 2 different plasmid preparations, prepared on different dates to control plasmid preparation. Murine brown adipose tissue (BAT) lysate (25/12.5 µg of total protein loaded) was used as positive control for ATGL. mATGL size: 53.657 kDa. ECFP-mATGL size: 82.6 kDA*

lanes of the positive control (BAT-lysate), which fits mATGL's molecular weight of 53.6 kDa. As the expressed ATGL construct contains a CFP-tag, which has a mass of approximately 29 kDa, ECFP-ATGL should have a total mass of 82.6 kDa [158]. Therefore, the blot clearly shows ECFP-ATGL expression in COS-7 after transfection with both plasmid preparations and expression failure can be excluded as the reason of non-present fluorescence after transfection. Since no sequencing data of the ECFP-tag was available, it would be possible that somewhere in the process of expression, the functionality of the ECFP-tag is lost, since the Western blot results most likely represent the expression of a complete product. Considering the problems with visualization, the apparent possibility of crosstalk with other fluorophores and the fact that endogenous protein expression of ATGL in COS-7 cells was shown earlier, it was decided that no transient co-expression of ECFP-ATGL during the following experiments would be conducted.

To summarize the pre-tests: The co-expression of CGI-58-mCherry and Plin1-EYFP constructs showed promising result. Taking into account that endogenous expression of ATGL was proven in COS-7 cells and that issues arose visualizing the ECFP-ATGL construct, it was decided to abstain from co-expression of fluorescently marked ATGL. Subsequently planned fluorescence experiments were set up, keeping the use of a proper filter-set in mind, assuring as little interference as possible between the used channels of all examined fluorophores and dyes.

***Co-localization Experiments* – Fluorescence microscopy**

Co-localization or protein interaction studies using fluorescently tagged proteins display a very convenient and elegant design for bioimaging experiments, especially regarding their unique ability to differentiate between the fluorescent signal and the background. They present a way of analyzing proteins with no specific antibodies available and allow in vivo fluorescence microscopy. They reduce the workflow of the microscopy experiment, as the visualization of the analyzed proteins does not have to be achieved by additional staining or antibody-reactions, nevertheless the additional work of cloning the fluorescent hybrid proteins cannot be disregarded [159–161]. After the pre-tests, the analysis of protein-protein interactions and co-localization in different states of lipolysis via fluorescence microscopy was attempted. To summarize the experiments briefly: Co-localization experiments with COS-7 cells co-expressing variations of murine CGI-58-mCherry (wild-type, S239A-, Y330F- and S239A/Y330F-mutant) and murine Plin1-EYFP wild-type were conducted. COS-7 cells were seeded and after 24 hours a lipid-based co-transfection with equal amounts of each respective plasmid DNA was conducted. 24 hours after transfection, the cells were lipid loaded with a complex of oleic acid and BSA to increase TAG production and LD formation. Half of the samples were examined under basal conditions. Lipolysis stimulation of the other half was achieved via incubation of the cells with forskolin and IBMX 36 hours after transfection. Consequently, cells were fixed, washed and nuclei and lipids were stained. Throughout this chapter, the results and possible error sources, as well as their solutions are discussed. To help maintain an overview, the discussion will follow the workflow of the experiment step by step.

Cell culture procedures were conducted following pre-approved standard protocols for COS-7 cells, which is why problems concerning general cell culture techniques can be excluded. Co-transfection was, as noted above, tested and optimized previous to the fluorescence experiments. Nevertheless, one of the first complications to note was inadequate co-transfection efficiency. Many of the factors influencing transfection efficiency, such as the health of the cells, cell number, and their confluency at the point of transfection were checked. The quality and the amount of DNA used and its ratio to the transfection reagent, even the incubation time of the mix were tested. The culture media with or without addition of serum or antibiotics was used according to the ideal settings during each step of the protocol [141]. Even though all those factors were considered, and a transfection reagent, especially developed for cells of the COS-line, was used, cells co-expressing both constructs had to be searched throughout the whole sample and were unfortunately were scarce. This led to a significant decrease in the number of cells to be examined i.e. to a low number of micrographs to be analyzed. A suitable example thereof can be seen in Figure 23ii, showing COS-7 cells that should be co-expressing mCGI-58 S239A and mPlin1 WT under stimulated conditions. However, although all three cells in the center of the picture are visibly expressing CGI-58, only the central one shows Plin1 expression,

consequently demonstrating that co-expression was not successful in all cells. Repetition of the experiments should be conducted using either other transfection reagents or another transfection method (virus-mediated stable transfection for instance) to assure higher efficiency [153].

Lipid-loading of the cells was carried out following pre-approved protocols, and the cells showed accumulation of an average amount of approximately 140 µm² of LDs in each cell, which is why this step was considered working properly [146].

Stimulation of lipolysis was conducted according to pre-approved standard procedures and as the quality of all chemicals was guaranteed and fresh solutions were prepared for each experiment, this step was not deemed problematic.

Concerning the fixation of the cells, the possible interference of formaldehyde with the fluorescence-tags as a consequence of the crosslinking of free amino groups of proteins, could pose a problem [162]. However, the detection of strong fluorescence signals was regarded as prove that the fixation method did not influence the fluorescent tags.

The staining of nuclei and lipid droplets was conducted using a variation of dyes. Hoechst33342 and DAPI were used to dye the nuclei. The used dilutions and procedures were pre-approved through tests conducted by other researchers of our group and were therefore followed rigorously. The lipid stain used in early experiments was Bodipy493/503. The main problems of this fluorescent dye noted in literature are its small stokes shift, which should not pose a problem with the used filter set, and its limited photostability, which was counteracted by using VECTASHIELD Antifade Mounting Medium [163, 164]. Nevertheless, bleaching of the dye became an obstacle throughout early observations, as the search for cells, expressing both proteins, could require the testing of all channels to assure the proper imaging of all components of the experiment. Even within the short time testing all channels, severe photobleaching could be detected. It was assumed that this problem concerned only the particular batch of Bodipy purchased, nonetheless, it was decided to try another product: Lipidtox Deep Red. Using this dye according to pre-approved protocols led to the clear visualization of LDs, which was a necessity, as the aim of this experiment was to determine localization of proteins in the cell, especially in respect to LDs. It should be mentioned that the intensity of the dye seemed to vary from well to well, suggesting a problem concerning the mixing or the dilution of the dye, or even insufficient light exclusion during the experiment, but all these factors that can easily be corrected.

Imaging depicted the last stage of the fluorescence experiments. Basics concerning the planning of fluorescence- and immunofluorescence microscopy experiments, focusing on the choice of fluorophores and the possibility of crosstalk, were already reviewed during pre-test discussions and the fluorescence and immunofluorescence experiments had been designed assuring minimum crosstalk between all channels with the generous help and expertise of Jürgen Gindlhuber. The

following discussion shall focus on bringing the obtained results into context with up to date literature, as well as reviewing possible errors, their cause and solutions.

Figure 22 and Figure 23 show representative results for all experimental set-ups conducted, varying combinations of CGI-58-mCherry with Plin1-EYFP under basal and stimulated conditions. Laser- and filter settings can be found in this chapter's "experimental procedures". Primary visual analysis of the results showed that, although Plin1-EYFP and CGI-58-mCherry produced strong fluorescence signals, if co-expressed properly, even individual experiments produced contradictory outcomes. An example thereof can be found in Figure 23i: In this micrograph, 2 co-transfected cells are visible. In the cell in the lower left corner of the micrograph, signals for CGI-58 (red) were detected in the cytoplasm as well as on the LD, whereas the other cell shows distinct localization of CGI-58 at the lipid droplet.

Putting the interpretation of these results aside for the time being, we wanted to eliminate subjectivity by merely examining the micrographs visually. Therefore, a rough analysis with ImageJ using the plugin Fiji and a makro designed by Jürgen Gindlhuber was attempted. Therein, areas in the pictures were chosen (either at the LD or in the cytosol) and the absolute intensities of both CGI-58-mCherry and Plin1-EYFP in those areas were measured and compared. It became clear that this approach led to no significant/valid results as well. Nevertheless, examples of produced micrographs are shown, and interpretation of the results will be attempted on the basis of previous research, keeping in mind that, because of the small sample size, as a consequence of the low number of co-transfected cells, in combination with the inconsistency of the results, it is impossible to make conclusive statements.

The first micrographs shown in Figure 21 display COS-7 cells expressing wild-type CGI-58-mCherry and wild-type Plin1-EYFP in varying magnifications. The micrographs show a maximum intensity z-projection, whereby all channels are merged in this picture. Blue nuclei and clearly visible green signals for the LDs can be obtained in both micrographs.

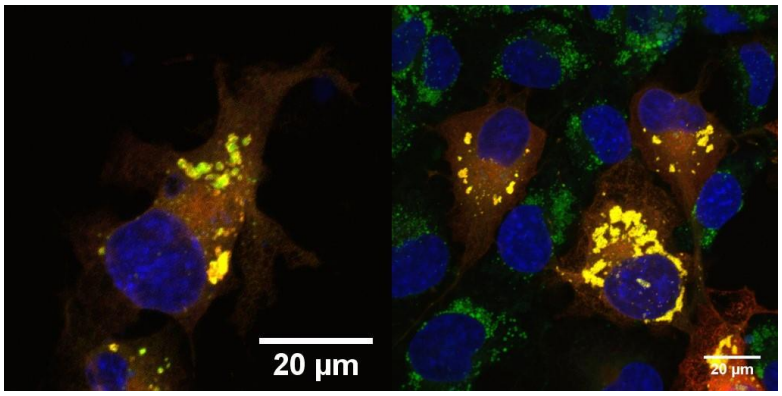

Figure 21: ***COS-7 cells expressing wild-type mCGI-58-mCherry and wild-type Plin1-EYFP under basal conditions****. Cells were fixed and stained with Hoechst 33342 for the detection of nuclei and LipidTox Deep Red for the detection of lipid droplets. Blue: Nuclei; Yellow: Plin1-EYFP; Red: CGI-58-mCherry; Green: Lipids; Scale bars: 20 µm*

The organization of Plin1 (yellow) around the lipid droplets in Figure 21 is clearly observable and would be expected, regarding the current state of research on the subject. It has been reported that Plin1 is directly recruited to the LD and stabilized, building the scaffold on the LD surface, whereas its stability is dependent on its LD-association and Plin1 is degraded, once detached from the LD [15, 94]. Studies indicate that the N-terminal hydrophobic PAT-motif and a 11-mer domain containing helical motifs, common to all Plins, as well as other non-conserved C-terminal elements are essential for the correct LD-targeting [15, 94, 165]. The involvement of amphipathic α-helices and hydrophobic hairpin structures has been stated to play a role in LD protein targeting but the exact mechanism regarding the Plins has not yet been completely clarified [15, 166]. Intriguingly, it became apparent that Plins do not only target LDs, but do also distinguish between therein contained lipids. Plin1a, 1b and Plin5 specifically target LDs storing TAG, which is why adipocytes, which primarily accumulate lipids in the form of TAGs, express high amounts of these three Plins, whereas Plin5 is only expressed in brown adipocytes. Plin1c and 4 were, however, shown to target cholesteryl ester-loaded LDs and Plin2 as well as Plin3 do not show significant preferences [167]. As multiple members of the Plin family seem to be expressed in cells that store neutral lipids [15], distinct forms of Plins seem to have varying impact on the cells' TAG storage ability. Experiments with Plin1 null mice showed that their adipose LDs were only coated with Plin2, resulting in increased TAG turnover and a 70%-reduced adipose tissue mass, due to the missing Plin1 scaffold [168, 169]. Conversely, the expression of Plin1 in cells that normally only coat their LDs with Plin2 led to enhanced TAG storage, due to decreased lipolysis [99, 100]. In humans, studies showed that expression of frameshift-mutated versions of Plin1 led to the subjects' development of lipodystrophy, characterized by ectopic lipid deposition, due to impaired TAG storage in adipocytes [125, 170]. The observed organization of Plin1 around the LDs in all examined cells expressing the construct shows that lipid loading had been successfully accomplished and that the Plin1-EYFP construct localizes to the LD, as expected.

Splitting the channels of the micrographs in Figure 21, co-localization of CGI-58 and Plin1 at the LD can be seen in both presented micrographs (not shown). Nonetheless, a faint cytosolic background signal of CGI-58 and Plin1 was detected in all samples, which can be explained by the fact that forced expression of high levels of marked proteins has been reported to lead to an overabundance of protein. This excessive amount of protein can result in impaired protein trafficking or insufficient protein degradation, which in turn influences subcellular localization and other factors compared to the wild-type proteins [159].

Figure 22 depicts representative images of all experiments in the basal state of lipolysis: All cells show at least partial co-localization of CGI-58- and Plin1 constructs at the LD. Examining various sources of results concerning the localization of the proteins of the lipolytic machinery, the following statements can be made: Granneman et al. showed colocalization of CGI-58 and Plin1 at the LD via FRET- and BiFC-

experiments in COS-7 cells [102]. Sahu et al. verified these results, reporting co-localization of CGI-58 WT as well as CGI-58 S239A with Plin1 at the LD under basal conditions [79]. This study additionally stated that the Ser239-residue of CGI-58 takes an important role in ATGL activation, by inducing CGI-58's release from the Plin1 scaffold after PKA-mediated phosphorylation. As an introduced mutation at Ser239 should only interfere with CGI-58's localization after stimulation of lipolysis, it would be likely that CGI-58 S239A remains co-localized with Plin1 during the basal state of lipolysis. As expected, Figure 22i and ii, show mainly co-localization of both Plin1 and CGI-58 at the LD, confirming these results. The additional cytosolic signals that can be observed in these micrographs can be explained by an extensive overexpression of the constructs and consequentially their overflow into the cytosol, as mentioned above.

Figure 22iii shows experiments co-expressing the novel mutant CGI-58 Y330F with Plin1 WT. The examination of this mutant in the context of lipolysis became of interest because of research conducted by Sanders et al. in 2015.

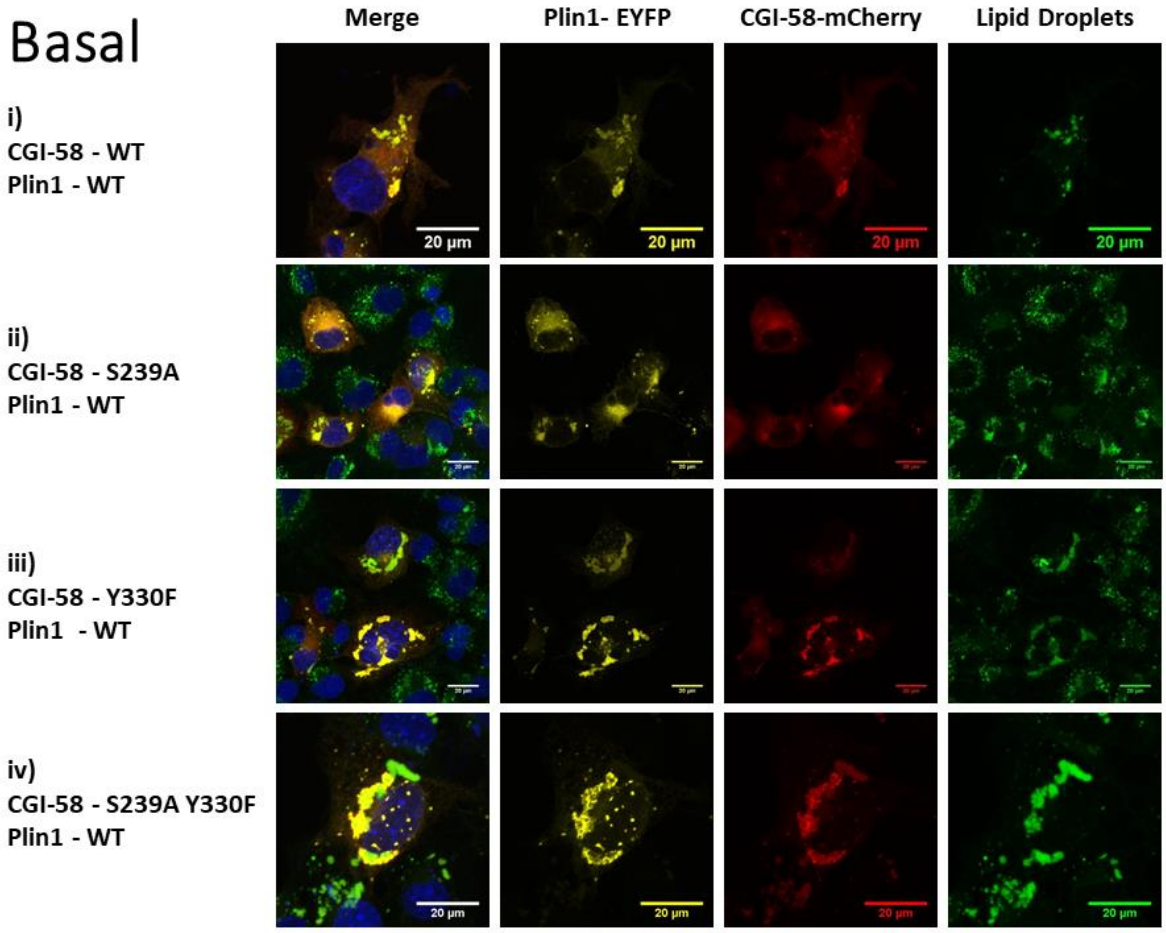

Figure 22: ***Under basal conditions Plin1 and CGI-58 in varying forms co-localize at the LD*** *Representative micrographs of COS-7 cells co-expressing either CGI-58-mCherry wild-type[i], CGI-58-mCherry S239A [ii], CGI-58-mCherry Y330F [iii], or CGI-58-mCherry S239A Y330F(iv) with Plin1-EYFP wild-type under basal conditions. Cells were fixed and stained with Hoechst 33422 for the detection of nuclei and LipidTox Deep Red for the detection of lipid droplets. Under basal conditions all CGI-58 variants co-localize with Plin1 at the LD. Scale bars: 20 µm*

Early on, PKA-mediated lipolysis stimulation was the only know mechanism regarding rapid activation of adipocyte lipolysis, but Sanders et al. showed an alternative mechanism for lipolysis activation: the binding of ligands to CGI-58, subsequently mediating CGI-58's release by Plin1 and furthermore facilitating stimulation of lipolysis by enabling binding of CGI-58 to ATGL [70]. Using an activity-based probe (NBD-HE-HP) that had previously been proven to covalently bind to CGI-58 by Birner-Gruenberger et al. [171], they showed that NBD-HE-HP binds CGI-58 at residue Tyrosine330 (Y330) [70]. Following experiments showed that novel synthetic ligands did interfere with NBD-HE-HP binding at Y330 and that the residue is part of a binding pocket for the new synthetic ligands but not crucial for their interaction with CGI-58, i.e. Y330 is not the binding point of said ligands [70]. Regarding Y330's involvement in ligand-mediated lipolysis, it was decided to look at possible alterations in subcellular localization of a CGI-58 Y330F mutant and a CGI-58 S239A Y330F double mutant. Figure 22iii and iv show that both, the Y330F- and the double mutant, localize to the LD under basal conditions, indicating that Tyr330 may genuinely have no influence on the subcellular localization of CGI-58, at least under basal conditions. Considering the role of the binding site as described in previous literature, it should be assumed that, as the mutation of Y330 to alanine or phenylalanine did reportedly not interfere with CGI-58's ability to promote lipolysis or its interactions with Plin [70], the mutation should not impact CGI-58's subcellular distribution. Even if the mutation did alter CGI-58's interaction with Plin, the released activator would co-localize with and activate ATGL, inducing lipolysis, which would re-locate the CGI-58-ATGL complex at the LD anyhow.

Figure 23 displays the same co-expression experiments as Figure 22, only this time under lipolysis stimulating conditions. The "sequestration-release"- model for CGI-58 under lipolysis stimulating conditions, which was proposed by several research groups [17, 50, 62, 79], states that the PKA-mediated phosphorylation of CGI-58 and Plin1 leads to CGI-58's release and consequently its co-activation of phosphorylated ATGL. This model is generally accepted but in 2015 an additional subcellular movement was observed: the dispersion of phosphorylated CGI-58 to the cytoplasm directly after lipolysis stimulation [79]. Since direct protein-protein interaction is necessary for maximum activation of ATGL, an interaction proven by various groups [18, 50, 52, 77], it would be reasonable to assume that ATGL and CGI-58 would have to co-localize at ATGLs "area of activity", which would be the LD [68], deeming the proposed dispersion of CGI-58 unlikely. ATGL is mainly cytosolic during the basal state; however, even in this state low levels of ATGL are associated with the LD, as low rates of basal lipolysis are detectable [15]. After lipolysis stimulation, ATGL is recruited to the LD in a Plin1-dependent manner [18, 40, 53], leading to elevated levels of lipolysis. Earlier localization studies regarding ATGL, CGI-58 and Plin1's co-localization also showed that after lipolysis stimulation ATGL-CGI-58 interactions take place on various intracellular structures lacking Plin1 as well as Plin1-containing LDs. Nonetheless, the greatest increase in ATGL-CGI-58 interactions after stimulation was

measured at Plin1-laced LDs [17]. In 2015, the internal structure of CGI-58 was examined closely and a Trp-rich sequence at the N-terminus was discovered, revealing three tryptophan residues that build a left (Trp21 and Trp25) and a right (Trp29) anchor arm, serving as a LD-anchor for CGI-58 [78]. The role of this anchor has not yet been fully understood, but it is hypothesized that it may be responsible for either the correct orientation of CGI-58 at the LD, facilitating its interaction with ATGL, or for bringing the substrate into perfect position to be highly accessible by ATGL [78]. The fact that the anchoring of CGI-58 to the LD is necessary to maximize ATGL activation [77, 78] also seems to contradict Sahu's model of cytosolic dispersion of CGI-58 under lipolysis stimulating conditions. Actually, it would endorse a model wherein CGI-58 is localized at the LD, binding ATGL and providing the conditions for maximal lipolysis activation. As this experiment was designed to be a repetition of the one in the Sahu paper, the dispersion of CGI-58 should have been replicated, even if it was just a short-time translocation, since time points were chosen identically to those in the paper.

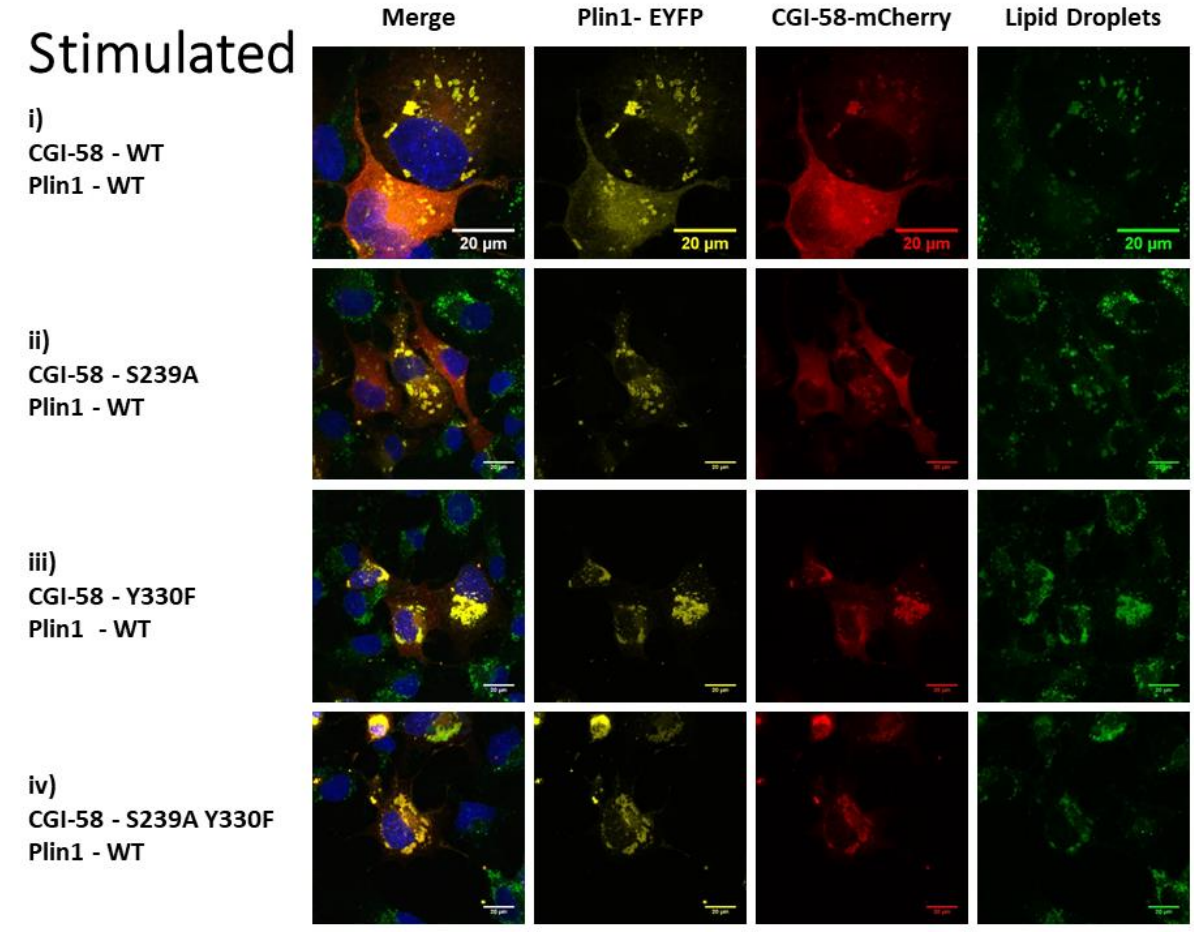

Figure 23: ***Mutation of mCGI-58 S239A may lead to reduced trans-localization of CGI-58 to cytosol after lipolysis stimulation. Results of experiments with mCGI-58 Y330F mutants remain inconclusive****. Representative micrographs of COS-7 cells co-expressing either mCGI-58-mCherry wild-type[i], mCGI-58-mCherry S239A [ii], mCGI-58-mCherry Y330F [iii], or mCGI-58-mCherry S239A Y330F(iv) with mPlin1-EYFP wild-type stimulated conditions. Lipolysis was stimulated with forskolin and IBMX. Cells were fixed and stained with Hoechst 33422 for the detection of nuclei and LipidTox Deep Red for the detection of lipid droplets. Under stimulated conditions wild-type CGI-58 partially translocated to the cytoplasm whereas all other CGI-58 constructs mainly remained at the LD. mCGI-58 S239A and mCGI-58 Y330F seem to reduce re-localization to the cytoplasm but seemingly varying expression levels of the constructs make concrete assertions difficult (see text for details). Scale bars: 20 µm*

Since most of the studied sources indicate that co-localization should be present, and my experiments did not produce significant results, a repetition of the experiment is inevitable to come to a conclusion. Examining my obtained results, Figure 23i displays 2 cells co-expressing CGI-58 WT and Plin1 WT under stimulated conditions showing contradictory localizations of CGI-58. The cell in the lower left corner shows mainly cytosolic CGI-58, whereby the other cell shows CGI-58 localization primarily and distinctly on the LD, which could be explained by varying expression levels of CGI-58 from cells to cell. Taking into consideration all aforementioned points, it would be reasonable to assume that the correct localization of the 2 constructs would be at the LD, as previously repeatedly stated [68]. The cytosolic CGI-58-dispersion could again be interpreted as a side-effect caused by a substantial overexpression of the CGI-58 construct, as this had also been present in cells examined in the basal state of lipolysis.

The central cell in Figure 23ii shows co-expression of CGI-58 S239A and Plin1 WT. Corresponding to Sahu et al.'s results, the phosphorylation of CGI-58 at residue S239, which is contained in a PKA consensus sequence, was shown to be responsible for the translocation of CGI-58 to the cytosol after lipolysis stimulation. Additionally, the mutation of S239 to alanine led to the persistence of CGI-58 at the LD [79]. Considering the preceding discussion, the localization of CGI-58 at the LD should be present anyhow, as the mutation of the serine residue should not interfere with the CGI-58's Trp-LD-anchors. Therefore, it would be plausible to conclude that the S239A mutant of CGI-58 would be detected at the LD, which is confirmed in the central cell, that mainly shows a co-localization of the Plin1 and the CGI-58 construct at the LD. The cells in Figure 23ii furthermore display the aforementioned issues concerning co-transfection efficiency. Plin1 is only co-expressed in one of them, which is why only the central, successfully co-transfected cell, displaying CGI-58 S239A at the LD, can be used to make any statement regarding the localization of the constructs. Basically, the absence of Plin1 expression should have no influence on CGI-58's localization, due to CGI-58's LD anchor, but to prove that further analyses of cells expressing both constructs have to be conducted.

Figure 23iii and iv show the results of CGI-58 Y330F and CGI-58 Y330F S239A co-expression with Plin1 under stimulated conditions. Both experiments show co-localization of the CGI-58 mutant and Plin1 at the LD. The binding site of Y330 had previously been examined in context with ligand-mediated lipolysis activation. As its impact on CGI-58-Plin1 interaction has already been disproven [70] and the mutation of the site should have no influence on PKA-mediated lipolysis stimulation, the present result, a co-localization of CGI-58 and Plin1 at the LD should be correct. Finally, no clear statement can be made regarding Y330's influence on cellular localization, although the limited set of micrographs and more importantly the current state of research would indicate that the residue does not have an influence on PKA-mediated lipolysis activation and localization of CGI-58 in either the basal or stimulated state of lipolysis.

An additional aspect to take into consideration is hydrolase activity. To assure proper lipolysis activation and measurement of its extent, a determination of TAG hydrolase activity and the amount of released NEFA or glycerol in the basal and stimulated state of lipolysis is imperative. A comparison of NEFA contents at set start and stop points in basal and stimulated conditions would give insight in the amount of lipolysis activation present. This was attempted using a NEFA kit (Wako Chemicals GmbH); however, the dilution was too high, and neither basic nor elevated levels of NEFA after stimulation were measurable. In further experiments, this issue has to be solved, possibly by minimizing the well-size and the used medium volume, to confirm lipolysis activation by other means than confirmation of co-localization. Additionally, it is possible, as the expression of ATGL was only shown per Western blot, that the TAG hydrolase is only expressed at low levels, leading to low hydrolase activity. Thus, the hydrolase activity should additionally be checked in COS-7 lysates before use and if insufficient, ATGL has to be expressed as a different construct.

The main issue present throughout all conducted microscopy experiments was the variation of expression levels. To guarantee correct results, expression levels of each construct in equivalent amounts to those present in adipocytes would have to be assured. The co-transfection with varying amounts of DNA and varying ratios between the constructs has to be conducted to perfect the experiment and to consequently make valid statements regarding the results. All in all, considering the divergent outcomes of these experiments as well as the small sample size, the repetition of all experiments is required.

As a final point, another element concerning these experiments must be discussed: fluorescence tags. The use of tags has several pitfalls: The manipulation of the protein could possibly lead to protein misfolding, blocking of binding sites, altered protein shuttling or even to impaired functionality, which would, in conclusion, influence the outcome of the experiment severely. Even the localization of the tag (C-terminal or N-terminal) has been shown to influence the proteins' properties [159–161]. The tagged proteins were a kind gift by Dr. Granneman and his team conducted various studies using these constructs [102, 112, 156], as a consequence, experiments were conducted assuring that the fluorescence tags have no influence on the protein interactions [157]. With the help of these constructs, Granneman et al. showed that EYFP-marked Plin1 and mCherry-marked CGI-58 highly localize at the LD, whereas ECFP-ATGL was present in the cytosol as well as at the LD. The results reproduced those of other groups, such as Subramanian et al. and Yamaguchi et al. in 2004, whereas those research teams used an immunochemical approach to show the same phenomenon regarding endogenous Plin1 and CGI-58 [62, 101]. Furthermore, the same conclusion was reached by Sahu et al. in 2015, expressing recombinant Plin1 and CGI-58 variations in COS-7 cells [79]. The overlap of all these results strongly indicates that the tags do not have a critical influence on the properties of the proteins as such.

In conclusion, the summary of previous research and my fluorescence experiments results would indicate that all examined co-expressed Plin1 and CGI-58 constructs should be co-localized at the lipid droplet in the basal as well as the stimulated state of lipolysis, keeping in mind that only preliminary results were achieved through my experiments and that an overall repetition is necessary.

Co-localization experiments – **Immunofluorescence microscopy**

Additional to fluorescence experiments, it was decided to examine the protein expression and localization via immunochemical approach, to rule out eventual changes of cellular localization due to fluorescence tags. The immunofluorescence experiment was basically designed identically to the discussed fluorescence experiment above, besides transfection with other plasmids (expressing non-fluorescent proteins) and additional steps for visualization via immune-reactions. Transfection was conducted with Plin1 wild-type and various CGI-58 variations, all contained in pCDNA HisMax C vectors, without fluorescence tags. Seeding, transfection, lipid loading, stimulation of lipolysis and fixation of the cells were conducted as mentioned above. After fixation, the cells were blocked with skim milk and then probed with a mix of antibodies specific to CGI-58 (mouse/monoclonal) and Perilipin-A (rabbit/polyclonal). After washing the cells, an incubation with a mix of the secondary antibodies was conducted. The staining of nuclei and lipid droplets (after vigorous washing) displayed the last step of the experiment before the microscopic examination of the samples. The representative results of the immunofluorescence experiments can be found in Figure 24, Figure 25 and Figure 26. Transfection, lipid loading, and stimulation were discussed in the previous chapter and the same problems/solutions mentioned before can be applied to this experiment (transfection efficiency, number of transfected cells, controversial results etc.).

The primary difference between the fluorescence and immunofluorescence reaction is the immunoreaction necessary to visualize the analytes and there are many pitfalls regarding the use of antibodies. The fact that the set-up of each experiment has to be checked thoroughly regarding the antibodies and their various properties builds the basis of each experiment. For this set-up a monoclonal antibody raised in mouse for marking CGI-58 and a polyclonal anti-Plin1 antibody raised in rabbit was chosen. Monoclonal antibodies do, as mentioned before, show few cross-reactions since they only bind to one epitope, making them more specific as opposed to polyclonal antibodies [133]. However, the masking of this single epitope could lead to the failure of the antibody reaction and conclusively to the failure of the experiment, which is why many researchers prefer polyclonal antibodies for immunofluorescence experiments. In search of the right secondary antibody, the compatibility of each host has to be checked corresponding to each analyte, the blocking reagent and of course the expression system one is working with. It was decided to use a Cy3-marked goat anti mouse IgG for visualization of CGI-58 and an AlexaFuor647 anti-rabbit antibody to visualize marked

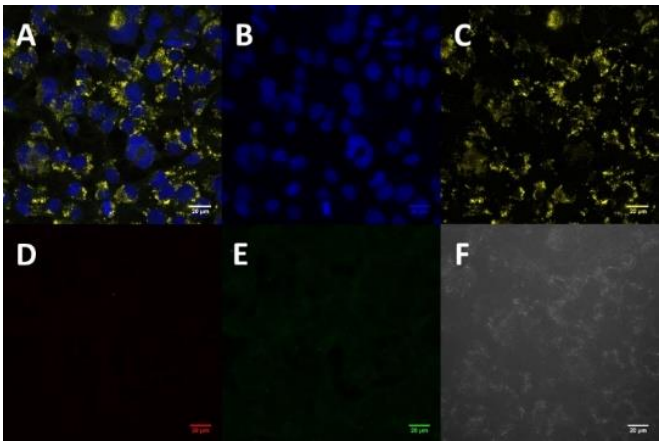

Figure 24: ***Non-transfected COS-7 control cells do not show signals when incubated with antibodies against CGI-58 and Plin1.*** *Cells were fixed, blocked and incubated with Anti-CGI-58 mouse monoclonal antibody and anti-Perilipin-A rabbit polyclonal antibody followed by anti-rabbit Alexa Fluor 647 and a Cy3-marked goat polyclonal secondary antibody to mouse IgG. Nuclei were stained with Hoechst 33422 and LipidTox Deep Red was used for the detection of lipid droplets.* ***A*** *Merged Picture;* ***B*** *Nuclei (blue);* ***C*** *Lipid droplets (yellow);* ***D*** *Anti mouse Cy3-marked goat antibody for CGI-58 detection (red);* ***E*** *Anti-rabbit Alexa Fluor 647 for Plin-A detection (green);* ***F*** *Brightfield Size bars: 20 µm.*

Plin1. The excitation and emission wavelengths of these constructs were chosen according to the available nucleic dyes (Hoechst33422) and lipid dye (Bodipy493/503) to minimize cross-talk between the channels. To assure that no antibody cross-reactions are present, the immunofluorescence experiments included a set of non-transfected COS-7 cells as negative controls. As shown in Figure 24, staining of nuclei and lipids delivered the expected results (B and C). The micrographs in Figure 24 D and E represent the channels for visualization of the CGI-58 and Plin1 antibodies. The purpose of negative controls is to exclude possible background signals linked to endogenously expressed CGI-58/Plin1, autofluorescence of the cells or unspecific reactions of the antibodies within the cells, as well as problems with fixing and blocking [172]. Additionally, the control samples are typically used to set the acquired signals as a threshold to exclude false-positive signals in subsequent experiments, which was not possible in our case, since none were present [172]. The absence of any signals in the negative control can be interpreted as follows: As previous tests regarding the expression of endogenous Plin1 and CGI-58 of COS-7 cells via Western blot remained inconclusive, it can hereby be said that at least no background signal concerning the immunofluorescence experiment is produced. Additionally, no autofluorescence or unspecific binding of any of the antibodies could be detected. As no signals were detected, antibody cross-reactions can be excluded as possible cause for background signals in further experiments. Control samples and all other samples were examined using the same gain settings, assuring comparability and eliminating the possibility that varying intensity of antibody signals (or background signals) occurs due to differing laser settings in the samples and the controls.

Figure 25 and Figure 26 show micrographs depicting combinations of COS-7 cells co-expressing versions of CGI-58 and Plin1. All micrographs predominantly show co-localization of all examined CGI-58 construct with Plin1 at the LD. These results have already been reviewed regarding various studies representing the state of research during the discussion of the fluorescence experiment results, which is why this part will mainly handle the intricacies of immunofluorescence microscopy experiments. Having said that, the first thing to be noticed in all micrographs is the high background signal throughout the cells detected in the CGI-58 channel, seemingly marking the whole cytoplasm and

showing slightly more intense signals at co-localization sites with Plin1 (more pronounced in Figure 25 than Figure 26). In search for a plausible explanation for this background, the workflow was scanned for possible error sources. The fact that the control cells did not show this background signals led to the exclusion of factors that would have impacted all samples, for instance the drying out of the cells prior to fixation, incomplete fixation, as well as the implementation of too few washing steps [172]. As stated previously, formaldehyde fixation can affect detection, since the proteins N-terminal free amino groups reacts with varying side chains, like for instance cysteine, histidine, lysine and others [173], possibly leading to reduced immunorecognition of the antigens by antibodies. This can have various explanations: reduced access of the antibody to the target, reduced immunoreactivity of the target because of the formaldehyde interactions, or the change in secondary structures due to the crosslinks [174]. Nevertheless, these factors would lead to a lower background and lower signal intensity, as opposed to the clearly visible background in our samples. Although no antigen retrieval steps were included in the protocol, it was concluded that the fixation step did have no perceptible impact on the results of the experiment since the micrographs showed decent immunofluorescence signals for both constructs.

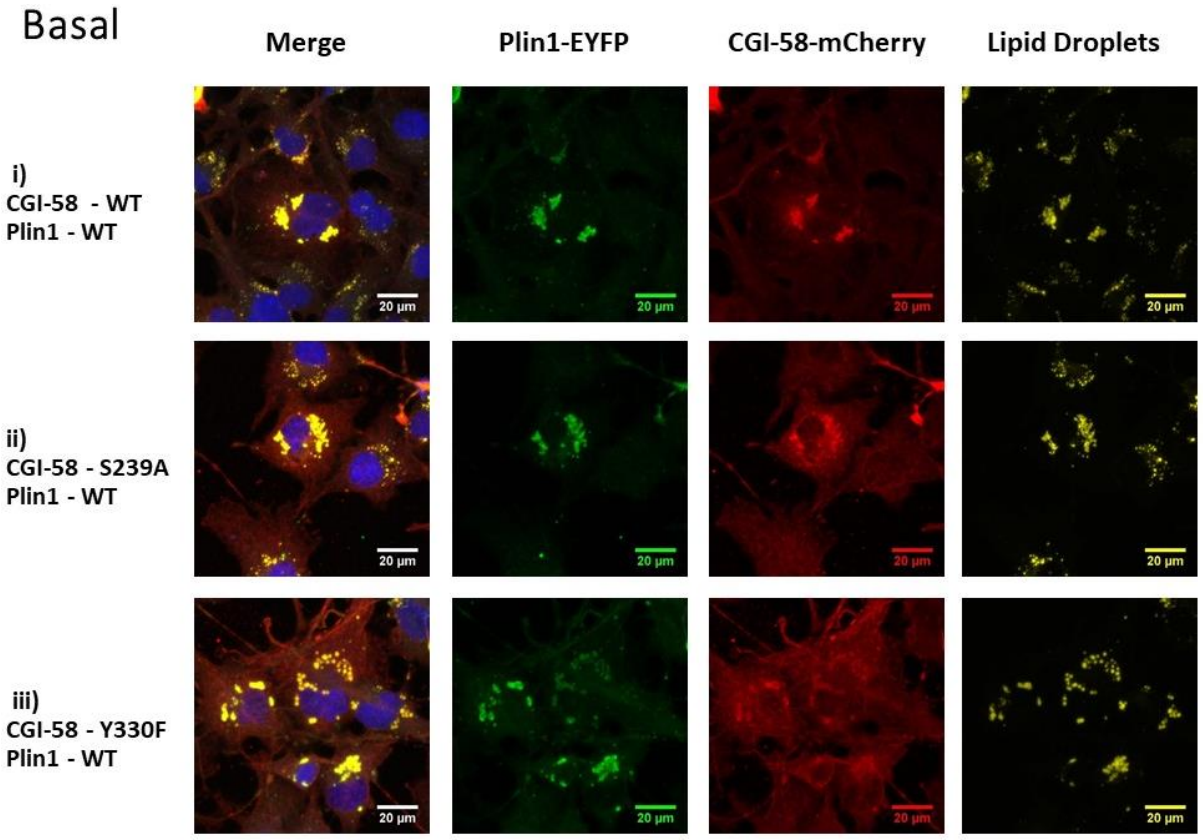

Figure 25: ***Under basal conditions Plin1 and varying CGI-58 constructs mainly co-localize at the LD in immunofluorescence experiments.*** *Representative micrographs of COS-7 cells co-expressing either CGI-58 wild-type[i], CGI-58 S239A [ii] and CGI-58 Y330F [iii] with Plin1 under basal conditions. Cells were fixed, blocked and incubated with Anti-CGI-58 mouse monoclonal antibody and anti-Perilipin-A rabbit polyclonal antibody followed by Cy3-marked goat polyclonal secondary antibody to mouse IgG and anti-rabbit Alexa Fluor 647. Then, cells were stained with Hoechst 33422 for the detection of nuclei and Bodipy 493/503 for the detection of lipid droplets. Under basal conditions, all examined CGI-58 constructs co-localize with Plin1 at the LD. Scale bars: 20 µm*

Permeabilization of cells plays a crucial role in immunofluorescence experiments, as the cell membrane is not passable for large molecules. In this experiment, permeability was assured through the use of saponin. Basically, saponin removes cholesterol from the plasma membrane, leaving it porous for small molecules to enter the cell, hitherto leaving the intracellular membranes intact because of their low cholesterol content [175]. Since the preservation of intact lipid droplets was a necessity for the experiments, saponin displayed the ideal permeabilization agent, as opposed to Triton-X or Tween-20, which are non-selective reagents that interact with both proteins and lipids [176]. On the one hand, insufficient permeabilization can lead to failing of the antibody reaction, but on the other hand it has been reported that the entrapment of unattached reagents in the cells caused by incomplete permeabilization makes them resistant to removal by wash buffer, leading to unspecific background [177]. Although other protocols contained a separate permeabilization step, the pre-approved protocol by our group included the addition of saponin to the diluent used for the preparation of the blocking solution and the antibody dilutions.

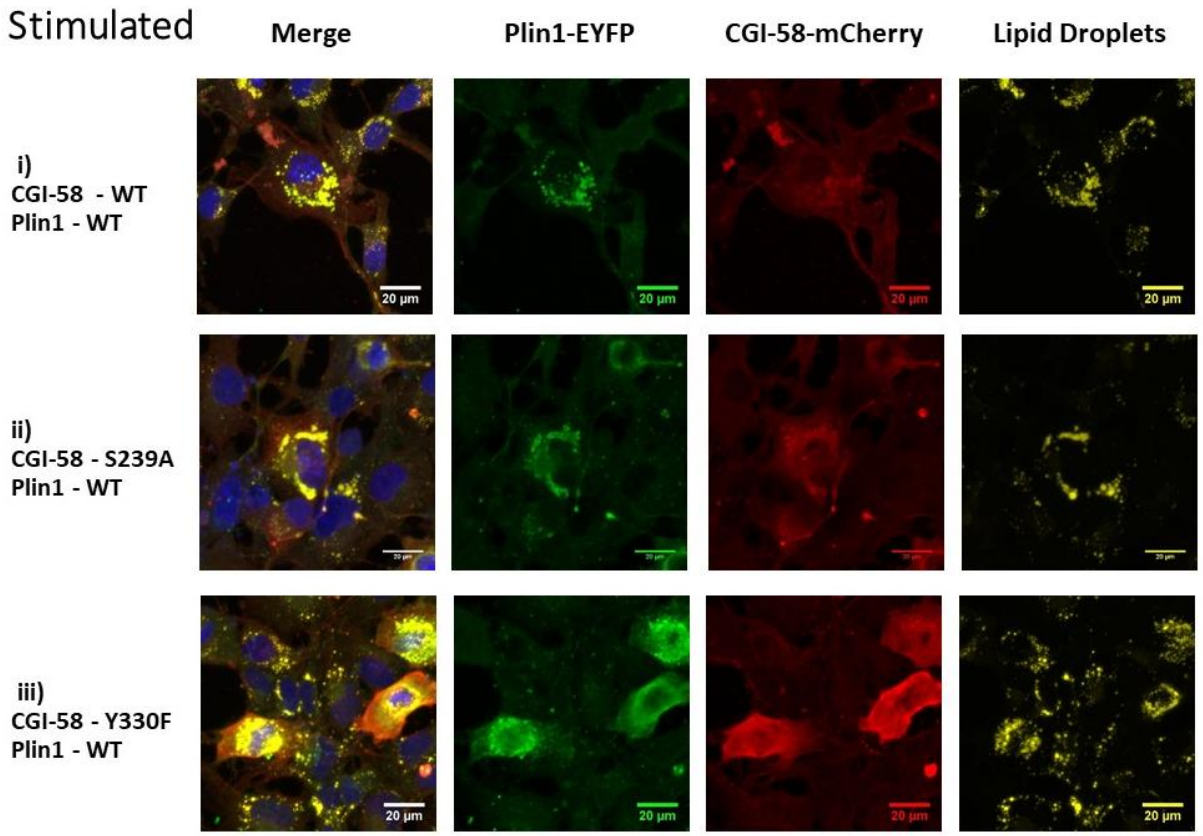

Figure 26: ***Expression of Plin1 and varying CGI-58 constructs under lipolysis stimulated conditions observed via immunofluorescence microscopy.*** *Representative micrographs of COS-7 cells co-expressing either CGI-58 wild-type[i], CGI-58 S239A [ii] and CGI-58 Y330F [iii] with Plin1 under stimulated conditions. Lipolysis was stimulated with forskolin and IBMX. Cells were fixed, blocked with skim-milk and incubated with Anti-CGI-58 mouse monoclonal antibody and anti-Perilipin-A rabbit polyclonal antibody followed by anti-rabbit Alexa Fluor 647 and a Cy3-marked goat polyclonal secondary antibody to mouse IgG. Then, cells were stained with Hoechst 33422 for the detection of nuclei and Bodipy 493/503 for the detection of lipid droplets. Plin1 is mainly located at the LD in all micrographs. Scale bars: 20 µm*

The fact that both analytes were detected in the examined samples shows that the antibodies did enter the cells, rendering the addition of saponin to the antibody diluent an adequate method of permeabilization. In the course of adapting the previously used protocol, changes were made regarding the blocking reagent, substituting the original blocking agent rat IgG with skim milk, as pre-approved protocols of the chosen antibodies stated skim milk as suitable. During this change, the new protocol did mistakenly not include saponin in the blocking solution, failing to assure that the blocking agent could properly enter the cells. Theoretically, this could lead to unspecific signals, however, as the negative control did not show any unspecific binding of the antibody to any cellular structures, it was concluded that this error did not lead to the background in our micrographs. Nonetheless, the correction of this mistake has to be implemented in further protocols. A factor that must be mentioned is the importance of keeping the compatibility of the host and the blocking agent with all of the antibodies in mind to prevent cross reactions, which in our case was ensured.

Antibody dilutions were chosen regarding references from companies and colleagues and worked properly regarding the strong signals present in the cells overexpressing the CGI-58 and Plin1 constructs. Although these pre-approved antibody dilutions did not cause any problems, it should be noted that insufficient antibody dilution could lead to background signals [177].

As mentioned above, extensive washing steps between blocking and especially between first and secondary antibody incubation display a crucial point, since this significantly reduces unspecific binding of the secondary antibody [177]. Only the CGI-58 antibody produced signals throughout the cells and the Plin1-antibody did not, which leads to the assumption that antibody or antigen-specific factors may be the cause of the signals. As every antibody reacts differently, further washing steps could be added to assure sufficient reduction of unspecific signals.

Taking the antibody-specific background and the results of the negative control into account, the most probable explanation for the background signal coming to mind is a difference in the expression levels of the constructs. As the same kind of plasmid (pCDNA HisMax C) was used to clone the constructs, simple errors, for instance discrepancies concerning the estimation of the amount of nucleic acid in the prepared plasmids or even trivial dilution or pipetting errors could be responsible. Even differences in plasmid quality could have an influence on varying levels of expression. Experiments co-transfecting cells with varying DNA amounts and ratios of the respective constructs have to be conducted to assure equivalent expression levels of the plasmids and in consequence correct results. All other issues concerning plasmids can be solved easily by producing new plasmids, assuring their quality, correct concentrations and dilutions when repeating the experiments.

To sum up, the visualization of the nuclei worked perfectly, and the lipid dye led to clearly observable lipid droplets. Plin1 organization around the droplets can be obtained producing fairly strong signals restricted to the LD only, which would be expected. The main issue that arose during this

immunofluorescence experiment was the production of unspecific background signals by the CGI-58 antibody, whereby the most likely explanation for this was pinpointed to issues with plasmid DNA expression.

In conclusion, the preliminary results of the immunofluorescence experiment did mainly reproduce the outcomes of the fluorescence experiments, as the strongest signals for the CGI-58 constructs were primarily located at the LD co-localized with Plin1.

PKA/PKG Assay – Part III

Background

This section of the thesis concerns itself with the phosphorylation of CGI-58 in particular. As mentioned in the introduction, both PKA and PKG regulate lipolysis via phosphorylation of HSL and Plin1 [35]. As previous studies showed that CGI-58 contains a PKA consensus sequence Arg^{236}-Lys-Tyr-Ser-Ser or R^{236}KYSS [32, 33, 79] and was phosphorylated by PKA, it was hypothesized that CGI-58 could possibly be a target for phosphorylation by PKG as well. To test this theory, a mutated version of murine CGI-58 was created, exchanging Arginine236 to Alanine, disrupting the contained consensus sequence to "A^{236}KYSS", since the substrate consensus amino acid sequence for PKGs appears to require more basic residues than does PKA [178]. Phosphorylation of both wild-type and R236A-mutated murine CGI-58 after incubation with either PKA or PKG was checked via liquid chromatography- mass spectrometry (LC-MS) analysis.

Experimental procedure

Expression of mCGI-58 constructs

Murine CGI-58 WT and CGI-58 R236A served as substrates for the conducted PKA/PKG assays. CGI-58 wild-type and CGI-58 R236A were overexpressed in *E. coli* by Lisa Wechselberger (group of Dr. Oberer at Karl-Franzens University) and the harvested cell pellets were kindly provided to us. Information regarding its sequence and the creation of the R236A-mutated version of CGI-58 can be found in the first chapter of this thesis.

Preparation of E. coli lysates

The provided *E. coli* cell pellets were re-suspended in buffer (40mM TrisHCl, 10mM $MgCl_2$, pH7.5) and cell lysis was performed via sonication probe. After centrifugation (7197 rcf/ 15 min/ 4°C), a protein estimation of the supernatant via Bradford assay was conducted.

Estimation of overexpressed mCGI-58 in the lysates

An estimation of the amount of overexpressed CGI-58 in the lysate for further experiments was achieved via Western blot. SDS-PAGE and immunoblotting on nitrocellulose membrane were performed using standard procedures as described in part II of the thesis.

E. coli lysates containing 5 µg of total protein and purified CGI-58 (50 ng, 25 ng, 12.5 ng) were loaded on the gel. Anti-CGI-58 mouse monoclonal antibody (Abnova, Cat. No. H00051099-M01) at a dilution of 1:1000 was used for primary antibody incubation. Anti-mouse IgG, HRP-linked Antibody (Cell Signaling, Cat. No. 7076S) was used for secondary antibody incubation at a dilution of 1:3000. Volume analysis of the finished blot was carried out to estimate the amount of overexpressed protein.

Acquisition of kinases

PKG was kindly provided by Dr. D. Bertinetti (University of Kassel) in form of the human cGMP-dependent protein kinase isoform Iβ [179]. Additional information can be found in Figure 66 in the appendix. PKA was purchased from Promega (Cat. No. V5161).

PKA/PKG assay on Ni-NTA-Spin Columns

The basic approach of the conducted PKA/PKG assay was to incubate the wild-type or the mutated version of CGI-58 with either PKA, PKG, or no kinase and determine via LC-MS analysis (after reduction, alkylation, and enzymatic digestion of the reactions with either AspN or Trypsin) whether the proteins had been phosphorylated or not. First experiments showed that direct use of the *E. coli* lysate did not lead to any results via LC-MS analysis. As it was assumed that the high dilution of the protein in the lysate was the origin of the problem, it was decided that preconcentration of the overexpressed proteins would be necessary for further experimental approaches.

The provided mCGI-58-construct contained a 6-His-tag, which is why it was decided to isolate the protein using Thermo Fisher Scientific™ HisPur™ Ni-NTA Spin Columns (Thermo Fisher Scientific, Cat. No. 88224) [180]. To facilitate the workflow, the PKA/PKG assays were performed directly on the columns. To examine PKA- and PKG-mediated phosphorylation of either wild-type or R236A-mutated CGI-58, 3 columns were loaded with wild-type CGI-58 lysate and 3 columns were loaded with CGI-58 R236A lysate. Of each of those three, one column was incubated with PKA, the second with PKG and the third was used as a control reaction without kinase addition. Each column was loaded with *E. coli* lysate containing a total protein amount of 2.5 mg. The loading and washing of the His-tagged proteins was conducted following protocol steps 1-9 of the instruction manual provided by Thermo Fisher Scientific [180]. After completing step 9, the buffers on each column were exchanged to the respective reaction buffers via 3 consecutive washing steps. For PKA-incubation and control reactions, the columns were washed with PKA buffer (40 mM TrisHCl/10 mM $MgCl_2$/pH 7.8) and the PKG-columns were washed with PKG buffer (25mM TrisHCl/10 mM $MgCl_2$/pH 7.8). After the buffer exchange, 200 µL of the respective reaction mix were added to each column and incubated at 37°C for one hour. The reaction mix composition can be found in Table 10 in the appendix. In order to assure complete substrate conversion, the amount of added kinase was calculated guaranteeing complete substrate turnover during the reaction time of one hour. After 1 hour, the columns were centrifuged at 700 x g for 2 minutes and washed with 50 mM ammoniumbicarbonate (ABC) twice. Then, 200 µl of 25 mM iodoacetamide (IAA) in 50 mM ABC were added to each reaction and the columns were heated to 37 °C for 30 minutes under light exclusion. Subsequently, the columns were centrifuged again and two washing steps with AspN digest buffer (50 mM TrisHCl, 2.5mM $ZnSO_4$, pH 8.0) were conducted. Each column was then incubated with 200 µl AspN digest buffer containing 0.25 µg of AspN (1:200 ratio AspN:Protein). The reaction mix was incubated at 37°C overnight. Next day, the peptides were

harvested by centrifugation and the digest was stopped by addition of 2 µl of 30% trifluoroacetic acid (TFA). Hereby the necessary amount of 0.3% TFA for LC-MS measurement were reached.

To assure PKA/PKG activity, positive controls with each kinase were conducted with a control peptide, kemptide [33]. 20 µg of kemptide, a peptide with the amino acid sequence Leu-Arg-Arg-Ala-Ser-Leu-G (L-R-R-A-S-L-G), were incubated with 200 µL of each reaction mix (see Table 10). The reaction was incubated for 1h at 37°C. Then 200 µl of 50 mM IAA were added and incubated at 37°C for 1 hour in the dark. After addition of 0.1 µg of AspN to each vial, the proteins were digested overnight. After that the reaction was stopped by adding 30% TFA to a final concentration of 0.3% TFA. All samples were frozen at -20°C until measurement.

LC-MS/MS analysis

The samples were analyzed by by nano-HPLC (Dionex Ultimate 3000) equipped with an Acclaim™ PepMap™ 100 enrichment column (C18, 5 µm, 100 Å, 20 x 0.1 mm) and an Acclaim PepMap RSLC nanocolumn (C18, 2 µm, 100 Å, 500 x 0.075 mm) (Thermo Fisher Scientific). Samples were concentrated on the enrichment column at a flow rate of 15 µL/min with 0.1% formic acid in water as an isocratic solvent. Separation was carried out on the nanocolumn at a flowrate of 400 nl/min at 40°C using the following gradient, where solvent A is 0.1% formic acid in water and solvent B is acetonitrile containing 0.1% formic acid: 0-5min: 2% B; 5-60 min: 5-18% B; 60-100 min: 18-95% B; 100-110 min: 95% B; 110-111 min: 95-5% B; 111-125 min: 5% B. The maXis II ETD mass spectrometer (Bruker) was operated with the captive source in positive mode with the following settings: mass range: 150 – 2200 m/z; 5 Hz; capillary 1600V, dry gas flow 3L/min with 150°C, nanoBooster 0.2 bar, precursor acquisition control Top20 (CID). 20 µl of each PKA/PKG assay spin column eluate was loaded on the LC-column. This corresponds to approximately 5 µg CGI-58, assuming that all of the CGI-58 used for the assay was retained on the Ni-columns. Approximately 150 ng (3µL) of the positive control peptide (kemptide) were used for LC-MS analysis. For preferred fragmentation of the CGI-58 peptides containing the specific PKA/PKG phosphorylation site, previously measured peptide m/z were added to a preferred mass list using a width of 0.01 m/z. A list containing all information to the peptides, their modifications and the used masses can be found in Table 11 in the appendix.

The LC-MS data were analyzed using Proteome Discoverer 2.0.0.802 (Thermo Fisher Scientific) and its plug-in feature MS Amanda [181]. The search database used was customized and contained the Uniprot database for *E. coli* strain K12 (proteome ID: UP000000625), the Uniprot fasta files for human PKA (Accession number P17612), human PKG (Accession number Q13976) and murine CGI-58 wild-type (Accession number Q9DBL9). Additionally, a fasta-file of the mCGI-58 R236A mutant was created with the "fictional" Accession number Q96666. All proteins contained in the cRAP-database were added, accounting for proteins present in the experiment by contamination [182]. Carbamidomethylation on cysteine was entered as a static modification. Oxidation on methionine and

phosphorylation on serine and threonine residues was entered as a dynamic modification. The MS1 tolerance was set o 10 ppm and a MS2 tolerance of 0.05 Da was entered. The maximum number of missed cleavages was set to 2. A maximum false discovery rate of 5% using a decoy database search was chosen as identification criteria. To specify the exact localization of the phosphorylation, a PTM (post-translational modification) analysis via phosphoRS 3.0-tool was added to the workflow.

Part III: Results and Discussion

PKA-mediated phosphorylation of CGI-58 and the examination of the PKA/PKG consensus sequence of CGI-58 and the possibility of CGI-58 being a target for PKG phosphorylation were the point of interest in this part of the thesis. As the generation of a murine CGI-58 R236A mutant was already discussed in part I of the thesis, and the over-expression of the proteins was kindly taken over by Lisa Wechselberger, the beginning of experiments in this part is represented by the estimation of the amount of CGI-58 overexpressed in the *E. coli*- pellets provided. In early stages of the experiment, it became clear that an isolation or purification of the expressed proteins would be necessary as their concentration in the lysate was too low to measure properly in diluted form. The Ni+-NTA-spin columns were the chosen method of purification and as columns can only be loaded with a certain amount of analyte, some manner of estimation of the amount of produced protein had to be attempted.

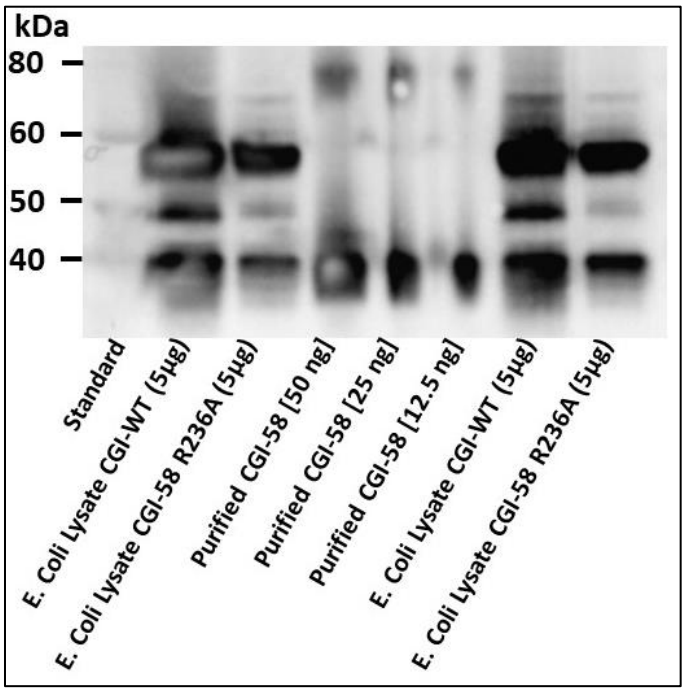

Figure 27: ***Estimation of amount of overexpressed CGI-58 in transformed E. coli cell lysates.*** *Overexpression of a CGI-58 construct was analyzed in transfected E. coli cell lysates by immunoblotting with anti-CGI-58 mouse monoclonal antibody. E. coli cells were transfected with a plasmid containing a version of mCGI-58 with TEV-cleavage site, smt3- and 6XHis-tag. Purified CGI-58 was loaded in increasing amounts to construct a calibration curve. CGI-58 size: 39.155 kDa, CGI-58 with TEV-cleavage site and smt3-tag size: 52.291 kDa, CGI-58 with TEV-cleavage site, smt3- and 6XHis-tag: 54.744 kDa*

The amount of overexpressed CGI-58 in each cell pellet was estimated via volume analysis of Western blots (Figure 27) as follows. Increasing amounts of purified CGI-58 (12.5 ng, 25 ng and 50 ng) were used as standards in lanes 4, 5 and 6, showing signals at ~40 kDa and ~80 kDa. As murine CGI-58 has a mass of 39.155 kDa [61], it was concluded that the 80 kDa signal is a result of dimer formation. The volumes of the purified CGI-58 bands were used to create a calibration curve, plotting volume versus concentration. The calibration curve was used to calculate approximate CGI-58 amounts through measurement of CGI-58 band volumes in the respective *E. coli*-lysate lanes (lanes 2, 3, 7 and 8). All of these lanes show 3 prominent bands on the blot at ~40 kDa, ~50 kDa and ~56 kDa. This phenomenon can easily be explained by the sequence of the expressed protein. CGI-58 was expressed with a smt3-, a 6xHis-Tag and a TEV-restriction site, the loss of either one or all of those structures can occur throughout sample preparation for the SDS-gel. The amino acid sequence "MSDSEVNQEAKPEVKPEVKPETHINLKVSDG-SSEIFFKIKKTTPLRRLMEAFAKRQGKEMDSLRFLYDGIRIQADQTPEDLDMEDNDIIEAHREQIGQSEFELENLYFQG AMGS" (see Figure 30) representing the smt3-tag and the TEV-cleavage site was used to calculate the

molecular weight of 13.136 kDa using the ExPASy ProtParam Tool. Peptide "MGSSHHHHHHSSGLVPRGSHMASMSDSEVNQEAKPEVKPEVKPETHINLKVSDGSSEIFFKIKKTTPLRRLMEAF AKRQGKEMDSLRFLYDGIRIQADQTPEDLDMEDNDIIEAHREQIGQSEFELENLYFQGAMGS" contains the sequence of the 6XHis-tag, the smt3- tag and the TEV-cleavage site up to the actual CGI-58 sequence. Its molecular weight of 15.589 kDa was calculated using the same tools. In conclusion, the 3 signals correspond to CGI-58 at 39.155 kDa, CGI-58 with TEV-cleavage site and smt3-tag at 52.291 kDa and the complete CGI-58 construct at 54.744 kDa. After measuring the volume of all three bands and their addition, the amount of overexpressed CGI-58 could be roughly estimated. The pellet of a 200 mL *E. coli* culture contained approximately 250-300 µg CGI-58, which corresponds to approximately 1.5-3% of total protein amount estimated in samples (varying from lysate to lysate). This was deemed sufficiently accurate, as just a rough estimation was necessary.

In these early stages of the experiment, it became clear that visualization of the overexpression of CGI-58 in *E. coli* via Western blot was possible but for the PKA/PKG assay the isolation and concentration of the protein was imperative. As the expressed proteins contained a 6xHis-tag, purification via immobilized metal affinity chromatography was considered. It was decided to perform the whole assay on Thermo Fisher Scientific™ HisPur™ Ni-NTA Spin Columns (Thermo Fisher Scientific, Cat. No. 88224), taking into account that the last step of the assay was an enzymatic digest with AspN for LC-MS/MS analysis, which would in the end digest the protein "off the column". The expressed CGI-58 construct contains a total of 26 predicted cleaving sites for AspN (determined using the ExPASy Peptide Cutter tool), whereas 9 of those lie in the attached tag-sequences, which means after digest the resulting peptides are no longer bound to the column and could be easily eluated.

As the binding capacity of the columns was noted at ≤ 60mg of a 28kDa 6xHis-tagged protein from a bacterial source per milliliter of settled resin, the chosen columns can be loaded with the maximum amount of 12 mg of protein. With the previously conducted estimation of the CGI-58 amount via Western blot, it was decided to load a total of 50 µg of CGI-58, a total protein amount of ~2.5 mg, on the column.

After performing first assays on the columns and analyzing the trypsin and AspN digests via LC-MS/MS (maXis and orbitrap), it became apparent that a trypsin digests did not deliver peptides that contained CGI-58's consensus sequence around R236. Hence, in consecutive experiments only an AspN digest of the assay reactions was performed and the resulting samples were analyzed via LC-MS/MS (maXis) following protocol (see experimental procedures). The three wild-type CGI-58-lysates were assigned sample names according to which kinase they were incubate with: CGI-58 WT No PKA, CGI-58 WT PKA and CGI-58 WT PKG. The same principle applies to the R236A-mutated CGI-58 lysate (CGI-58 R236A No PKA, - PKA and - PKG) and the control peptide (kemptide) samples (Ctrl No PKA, Ctrl PKA and Ctrl PKG).

Data analysis via MS Amanda searches was conducted with all samples. Table 5 shows the total number of proteins found in each sample and especially the detected CGI-58 peptides with sequences, contained modifications, number of peptide spectrum matches (PSMs), number of missed cleavages and their MS Amanda score. MS Amanda was used for the searches as it is a database search engine, which was developed specially for high resolution tandem MS data and it outperformed MASCOT and SEQUEST regarding the number of identified PSMs for high-resolution data sets, also phosphorylated peptide library subsets in studies conducted by Dorfer et al in 2014 [181].

The first thing that catches the eye regarding the list of identified peptides of all examined samples, is that, since the goal of the experiment was to examine the phosphorylation status of CGI-58, no desired phosphorylations were found (see Table 5 in the column modifications). All lysate samples produced approximately the same results, varying mostly by the number of found proteins in total.

*Table 5: **CGI-58 peptides identified by MS.** CGI-58 wild-type or R236A overexpressed in E. coli was concentrated on HisPur™ Ni-NTA Spin Columns and incubated with either with PKA, PKG or no kinase (No PKA) in vitro, digested by AspN, and analyzed via LC-MS/MS. Peptides were identified by searching a custom made database (see chapter "experimental procedures" for details) with Proteome Discoverer and its plug-in MS Amanda. The total number of total proteins, the sequence of identified peptides, their modifications, the number of PSMs and missed cleavages and their MS Amanda score are listed.*

Sample Name	Total Number of Proteins found	Sequence	Modifications	# PSMs	# Missed Cleavages	Amanda Score MS Amanda
CGI-58 WT No PKA	989	DIPVSVIFGARSCI	1×Carbamidomethyl [C13]	3	0	238.73
		DLSTDRPVYAF	-	5	1	174.41
CGI-58 WT PKA	1079	DIPVSVIFGARSCI	1×Carbamidomethyl [C13]	3	0	229.82
		DLSTDRPVYAF	-	5	1	190.75
CGI-58 WT PKG	1275	DLSTDRPVYAF	-	5	1	240.05
		DIPVSVIFGARSCI	1×Carbamidomethyl [C13]	3	0	203.95
		KAMAAEEEVDSA	-	1	1	142.58
CGI-58 R236A No PKA	1462	DIPVSVIFGARSCI	1×Carbamidomethyl [C13]	3	0	237.09
		DLSTDRPVYAF	-	4	1	188.85
		DFKAKYSSMFE	-	1	0	137.61
CGI-58 R236A PKA	659	DIPVSVIFGARSCI	1×Carbamidomethyl [C13]	1	0	237.47
		DLSTDRPVYAF	-	3	1	164.04
CGI-58 R236A PKG	994	DIPVSVIFGARSCI	1×Carbamidomethyl [C13]	3	0	210.88
		DLSTDRPVYAF	-	3	1	183.24
		KAMAAEEEVDSA	-	1	1	133.06

There were several issues with the experiment leading to these unsatisfactory results, which will be discussed using one of the examined constructs as an example: the wild-type lysate with no added kinase (CGI-58 WT No PKA). 989 proteins were identified in this sample, which is quite a high number, considering that a purification and isolation of the overexpressed protein should have taken place before the assay and the measurement. Ranked by Amada Score, CGI-58 showed up in the higher ranks (results not shown); the high score concluding that the protein is present and correctly identified. However, the only two peptides of CGI-58 identified were, "DIPVSVIFGARSCI" and "DLSTDRPVYAF", with 3 and 5 PSMs respectively. The desired peptide "DFKRKYSSMFE" containing the phosphorylation site was not found, so no results regarding the phosphorylation state of CGI-58 on this particular site can be made. Looking at the search results, it became clear that the purification via metal affinity chromatography did not lead to proper results. Taking into account that *E. coli*-lysates display complex samples and the workflow up until the measurement of the reaction product contains many steps, it was subsequently attempted to identify as many error sources as possible.

The low number of CGI-58 peptides and PSMs obtained through our analysis, leads to the assumption that CGI-58 was not concentrated high enough to be measured properly. The first explanation coming to mind is low expression levels of the protein. CGI-58 expression had been checked via Western blot and the CGI-58 content should have been high enough to be measured with MS after purification via chromatography; however, degrees of overexpression can vary from batch to batch and therefore the possibly low expression levels of the protein could have led to the obtained results.

As low analyte concentrations in the final examined eluate could be explained by early elution of the proteins, possible error sources regarding this were considered. Buffer properties represent an important factor regarding Ni-columns, and it is emphasized that the use of dithiothreitol (DTT) has to be avoided since DTT reduces Ni-ions in the resin. The assay buffer contained small amounts of DTT, but as the concentration was kept low, and the columns did not change color to a reddish-brown, a reaction reported when DTT was present, the DTT content may not have influenced the result that heavily [183]. However, it could also be responsible for a low concentration of retained CGI-58 and could therefore explain the low number of peptides identified. Nonetheless, it has to be assumed that a reduced Ni-column should have led to the early elution of all bound proteins, therefore the high number of total proteins identified, seems to exclude this factor as the possible culprit. A further critical step in the workflow regarding the early elution is the elevated temperature during the assay, as there is a buffer exchange step after completion of the PKA/PKG assay and before the AspN-digest. However, as mentioned earlier, the presence of such a high number of proteins after the digest suggests differently.

The high total number of proteins found in our results, varying from ~660 to ~1270 throughout our samples, presented another problem. Aside from proteins containing a 6xHis-tag, it is possible that

other His-rich proteins also bind to the column, and the presence of such proteins in the complex mixture of the *E. coli* lysate is likely. The retention of those proteins could lead to "contamination" of the eluate after the assay reaction, in consequence leading to the high number of identified proteins. In regard to the retention of analytes on the columns, it is additionally suggested, that a low imidazole content of the loading buffer (equilibration buffer in my protocol) should lead to less binding of untagged proteins but as the prepared buffer already contained imidazole, this factor had been implemented in the workflow. The alteration of washing conditions, by changing the wash buffer properties or increasing of the number of washing steps, should be mentioned as a possibility to improve the purification results as well [183].

All in all, the binding of contaminating proteins, non-sufficient washing and a low level of over-expression of the protein seem to be the most probable explanations for the obtained results.

Analysis of the data obtained from the control peptide reactions via LC-MS, showed that the small control peptide, kemptide, was too polar to be analyzed via LC-MS. Only small signals were detected in the flow-through, so it was assumed that the peptide did not even bind to the pre-column and therefore was never retained in any way. If the experiment is repeated, analysis of PKA/PKG-treated and untreated kemptide with other methods, for example MALDI-TOF, may be preferred to LC/MS analysis. MALDI-TOF methods analyzing phosphorylated peptides have been studied thoroughly and various protocols have been developed characterizing phosphorylated proteins [28, 184].

It should additionally be mentioned that some of the blanks measured between the samples showed significant amounts of *E. coli* proteins present, which could be interpreted as carry over and would suggest overloading of the LC-column.

To sum up, it can be said that the attempted experimental setup would display an elegant way to purify and examine the protein in one step. Nevertheless, the expression level of the protein most likely was the limiting factor regarding this special experiment. In future attempts, every fraction (loading step, washing steps, etc.) should be examined via MS, assuring the proper retention of the desired analyte. As the concentration of CGI-58 was not high enough to lead to desired results, the assays have to be repeated but the isolation and concentration of CGI-58 should be performed before the actual assay, for instance via Ni-NTA chromatography in combination with another purification technique such as gel filtration or ion exchange chromatography.

Conclusions and Outlook

In this thesis, an attempt has been made to shed light on parts of the complex lipolytic apparatus. It especially concerned itself with the study of two proteins, CGI-58 and G0S2, regulating the activity of ATGL, the predominant TAG lipase in adipocytes, which catalyzes the first and rate-limiting step in lipolysis. The production of plasmids containing the wild-type and mutated versions of these proteins was achieved in early experiments using site-directed mutation. Subcellular localization of various proteins and mutated versions thereof was analyzed using state of the art approaches like fluorescence microscopy and immunofluorescence microscopy. Lastly, as the phosphorylation state of these proteins has been speculated to influence the level of lipolysis, phosphorylation of some of these proteins by various kinases and its detection via LC-MS/MS experiments was attempted. Although the conducted experiments led only to preliminary results, challenges and possible sources of error were thoroughly assessed with regard to the current state of the art. The repetition of the analyses will be necessary and improvements regarding the experiments have been thoroughly noted and discussed.

This final chapter should give a short outlook on how to carry on further studies after repetition of this thesis' main experiments, the fluorescence- and immunofluorescence microscopy analyses. The first proposition would be to change the expression system itself. COS-7 cells can be used for primary research into the subject but even after examination of COS-7 cells regarding their expression of endogenous protein, the additional overexpression of ATGL in the system, a monitoring of the TAG hydrolase activity and the released NEFA or glycerol contents, in the end, the cells differ from adipocytes, the actual system that is to be examined. One approach would be to try visualizing the proteins in differentiated 3T3-L1 cells, which display a widely used model for adipocytes [185]. The implementation of working silencing of endogenous CGI-58, G0S2 and even Plins, depending on the desired outcome would have to be managed first, but this cell model would probably give more accurate results in further experiments. After examination of the behavior of the S239A-, Y330F- and double mutated S239A Y330F versions of CGI-58, additional studies could be done using a S239D variation in a phosphomimetics study, depending on the outcome of the previous studies. Additionally, the mutated versions of Plin1 and Plin5 should be examined, investigating the impact of those mutations on lipolysis control. As the inhibitor G0S2 was not included in this thesis' main experiments, analysis concerning its localization as well as its phosphorylation state during basal or stimulated lipolysis would be intriguing.

In recent years, many additional binding partners to the up-to-date known players in the complex game of lipolysis have been revealed. Optic atrophy 1 (OPA1), an A-kinase anchoring protein, was shown to be bound to Plin1 and to be responsible for the recruitment of PKA (type 1 and 2) to the LD [186]. Fatty acid binding proteins (FABPs) have been shown to interact with CGI-58, suggesting these interactions

may assist in shuttling FFA and acylglycerol away from the LD [187]. Coat Protein Complex I (COPI) seems to regulate localization of Plins at the LD furthermore having an influence on ATGL levels at the LD surface [188]. Additionally, experiments using specific ATGL and HSL inhibitors, Atglstatin and BAY, have led to the assumption that HSL plays a major role in TAG-hydrolysis following PKA activation, although ATGL has been thought to be the primary and major TAG hydrolase [189]. Thus, many research questions regarding lipolysis are still not sufficiently answered and need to be explored in further years.

References

1. World Health Organization (2018) 10 facts on obesity. http://www.who.int/features/factfiles/obesity/en/. Accessed 16 Aug 2018
2. Demine S, Tejerina S, Bihin B et al. (2018) Mild mitochondrial uncoupling induces HSL/ATGL-independent lipolysis relying on a form of autophagy in 3T3-L1 adipocytes. J Cell Physiol 233(2): 1247–1265. doi: 10.1002/jcp.25994
3. Church T (2011) Exercise in obesity, metabolic syndrome, and diabetes. Prog Cardiovasc Dis 53(6): 412–418. doi: 10.1016/j.pcad.2011.03.013
4. Herrera BM, Keildson S, Lindgren CM (2011) Genetics and epigenetics of obesity. Maturitas 69(1): 41–49. doi: 10.1016/j.maturitas.2011.02.018
5. Guh DP, Zhang W, Bansback N et al. (2009) The incidence of co-morbidities related to obesity and overweight: a systematic review and meta-analysis. BMC Public Health 9: 88. doi: 10.1186/1471-2458-9-88
6. Zechner R, Madeo F, Kratky D (2017) Cytosolic lipolysis and lipophagy: two sides of the same coin. Nat Rev Mol Cell Biol 18(11): 671–684. doi: 10.1038/nrm.2017.76
7. Voet D (2008) Principles of biochemistry: [internat. student version], 3. ed. Wiley, Hoboken, NJ
8. Caroline Burgess Clifford (2018) Terminology for Vegetable Oils and Animal Fats. https://www.e-education.psu.edu/egee439/node/683
9. Wang S, Soni KG, Semache M et al. (2008) Lipolysis and the integrated physiology of lipid energy metabolism. Mol Genet Metab 95(3): 117–126. doi: 10.1016/j.ymgme.2008.06.012
10. Zimmermann R, Strauss JG, Haemmerle G et al. (2004) Fat mobilization in adipose tissue is promoted by adipose triglyceride lipase. Science 306(5700): 1383–1386. doi: 10.1126/science.1100747
11. Zechner R, Zimmermann R, Eichmann TO et al. (2012) FAT SIGNALS--lipases and lipolysis in lipid metabolism and signaling. Cell Metab 15(3): 279–291. doi: 10.1016/j.cmet.2011.12.018
12. Cerk IK, Wechselberger L, Oberer M (2018) Adipose Triglyceride Lipase Regulation: An Overview. Curr Protein Pept Sci 19(2): 221–233. doi: 10.2174/1389203718666170918160110
13. Haemmerle G, Lass A, Zimmermann R et al. (2006) Defective lipolysis and altered energy metabolism in mice lacking adipose triglyceride lipase. Science 312(5774): 734–737. doi: 10.1126/science.1123965
14. Walther TC, Farese RV (2012) Lipid droplets and cellular lipid metabolism. Annu Rev Biochem 81: 687–714. doi: 10.1146/annurev-biochem-061009-102430
15. Sztalryd C, Brasaemle DL (2017) The perilipin family of lipid droplet proteins: Gatekeepers of intracellular lipolysis. Biochim Biophys Acta 1862(10 Pt B): 1221–1232. doi: 10.1016/j.bbalip.2017.07.009
16. Schittmayer M, Birner-Gruenberger R (2009) Functional proteomics in lipid research: lipases, lipid droplets and lipoproteins. J Proteomics 72(6): 1006–1018. doi: 10.1016/j.jprot.2009.05.006
17. Granneman JG, Moore H-PH, Krishnamoorthy R et al. (2009) Perilipin controls lipolysis by regulating the interactions of AB-hydrolase containing 5 (Abhd5) and adipose triglyceride lipase (Atgl). J Biol Chem 284(50): 34538–34544. doi: 10.1074/jbc.M109.068478
18. Yang X, Lu X, Lombès M et al. (2010) The G(0)/G(1) switch gene 2 regulates adipose lipolysis through association with adipose triglyceride lipase. Cell Metab 11(3): 194–205. doi: 10.1016/j.cmet.2010.02.003
19. Brasaemle DL, Subramanian V, Garcia A et al. (2009) Perilipin A and the control of triacylglycerol metabolism. Mol Cell Biochem 326(1-2): 15–21. doi: 10.1007/s11010-008-9998-8
20. Holm C (2003) Molecular mechanisms regulating hormone-sensitive lipase and lipolysis. Biochm. Soc. Trans. 31(6): 1120–1124. doi: 10.1042/bst0311120

21. Humphrey SJ, Yang G, Yang P et al. (2013) Dynamic adipocyte phosphoproteome reveals that Akt directly regulates mTORC2. Cell Metab 17(6): 1009–1020. doi: 10.1016/j.cmet.2013.04.010
22. Zechner R, Kienesberger PC, Haemmerle G et al. (2009) Adipose triglyceride lipase and the lipolytic catabolism of cellular fat stores. J Lipid Res 50(1): 3–21. doi: 10.1194/jlr.R800031-JLR200
23. DiPilato LM, Ahmad F, Harms M et al. (2015) The Role of PDE3B Phosphorylation in the Inhibition of Lipolysis by Insulin. Mol Cell Biol 35(16): 2752–2760. doi: 10.1128/MCB.00422-15
24. Choi SM, Tucker DF, Gross DN et al. (2010) Insulin regulates adipocyte lipolysis via an Akt-independent signaling pathway. Mol Cell Biol 30(21): 5009–5020. doi: 10.1128/MCB.00797-10
25. Koren S, DiPilato LM, Emmett MJ et al. (2015) The role of mouse Akt2 in insulin-dependent suppression of adipocyte lipolysis in vivo. Diabetologia 58(5): 1063–1070. doi: 10.1007/s00125-015-3532-9
26. Kitamura T, Kitamura Y, Kuroda S et al. (1999) Insulin-Induced Phosphorylation and Activation of Cyclic Nucleotide Phosphodiesterase 3B by the Serine-Threonine Kinase Akt. Mol. Cell. Biol. 19(9): 6286–6296. doi: 10.1128/MCB.19.9.6286
27. Morandell S, Stasyk T, Grosstessner-Hain K et al. (2006) Phosphoproteomics strategies for the functional analysis of signal transduction. Proteomics 6(14): 4047–4056. doi: 10.1002/pmic.200600058
28. Jagannadham MV, Nagaraj R (2008) Detecting the Site of Phosphorylation in Phosphopeptides without Loss of Phosphate Group Using MALDI TOF Mass Spectrometry. Anal ChemInsights 3: ACI.S497. doi: 10.4137/ACI.S497
29. Huttlin EL, Jedrychowski MP, Elias JE et al. (2010) A tissue-specific atlas of mouse protein phosphorylation and expression. Cell 143(7): 1174–1189. doi: 10.1016/j.cell.2010.12.001
30. Kosako H, Nagano K (2011) Quantitative phosphoproteomics strategies for understanding protein kinase-mediated signal transduction pathways. Expert Rev Proteomics 8(1): 81–94. doi: 10.1586/epr.10.104
31. Ubersax JA, Ferrell JE (2007) Mechanisms of specificity in protein phosphorylation. Nat Rev Mol Cell Biol 8(7): 530–541. doi: 10.1038/nrm2203
32. Turnham RE, Scott JD (2016) Protein kinase A catalytic subunit isoform PRKACA; History, function and physiology. Gene 577(2): 101–108. doi: 10.1016/j.gene.2015.11.052
33. Kemp BE, Pearson RB (1990) Protein kinase recognition sequence motifs. Trends in Biochemical Sciences 15(9): 342–346. doi: 10.1016/0968-0004(90)90073-K
34. Lafontan M, Moro C, Berlan M et al. (2008) Control of lipolysis by natriuretic peptides and cyclic GMP. Trends Endocrinol Metab 19(4): 130–137. doi: 10.1016/j.tem.2007.11.006
35. Sengenes C, Bouloumie A, Hauner H et al. (2003) Involvement of a cGMP-dependent pathway in the natriuretic peptide-mediated hormone-sensitive lipase phosphorylation in human adipocytes. J Biol Chem 278(49): 48617–48626. doi: 10.1074/jbc.M303713200
36. Alverdi V, Mazon H, Versluis C et al. (2008) cGMP-binding prepares PKG for substrate binding by disclosing the C-terminal domain. J Mol Biol 375(5): 1380–1393. doi: 10.1016/j.jmb.2007.11.053
37. Villena JA, Roy S, Sarkadi-Nagy E et al. (2004) Desnutrin, an adipocyte gene encoding a novel patatin domain-containing protein, is induced by fasting and glucocorticoids: ectopic expression of desnutrin increases triglyceride hydrolysis. J Biol Chem 279(45): 47066–47075. doi: 10.1074/jbc.M403855200
38. Jenkins CM, Mancuso DJ, Yan W et al. (2004) Identification, cloning, expression, and purification of three novel human calcium-independent phospholipase A2 family members possessing triacylglycerol lipase and acylglycerol transacylase activities. J Biol Chem 279(47): 48968–48975. doi: 10.1074/jbc.M407841200

39. Cerk IK, Salzburger B, Boeszoermenyi A et al. (2014) A peptide derived from G0/G1 switch gene 2 acts as noncompetitive inhibitor of adipose triglyceride lipase. J Biol Chem 289(47): 32559–32570. doi: 10.1074/jbc.M114.602599
40. Schweiger M, Lass A, Zimmermann R et al. (2009) Neutral lipid storage disease: genetic disorders caused by mutations in adipose triglyceride lipase/PNPLA2 or CGI-58/ABHD5. Am J Physiol Endocrinol Metab 297(2): E289-96. doi: 10.1152/ajpendo.00099.2009
41. Hoy AJ, Bruce CR, Turpin SM et al. (2011) Adipose triglyceride lipase-null mice are resistant to high-fat diet-induced insulin resistance despite reduced energy expenditure and ectopic lipid accumulation. Endocrinology 152(1): 48–58. doi: 10.1210/en.2010-0661
42. Kienesberger PC, Lee D, Pulinilkunnil T et al. (2009) Adipose triglyceride lipase deficiency causes tissue-specific changes in insulin signaling. J Biol Chem 284(44): 30218–30229. doi: 10.1074/jbc.M109.047787
43. Das SK, Eder S, Schauer S et al. (2011) Adipose triglyceride lipase contributes to cancer-associated cachexia. Science 333(6039): 233–238. doi: 10.1126/science.1198973
44. Zagani R, El-Assaad W, Gamache I et al. (2015) Inhibition of adipose triglyceride lipase (ATGL) by the putative tumor suppressor G0S2 or a small molecule inhibitor attenuates the growth of cancer cells. Oncotarget 6(29): 28282–28295. doi: 10.18632/oncotarget.5061
45. Tomin T, Fritz K, Gindlhuber J et al. (2018) Deletion of Adipose Triglyceride Lipase Links Triacylglycerol Accumulation to a More-Aggressive Phenotype in A549 Lung Carcinoma Cells. J Proteome Res 17(4): 1415–1425. doi: 10.1021/acs.jproteome.7b00782
46. Al-Zoughbi W, Pichler M, Gorkiewicz G et al. (2016) Loss of adipose triglyceride lipase is associated with human cancer and induces mouse pulmonary neoplasia. Oncotarget 7(23): 33832–33840. doi: 10.18632/oncotarget.9418
47. Pagnon J, Matzaris M, Stark R et al. (2012) Identification and functional characterization of protein kinase A phosphorylation sites in the major lipolytic protein, adipose triglyceride lipase. Endocrinology 153(9): 4278–4289. doi: 10.1210/en.2012-1127
48. Rydel TJ, Williams JM, Krieger E et al. (2003) The crystal structure, mutagenesis, and activity studies reveal that patatin is a lipid acyl hydrolase with a Ser-Asp catalytic dyad. Biochemistry 42(22): 6696–6708. doi: 10.1021/bi027156r
49. Duncan RE, Wang Y, Ahmadian M et al. (2010) Characterization of desnutrin functional domains: critical residues for triacylglycerol hydrolysis in cultured cells. J Lipid Res 51(2): 309–317. doi: 10.1194/jlr.M000729
50. Lass A, Zimmermann R, Haemmerle G et al. (2006) Adipose triglyceride lipase-mediated lipolysis of cellular fat stores is activated by CGI-58 and defective in Chanarin-Dorfman Syndrome. Cell Metab 3(5): 309–319. doi: 10.1016/j.cmet.2006.03.005
51. Cornaciu I, Boeszoermenyi A, Lindermuth H et al. (2011) The minimal domain of adipose triglyceride lipase (ATGL) ranges until leucine 254 and can be activated and inhibited by CGI-58 and G0S2, respectively. PLoS ONE 6(10): e26349. doi: 10.1371/journal.pone.0026349
52. Schweiger M, Schoiswohl G, Lass A et al. (2008) The C-terminal region of human adipose triglyceride lipase affects enzyme activity and lipid droplet binding. J Biol Chem 283(25): 17211–17220. doi: 10.1074/jbc.M710566200
53. Yang X, Heckmann BL, Zhang X et al. (2013) Distinct mechanisms regulate ATGL-mediated adipocyte lipolysis by lipid droplet coat proteins. Mol Endocrinol 27(1): 116–126. doi: 10.1210/me.2012-1178
54. Kobayashi K, Inoguchi T, Maeda Y et al. (2008) The lack of the C-terminal domain of adipose triglyceride lipase causes neutral lipid storage disease through impaired interactions with lipid droplets. J Clin Endocrinol Metab 93(7): 2877–2884. doi: 10.1210/jc.2007-2247

55. Eichmann TO, Kumari M, Haas JT et al. (2012) Studies on the substrate and stereo/regioselectivity of adipose triglyceride lipase, hormone-sensitive lipase, and diacylglycerol-O-acyltransferases. J Biol Chem 287(49): 41446–41457. doi: 10.1074/jbc.M112.400416
56. Bartz R, Zehmer JK, Zhu M et al. (2007) Dynamic activity of lipid droplets: protein phosphorylation and GTP-mediated protein translocation. J Proteome Res 6(8): 3256–3265. doi: 10.1021/pr070158j
57. Xie X, Langlais P, Zhang X et al. (2014) Identification of a novel phosphorylation site in adipose triglyceride lipase as a regulator of lipid droplet localization. Am J Physiol Endocrinol Metab 306(12): E1449-59. doi: 10.1152/ajpendo.00663.2013
58. Mason RR, Meex RCR, Lee-Young R et al. (2012) Phosphorylation of adipose triglyceride lipase Ser(404) is not related to 5'-AMPK activation during moderate-intensity exercise in humans. Am J Physiol Endocrinol Metab 303(4): E534-41. doi: 10.1152/ajpendo.00082.2012
59. Ahmadian M, Abbott MJ, Tang T et al. (2011) Desnutrin/ATGL is regulated by AMPK and is required for a brown adipose phenotype. Cell Metab 13(6): 739–748. doi: 10.1016/j.cmet.2011.05.002
60. Lu X, Yang X, Liu J (2010) Differential control of ATGL-mediated lipid droplet degradation by CGI-58 and G0S2. Cell Cycle 9(14): 2719–2725. doi: 10.4161/cc.9.14.12181
61. UniProt (2018) 1-acylglycerol-3-phosphate O-acyltransferase ABHD5 (Mus musculus): UniProtKB - Q9DBL9 (ABHD5_MOUSE). mCGI-58 Sequence. http://www.uniprot.org/uniprot/Q9DBL9. Accessed 20 Jun 2018
62. Subramanian V, Rothenberg A, Gomez C et al. (2004) Perilipin A mediates the reversible binding of CGI-58 to lipid droplets in 3T3-L1 adipocytes. J Biol Chem 279(40): 42062–42071. doi: 10.1074/jbc.M407462200
63. Lai C-H (2000) Identification of Novel Human Genes Evolutionarily Conserved in Caenorhabditis elegans by Comparative Proteomics. Genome Research 10(5): 703–713. doi: 10.1101/gr.10.5.703
64. Lefèvre C, Jobard F, Caux F et al. (2001) Mutations in CGI-58, the gene encoding a new protein of the esterase/lipase/thioesterase subfamily, in Chanarin-Dorfman syndrome. Am J Hum Genet 69(5): 1002–1012. doi: 10.1086/324121
65. Ronchetti A, Prati D, Pezzotta MG et al. (2008) Severe steatohepatitis in a patient with a rare neutral lipid storage disorder due to ABHD5 mutation. J Hepatol 49(3): 474–477. doi: 10.1016/j.jhep.2008.05.027
66. Cakir M, Bruno C, Cansu A et al. (2010) Liver cirrhosis in an infant with Chanarin-Dorfman syndrome caused by a novel splice-site mutation in ABHD5. Acta Paediatr 99(10): 1592–1594. doi: 10.1111/j.1651-2227.2010.01869.x
67. Cakmak E, Alagozlu H, Yonem O et al. (2012) Steatohepatitis and liver cirrhosis in Chanarin-Dorfman syndrome with a new ABDH5 mutation. Clin Res Hepatol Gastroenterol 36(2): e34-7. doi: 10.1016/j.clinre.2011.12.007
68. Lord CC, Ferguson D, Thomas G et al. (2016) Regulation of Hepatic Triacylglycerol Metabolism by CGI-58 Does Not Require ATGL Co-activation. Cell Rep 16(4): 939–949. doi: 10.1016/j.celrep.2016.06.049
69. Radner FPW, Streith IE, Schoiswohl G et al. (2010) Growth retardation, impaired triacylglycerol catabolism, hepatic steatosis, and lethal skin barrier defect in mice lacking comparative gene identification-58 (CGI-58). J Biol Chem 285(10): 7300–7311. doi: 10.1074/jbc.M109.081877
70. Sanders MA, Madoux F, Mladenovic L et al. (2015) Endogenous and Synthetic ABHD5 Ligands Regulate ABHD5-Perilipin Interactions and Lipolysis in Fat and Muscle. Cell Metab 22(5): 851–860. doi: 10.1016/j.cmet.2015.08.023

71. Bezaire V, Mairal A, Ribet C et al. (2009) Contribution of adipose triglyceride lipase and hormone-sensitive lipase to lipolysis in hMADS adipocytes. J Biol Chem 284(27): 18282–18291. doi: 10.1074/jbc.M109.008631
72. Kien B, Grond S, Haemmerle G et al. (2018) ABHD5 stimulates PNPLA1-mediated ω-O-acylceramide biosynthesis essential for a functional skin permeability barrier. J Lipid Res 59(12): 2360–2367. doi: 10.1194/jlr.M089771
73. Miao H, Ou J, Peng Y et al. (2016) Macrophage ABHD5 promotes colorectal cancer growth by suppressing spermidine production by SRM. Nat Commun 7: 11716. doi: 10.1038/ncomms11716
74. Vieyres G, Welsch K, Gerold G et al. (2016) ABHD5/CGI-58, the Chanarin-Dorfman Syndrome Protein, Mobilises Lipid Stores for Hepatitis C Virus Production. PLoS Pathog 12(4): e1005568. doi: 10.1371/journal.ppat.1005568
75. Ou J, Miao H, Ma Y et al. (2014) Loss of abhd5 promotes colorectal tumor development and progression by inducing aerobic glycolysis and epithelial-mesenchymal transition. Cell Rep 9(5): 1798–1811. doi: 10.1016/j.celrep.2014.11.016
76. Sanders MA, Zhang H, Mladenovic L et al. (2017) Molecular Basis of ABHD5 Lipolysis Activation. Sci Rep 7: 42589. doi: 10.1038/srep42589
77. Gruber A, Cornaciu I, Lass A et al. (2010) The N-terminal region of comparative gene identification-58 (CGI-58) is important for lipid droplet binding and activation of adipose triglyceride lipase. J Biol Chem 285(16): 12289–12298. doi: 10.1074/jbc.M109.064469
78. Boeszoermenyi A, Nagy HM, Arthanari H et al. (2015) Structure of a CGI-58 motif provides the molecular basis of lipid droplet anchoring. J Biol Chem 290(44): 26361–26372. doi: 10.1074/jbc.M115.682203
79. Sahu-Osen A, Montero-Moran G, Schittmayer M et al. (2015) CGI-58/ABHD5 is phosphorylated on Ser239 by protein kinase A: control of subcellular localization. J Lipid Res 56(1): 109–121. doi: 10.1194/jlr.M055004
80. Heckmann BL, Zhang X, Xie X et al. (2013) The G0/G1 switch gene 2 (G0S2): regulating metabolism and beyond. Biochim Biophys Acta 1831(2): 276–281. doi: 10.1016/j.bbalip.2012.09.016
81. Russell L, Forsdyke DR (1991) A human putative lymphocyte G0/G1 switch gene containing a CpG-rich island encodes a small basic protein with the potential to be phosphorylated. DNA Cell Biol 10(8): 581–591. doi: 10.1089/dna.1991.10.581
82. Yamada T, Park CS, Shen Y et al. (2014) G0S2 inhibits the proliferation of K562 cells by interacting with nucleolin in the cytosol. Leuk Res 38(2): 210–217. doi: 10.1016/j.leukres.2013.10.006
83. Wang Y, Zhang Y, Zhu Y et al. (2015) Lipolytic inhibitor G0/G1 switch gene 2 inhibits reactive oxygen species production and apoptosis in endothelial cells. Am J Physiol , Cell Physiol 308(6): C496-504. doi: 10.1152/ajpcell.00317.2014
84. Lee P-H, Yamada T, Park CS et al. (2015) G0S2 modulates homeostatic proliferation of naïve $CD8^+$ T cells and inhibits oxidative phosphorylation in mitochondria. Immunol Cell Biol 93(7): 605–615. doi: 10.1038/icb.2015.9
85. Yamada T, Park CS, Burns A et al. (2012) The cytosolic protein G0S2 maintains quiescence in hematopoietic stem cells. PLoS ONE 7(5): e38280. doi: 10.1371/journal.pone.0038280
86. Zhang X, Heckmann BL, Campbell LE et al. (2017) G0S2: A small giant controller of lipolysis and adipose-liver fatty acid flux. Biochim Biophys Acta Mol Cell Biol Lipids 1862(10 Pt B): 1146–1154. doi: 10.1016/j.bbalip.2017.06.007

87. Zhang X, Xie X, Heckmann BL et al. (2014) Targeted disruption of G0/G1 switch gene 2 enhances adipose lipolysis, alters hepatic energy balance, and alleviates high-fat diet-induced liver steatosis. Diabetes 63(3): 934–946. doi: 10.2337/db13-1422
88. El-Assaad W, El-Kouhen K, Mohammad AH et al. (2015) Deletion of the gene encoding G0/G 1 switch protein 2 (G0s2) alleviates high-fat-diet-induced weight gain and insulin resistance, and promotes browning of white adipose tissue in mice. Diabetologia 58(1): 149–157. doi: 10.1007/s00125-014-3429-z
89. Ma T, Lopez-Aguiar AGN, Li A et al. (2014) Mice lacking G0S2 are lean and cold-tolerant. Cancer Biol Ther 15(5): 643–650. doi: 10.4161/cbt.28251
90. Ricquier D (2011) Uncoupling protein 1 of brown adipocytes, the only uncoupler: a historical perspective. Front Endocrinol (Lausanne) 2: 85. doi: 10.3389/fendo.2011.00085
91. Harms M, Seale P (2013) Brown and beige fat: development, function and therapeutic potential. Nat Med 19(10): 1252–1263. doi: 10.1038/nm.3361
92. UniProtKB (2018) P27469 (G0S2_HUMAN): G0/G1 switch protein 2. https://www.uniprot.org/uniprot/P27469
93. Schweiger M, Paar M, Eder C et al. (2012) G0/G1 switch gene-2 regulates human adipocyte lipolysis by affecting activity and localization of adipose triglyceride lipase. J Lipid Res 53(11): 2307–2317. doi: 10.1194/jlr.M027409
94. Kimmel AR, Sztalryd C (2016) The Perilipins: Major Cytosolic Lipid Droplet-Associated Proteins and Their Roles in Cellular Lipid Storage, Mobilization, and Systemic Homeostasis. Annu Rev Nutr 36: 471–509. doi: 10.1146/annurev-nutr-071813-105410
95. Hynson RMG, Jeffries CM, Trewhella J et al. (2012) Solution structure studies of monomeric human TIP47/perilipin-3 reveal a highly extended conformation. Proteins 80(8): 2046–2055. doi: 10.1002/prot.24095
96. Brasaemle DL (2007) Thematic review series: adipocyte biology. The perilipin family of structural lipid droplet proteins: stabilization of lipid droplets and control of lipolysis. J Lipid Res 48(12): 2547–2559. doi: 10.1194/jlr.R700014-JLR200
97. Lass A, Zimmermann R, Oberer M et al. (2011) Lipolysis - a highly regulated multi-enzyme complex mediates the catabolism of cellular fat stores. Prog Lipid Res 50(1): 14–27. doi: 10.1016/j.plipres.2010.10.004
98. Servetnick DA, Brasaemle DL, Gruia-Gray J et al. (1995) Perilipins are associated with cholesteryl ester droplets in steroidogenic adrenal cortical and Leydig cells. J. Biol. Chem. 270(28): 16970–16973
99. Brasaemle DL, Rubin B, Harten IA et al. (2000) Perilipin A increases triacylglycerol storage by decreasing the rate of triacylglycerol hydrolysis. J Biol Chem 275(49): 38486–38493. doi: 10.1074/jbc.M007322200
100. Tansey JT, Huml AM, Vogt R et al. (2003) Functional studies on native and mutated forms of perilipins. A role in protein kinase A-mediated lipolysis of triacylglycerols. J Biol Chem 278(10): 8401–8406. doi: 10.1074/jbc.M211005200
101. Yamaguchi T, Omatsu N, Matsushita S et al. (2004) CGI-58 interacts with perilipin and is localized to lipid droplets. Possible involvement of CGI-58 mislocalization in Chanarin-Dorfman syndrome. J Biol Chem 279(29): 30490–30497. doi: 10.1074/jbc.M403920200
102. Granneman JG, Moore H-PH, Granneman RL et al. (2007) Analysis of lipolytic protein trafficking and interactions in adipocytes. J Biol Chem 282(8): 5726–5735. doi: 10.1074/jbc.M610580200
103. Andrew S. Greenberg, John J. Egan, Sheree A. Wek, Nira B. Garty, E. Joan Blanchette-Mackie, Constantine Londos (1991) Perilipin, a Major Hormonally Regulated Adipocyte-specific Phosphoprotein Associated wiht the Periphery of Lipid Storage Droplets. J Biol Chem(266): 11341–11346

104. Shinoda K, Ohyama K, Hasegawa Y et al. (2015) Phosphoproteomics Identifies CK2 as a Negative Regulator of Beige Adipocyte Thermogenesis and Energy Expenditure. Cell Metab 22(6): 997–1008. doi: 10.1016/j.cmet.2015.09.029
105. Wang H, Hu L, Dalen K et al. (2009) Activation of hormone-sensitive lipase requires two steps, protein phosphorylation and binding to the PAT-1 domain of lipid droplet coat proteins. J Biol Chem 284(46): 32116–32125. doi: 10.1074/jbc.M109.006726
106. Souza SC, Muliro KV, Liscum L et al. (2002) Modulation of hormone-sensitive lipase and protein kinase A-mediated lipolysis by perilipin A in an adenoviral reconstituted system. J Biol Chem 277(10): 8267–8272. doi: 10.1074/jbc.M108329200
107. Wolins NE, Quaynor BK, Skinner JR et al. (2006) OXPAT/PAT-1 is a PPAR-induced lipid droplet protein that promotes fatty acid utilization. Diabetes 55(12): 3418–3428. doi: 10.2337/db06-0399
108. UniProt (2018) Perilipin-5 (Mus musculus): UniProtKB - Q8BVZ1 (PLIN5_MOUSE). mPlin5 Sequence. http://www.uniprot.org/uniprot/Q8BVZ1. Accessed 20 Jun 2018
109. Dalen KT, Dahl T, Holter E et al. (2007) LSDP5 is a PAT protein specifically expressed in fatty acid oxidizing tissues. Biochim Biophys Acta 1771(2): 210–227. doi: 10.1016/j.bbalip.2006.11.011
110. Yamaguchi T, Matsushita S, Motojima K et al. (2006) MLDP, a novel PAT family protein localized to lipid droplets and enriched in the heart, is regulated by peroxisome proliferator-activated receptor alpha. J Biol Chem 281(20): 14232–14240. doi: 10.1074/jbc.M601682200
111. Wang H, Bell M, Sreenivasan U et al. (2011) Unique regulation of adipose triglyceride lipase (ATGL) by perilipin 5, a lipid droplet-associated protein. J Biol Chem 286(18): 15707–15715. doi: 10.1074/jbc.M110.207779
112. Granneman JG, Moore H-PH, Mottillo EP et al. (2009) Functional interactions between Mldp (LSDP5) and Abhd5 in the control of intracellular lipid accumulation. J Biol Chem 284(5): 3049–3057. doi: 10.1074/jbc.M808251200
113. Granneman JG, Moore H-PH, Mottillo EP et al. (2011) Interactions of perilipin-5 (Plin5) with adipose triglyceride lipase. J Biol Chem 286(7): 5126–5135. doi: 10.1074/jbc.M110.180711
114. Pollak NM, Jaeger D, Kolleritsch S et al. (2015) The interplay of protein kinase A and perilipin 5 regulates cardiac lipolysis. J Biol Chem 290(3): 1295–1306. doi: 10.1074/jbc.M114.604744
115. Hoffman NJ, Parker BL, Chaudhuri R et al. (2015) Global Phosphoproteomic Analysis of Human Skeletal Muscle Reveals a Network of Exercise-Regulated Kinases and AMPK Substrates. Cell Metab 22(5): 922–935. doi: 10.1016/j.cmet.2015.09.001
116. Lundby A, Andersen MN, Steffensen AB et al. (2013) In vivo phosphoproteomics analysis reveals the cardiac targets of β-adrenergic receptor signaling. Sci Signal 6(278): rs11. doi: 10.1126/scisignal.2003506
117. Wilson-Grady JT, Haas W, Gygi SP (2013) Quantitative comparison of the fasted and re-fed mouse liver phosphoproteomes using lower pH reductive dimethylation. Methods 61(3): 277–286. doi: 10.1016/j.ymeth.2013.03.031
118. Drevinge C, Dalen KT, Mannila MN et al. (2016) Perilipin 5 is protective in the ischemic heart. Int J Cardiol 219: 446–454. doi: 10.1016/j.ijcard.2016.06.037
119. Kuramoto K, Okamura T, Yamaguchi T et al. (2012) Perilipin 5, a lipid droplet-binding protein, protects heart from oxidative burden by sequestering fatty acid from excessive oxidation. J Biol Chem 287(28): 23852–23863. doi: 10.1074/jbc.M111.328708
120. Mason RR, Mokhtar R, Matzaris M et al. (2014) PLIN5 deletion remodels intracellular lipid composition and causes insulin resistance in muscle. Mol Metab 3(6): 652–663. doi: 10.1016/j.molmet.2014.06.002

121. Pollak NM, Schweiger M, Jaeger D et al. (2013) Cardiac-specific overexpression of perilipin 5 provokes severe cardiac steatosis via the formation of a lipolytic barrier. J Lipid Res 54(4): 1092–1102. doi: 10.1194/jlr.M034710
122. Wang H, Sreenivasan U, Gong D-W et al. (2013) Cardiomyocyte-specific perilipin 5 overexpression leads to myocardial steatosis and modest cardiac dysfunction. J Lipid Res 54(4): 953–965. doi: 10.1194/jlr.M032466
123. Wang C, Zhao Y, Gao X et al. (2015) Perilipin 5 improves hepatic lipotoxicity by inhibiting lipolysis. Hepatology 61(3): 870–882. doi: 10.1002/hep.27409
124. Bosma M, Sparks LM, Hooiveld GJ et al. (2013) Overexpression of PLIN5 in skeletal muscle promotes oxidative gene expression and intramyocellular lipid content without compromising insulin sensitivity. Biochim Biophys Acta 1831(4): 844–852. doi: 10.1016/j.bbalip.2013.01.007
125. Gandotra S, Lim K, Girousse A et al. (2011) Human frame shift mutations affecting the carboxyl terminus of perilipin increase lipolysis by failing to sequester the adipose triglyceride lipase (ATGL) coactivator AB-hydrolase-containing 5 (ABHD5). J Biol Chem 286(40): 34998–35006. doi: 10.1074/jbc.M111.278853
126. Agilent QuikChange II Site-Directed Mutagenesis Kit: Instruction Manual. Catalog #200523 (10 reactions) and #200524 (30 reactions). https://www.agilent.com/cs/library/usermanuals/Public/200523.pdf. Accessed 21 Mar 2018
127. Sigma-Aldrich/Merck SIG10 Chemically Competent Cells: Transformation Protocol for SIG10 Cells. https://www.sigmaaldrich.com/technical-documents/protocols/biology/sig10-chemically-competent-cells.html. Accessed 21 Mar 2018
128. Sigma-Aldrich/Merck (2018) LB Broth with agar (Lennox): Powder microbial growth medium. https://www.sigmaaldrich.com/catalog/product/sigma/l2897?lang=de&region=AT. Accessed 13 Jun 2018
129. Promega Wizard® Plus SV Minipreps DNA Purifi cation System: Instructions for Use of Products. https://at.promega.com/-/media/files/resources/protocols/technical-bulletins/0/wizard-plus-sv-minipreps-dna-purification-system-protocol.pdf. Accessed 21 Mar 2018
130. Thermo Fisher (2019) NanoDrop 2000/2000c Spectrophotometer: V1.0 User Manual. https://mlz-garching.de/files/nanodrop_2000_user_manual.pdf. Accessed 05 Jun 2019
131. LGC (2019) Single Sample Sequencing: "Ready2 run with flexible solutions and premium quality". https://biosearch-cdn.azureedge.net/assetsv6/single-sample-sequencing-data-sheet.pdf
132. New England Biolabs Datasheet for Quick-Load® 1 kb DNA Ladder (N0468; Lot 0401302)
133. Lottspeich F, Engels JW (eds) (2009) Bioanalytik, 2., [aktualisierte und erw.] Aufl., [Nachdr.]. Spektrum Akad. Verl., Heidelberg
134. National Center for Biotechnology Information (2018) Standard Nucleotide BLAST - NCBI. https://blast.ncbi.nlm.nih.gov/Blast.cgi?PROGRAM=blastn&PAGE_TYPE=BlastSearch&LINK_LOC=blasthome. Accessed 26 Jun 2018
135. ExPASy - Bioinformatics Resource Portal (2018) Translate tool. https://web.expasy.org/translate/
136. Addgene (2018) Plasmid: pECFP-C1. https://www.addgene.org/vector-database/2445/
137. UniProt Patatin-like phospholipase domain-containing protein 2 (Mus Musculus) Sequence: UniProtKB - Q8BJ56 (PLPL2_MOUSE). mATGL Sequence. http://www.uniprot.org/uniprot/Q8BJ56. Accessed 23 Mar 2018
138. Miyoshi H, Souza SC, Zhang H-H et al. (2006) Perilipin promotes hormone-sensitive lipase-mediated adipocyte lipolysis via phosphorylation-dependent and -independent mechanisms. J Biol Chem 281(23): 15837–15844. doi: 10.1074/jbc.M601097200

139. Thermo Fisher Useful Numbers for Cell Culture: Useful information for various sizes of cell culture dishes and flasks. https://www.thermofisher.com/us/en/home/references/gibco-cell-culture-basics/cell-culture-protocols/cell-culture-useful-numbers.html. Accessed 12 Apr 2018
140. ATCC COS-7 (ATCC® CRL-1651™). https://www.lgcstandards-atcc.org/products/all/CRL-1651.aspx?geo_country=at#documentation. Accessed 12 Apr 2018
141. OZBiosciences COSFectTM Transfection Reagent: Instruction Manual. https://www.ozbiosciences.com/transfection-cell-specific/76-cos-cells-transfection-cosfect-transfection-reagent.html. Accessed 11 Apr 2018
142. Thermo Fisher (2018) Novex™ Sharp Pre-stained Protein Standard. https://www.thermofisher.com/order/catalog/product/LC5800. Accessed 20 Jun 2018
143. Promega FuGENE 6 Transfection Reagent: Instructions for Use of Products E1691, E2692 and E2693. https://www.promega.com/-/media/files/resources/protocols/technical-manuals/101/fugene-6-transfection-reagent-protocol.pdf. Accessed 11 Apr 2018
144. Thermo Fisher Lipofectamine™ 3000 Reagent: User Guide. https://tools.thermofisher.com/content/sfs/manuals/lipofectamine3000_protocol.pdf. Accessed 11 Apr 2018
145. Birner-Gruenberger R, Susani-Etzerodt H, Waldhuber M et al. (2005) The lipolytic proteome of mouse adipose tissue. Mol Cell Proteomics 4(11): 1710–1717. doi: 10.1074/ mcp.M500062-MCP200
146. Seahorse Bioscience, Agilent (2018) Preparation of Bovine Serum Albumin-Palmitate. http://www.wklab.org/wp-content/uploads/2016/02/Palmitate-BSA_Prep_SOP_v080624.pdf. Accessed 20 Jun 2018
147. Gluzman Y (1981) SV40-transformed simian cells support the replication of early SV40 mutants. Cell 23(1): 175–182. doi: 10.1016/0092-8674(81)90282-8
148. Cell Signaling Technology (2018) ATGL Antibody #2138. https://www.cellsignal.at/products/primary-antibodies/atgl-antibody/2138
149. Vegliante R, Di Leo L, Ciccarone F et al. (2018) Hints on ATGL implications in cancer: beyond bioenergetic clues. Cell Death Dis 9(3): 316. doi: 10.1038/s41419-018-0345-z
150. UniProt (2018) Perilipin-1 (Mus musculus) Sequence: UniProtKB - Q8CGN5 (PLIN1_MOUSE). mPlin1 Sequence. http://www.uniprot.org/uniprot/Q8CGN5. Accessed 20 Jun 2018
151. UniProtKB (2018) UniProtKB - X5DSL3 (X5DSL3_ANAMA). Submitted name: MCherry fluorescent protein. https://www.uniprot.org/uniprot/X5DSL3
152. UniProtKB (2018) Yellow fluorescent protein - A0A059PIR9. https://www.uniprot.org/uniprot/A0A059PIR9
153. Kim TK, Eberwine JH (2010) Mammalian cell transfection: the present and the future. Anal Bioanal Chem 397(8): 3173–3178. doi: 10.1007/s00216-010-3821-6
154. Juers DH, Matthews BW, Huber RE (2012) LacZ β-galactosidase: structure and function of an enzyme of historical and molecular biological importance. Protein Sci 21(12): 1792–1807. doi: 10.1002/pro.2165
155. Arppe R, Carro-Temboury MR, Hempel C et al. (2017) Investigating dye performance and crosstalk in fluorescence enabled bioimaging using a model system. PLoS ONE 12(11): e0188359. doi: 10.1371/journal.pone.0188359
156. Moore H-PH, Silver RB, Mottillo EP et al. (2005) Perilipin targets a novel pool of lipid droplets for lipolytic attack by hormone-sensitive lipase. J Biol Chem 280(52): 43109–43120. doi: 10.1074/jbc.M506336200
157. Mottillo EP, Paul GM, Moore H-PH et al. (2014) Use of fluorescence microscopy to probe intracellular lipolysis. Meth Enzymol 538: 263–278. doi: 10.1016/B978-0-12-800280-3.00015-3

158. UniProt (2018) Cyan fluorescent protein (Aequorea victora): UniProtKB - A0A059PIU2 (A0A059PIU2_AEQVI). http://www.uniprot.org/uniprot/A0A059PIU2. Accessed 23 Jun 2018
159. Heymann MC, Rabe S, Ruß S et al. (2015) Fluorescent tags influence the enzymatic activity and subcellular localization of procaspase-1. Clin Immunol 160(2): 172–179. doi: 10.1016/j.clim.2015.05.011
160. Margolin W (2012) The price of tags in protein localization studies. J Bacteriol 194(23): 6369–6371. doi: 10.1128/JB.01640-12
161. Jensen EC (2012) Use of fluorescent probes: their effect on cell biology and limitations. Anat Rec (Hoboken) 295(12): 2031–2036. doi: 10.1002/ar.22602
162. Puchtler H, Meloan SN (1985) On the chemistry of formaldehyde fixation and its effects on immunohistochemical reactions. Histochemistry 82(3): 201–204. doi: 10.1007/BF00501395
163. Fam TK, Klymchenko AS, Collot M (2018) Recent Advances in Fluorescent Probes for Lipid Droplets. Materials (Basel) 11(9). doi: 10.3390/ma11091768
164. Vector Laboratories (2019) VECTASHIELD® Antifade Mounting Media. https://vectorlabs.com/browse/vectashield-antifade-mounting-media. Accessed 10 Jul 2019
165. Rowe ER, Mimmack ML, Barbosa AD et al. (2016) Conserved Amphipathic Helices Mediate Lipid Droplet Targeting of Perilipins 1-3. J Biol Chem 291(13): 6664–6678. doi: 10.1074/jbc.M115.691048
166. Thiam AR, Farese RV, Walther TC (2013) The biophysics and cell biology of lipid droplets. Nat Rev Mol Cell Biol 14(12): 775–786. doi: 10.1038/nrm3699
167. Hsieh K, Lee YK, Londos C et al. (2012) Perilipin family members preferentially sequester to either triacylglycerol-specific or cholesteryl-ester-specific intracellular lipid storage droplets. J Cell Sci 125(Pt 17): 4067–4076. doi: 10.1242/jcs.104943
168. Tansey JT, Sztalryd C, Gruia-Gray J et al. (2001) Perilipin ablation results in a lean mouse with aberrant adipocyte lipolysis, enhanced leptin production, and resistance to diet-induced obesity. Proc Natl Acad Sci U S A 98(11): 6494–6499. doi: 10.1073/pnas.101042998
169. Martinez-Botas J, Anderson JB, Tessier D et al. (2000) Absence of perilipin results in leanness and reverses obesity in Lepr(db/db) mice. Nat Genet 26(4): 474–479. doi: 10.1038/82630
170. Gandotra S, Le Dour C, Bottomley W et al. (2011) Perilipin deficiency and autosomal dominant partial lipodystrophy. N Engl J Med 364(8): 740–748. doi: 10.1056/NEJMoa1007487
171. Birner-Gruenberger R, Hermetter A (2007) Activity-Based Proteomics of Lipolytic Enzymes. CDDT 4(1): 1–11. doi: 10.2174/157016307781115458
172. Florian Hoff LM How to Prepare Your Specimen for Immunofluorescence Microscopy. https://www.leica-microsystems.com/science-lab/how-to-prepare-your-specimen-for-immunofluorescence-microscopy/. Accessed 11 Apr 2019
173. Hoffman EA, Frey BL, Smith LM et al. (2015) Formaldehyde crosslinking: a tool for the study of chromatin complexes. J Biol Chem 290(44): 26404–26411. doi: 10.1074/jbc.R115.651679
174. Grizzle WE (2009) Special symposium: fixation and tissue processing models. Biotech Histochem 84(5): 185–193. doi: 10.3109/10520290903039052
175. Burgess GM, McKinney JS, Fabiato A et al. (1983) Calcium pools in saponin-permeabilized guinea pig hepatocytes. J. Biol. Chem. 258(24): 15336–15345
176. Jamur MC, Oliver C (2010) Permeabilization of cell membranes. Methods Mol Biol 588: 63–66. doi: 10.1007/978-1-59745-324-0_9
177. Clive R. Taylor, Lars Rudbeck Sixth Edition of Dako's Guidebook to Immunohistochemical Staining Methods. https://www.agilent.com/cs/library/technicaloverviews/public/08002_ihc_staining_methods.pdf. Accessed 11 Apr 2019

178. Tegge W, Frank R, Hofmann F et al. (1995) Determination of cyclic nucleotide-dependent protein kinase substrate specificity by the use of peptide libraries on cellulose paper. Biochemistry 34(33): 10569–10577. doi: 10.1021/bi00033a032
179. UniProt (2018) Human cGMP-dependent proteinkinase Isoform Iβ: UniProtKB - Q13976 (KGP1_HUMAN). http://www.uniprot.org/uniprot/Q13976. Accessed 24 Jun 2018
180. Thermo Fisher INSTRUCTIONS HisPur™ Ni-NTA Spin Columns. https://www.thermofisher.com/order/catalog/product/88224#/pdp-documents. Accessed 27 Mar 2018
181. Dorfer V, Pichler P, Stranzl T et al. (2014) MS Amanda, a universal identification algorithm optimized for high accuracy tandem mass spectra. J Proteome Res 13(8): 3679–3684. doi: 10.1021/pr500202e
182. The Global Proteome Machine (2018) cRAP protein sequences. https://www.thegpm.org/crap/. Accessed 27 Aug 2018
183. Thermo Fisher (2018) Ni-NTA Purification System: For purification of polyhistidine-containing recombinant proteins. https://tools.thermofisher.com/content/sfs/manuals/ninta_system_man.pdf
184. Parker L, Engel-Hall A, Drew K et al. (2008) Investigating quantitation of phosphorylation using MALDI-TOF mass spectrometry. J Mass Spectrom 43(4): 518–527. doi: 10.1002/jms.1342
185. Morrison S, McGee SL (2015) 3T3-L1 adipocytes display phenotypic characteristics of multiple adipocyte lineages. Adipocyte 4(4): 295–302. doi: 10.1080/21623945.2015.1040612
186. Pidoux G, Witczak O, Jarnæss E et al. (2011) Optic atrophy 1 is an A-kinase anchoring protein on lipid droplets that mediates adrenergic control of lipolysis. EMBO J 30(21): 4371–4386. doi: 10.1038/emboj.2011.365
187. Hofer P, Boeszoermenyi A, Jaeger D et al. (2015) Fatty Acid-binding Proteins Interact with Comparative Gene Identification-58 Linking Lipolysis with Lipid Ligand Shuttling. J Biol Chem 290(30): 18438–18453. doi: 10.1074/jbc.M114.628958
188. Beller M, Sztalryd C, Southall N et al. (2008) COPI complex is a regulator of lipid homeostasis. PLoS Biol 6(11): e292. doi: 10.1371/journal.pbio.0060292
189. Rondini EA, Mladenovic-Lucas L, Roush WR et al. (2017) Novel Pharmacological Probes Reveal ABHD5 as a Locus of Lipolysis Control in White and Brown Adipocytes. J Pharmacol Exp Ther 363(3): 367–376. doi: 10.1124/jpet.117.243253
190. Addgene Sequencing Primers: Commonly Used Primers. https://www.addgene.org/mol-bio-reference/sequencing-primers/. Accessed 21 Mar 2018

List of Tables

Table 1**: PCR Program used for SDM reactions** 22

Table 2: **Filterset of Olympus IX51 inverted microscope** 32

Table 3: **Channel settings used for fluorescence microscopy on Nikon A1 confocal laser scanning system** 33

Table 4: **Channel settings used for immunofluorescence microscopy on Nikon A1 confocal laser scanning system** 34

Table 5: **CGI-58 peptides identified by MS.** 67

Table 6: **Summary of all provided plasmid templates listed with all contained mutations after first sequencing (column "contained construct").** 87

Table 7: **List of all designed SDM-primers with assigned names, 5'-3'-sequence, mutations that they were used to introduce and their respective designer.** 88

Table 8: **List of all designed sequencing primers, their 5'-3'-sequence, the plasmids they were used to sequence and their respective designer.** 89

Table 9: **Recipe for SOC-medium** 89

Table 10: **Reaction mixes used for PKA/PKG Assays.** 89

Table 11: **List of CGI-58 peptides (AspN digest) for preferred fragmentation containing the phosphorylation site of interest.** 90

List of Figures

Figure 1: **Molecular structure of triacylglycerols**. 10
Figure 2: **Overview of lipolysis in adipocytes**. 12
Figure 3**: 1% Agarose gel run of various SDM reaction plasmid templates and their consecutive SDM-PCR reaction products to control successful amplification** 25
Figure 4**: DNA sequence of sequencing result of Plin1 A508T L512Q in vector pEYFP-N1**. 27
Figure 5: **Legend explaining features in DNA sequencing results** (see Figure 6) 27
Figure 6**: Amino acid sequence of sequencing result of Plin1 A508T L512Q in vector pEYFP-N1.** 27
Figure 7**: Legend explaining features in translated amino acid sequence of sequencing result** 27
Figure 10: **Endogenous Plin5 could be present in COS-7 Lysates.** 36
Figure 9: **Endogenous Plin1 may be expressed in COS-7 Lysates.**. 36
Figure 8: **Endogenous ATGL is expressed in COS-7 Lysates**.. 35
Figure 11**: Endogenous CGI-58 could be present in COS-7 Lysates.** 37
Figure 12**: Analysis of expression of CGI-58-mCherry-variations in co-transfected COS-7 cells**. 38
Figure 13: **Analysis of Plin5-EYFP expression in co-transfected COS-7 cells**. 39
Figure 14: **Analysis of Plin1-EYFP expression in co-transfected COS-7 cells**. 39
Figure 15**: COSFect in ratio 2:1 delivered best transfection results in β-galactosidase assay after 4 hours of incubation.** 41
Figure 16**: COSFect in ratio 2:1 delivered best transfection results in β-galactosidase assay after 22 hours of incubation.** 41
Figure 17: **Excitation and emission spectra of ECFP (blue), EYFP (green) and mCherry (red).** 42
Figure 18: **mCGI-58-mCherry and Plin5-EYFP expression of transfected COS-7 cells.** 44
Figure 19: **Very low ECFP-ATGL expression in transfected COS-7 cells.** 44
Figure 20: **ECFP-ATGL is expressed in transfected COS-7 cell lysates**. 45
Figure 21: **COS-7 cells expressing wild-type mCGI-58-mCherry and wild-type Plin1-EYFP under basal conditions.** 48
Figure 22: **Under basal conditions Plin1 and CGI-58 in varying forms co-localize at the LD** 50
Figure 23: **Mutation of mCGI-58 S239A may lead to reduced trans-localization of CGI-58 to cytosol after lipolysis stimulation. Results of experiments with mCGI-58 Y330F mutants remain inconclusive** 52
Figure 24: **Non-transfected COS-7 control cells do not show signals when incubated with antibodies against CGI-58 and Plin1.** 56
Figure 25: **Under basal conditions Plin1 and varying CGI-58 constructs mainly co-localize at the LD in immunofluorescence experiments.** 57

Figure 26: **Expression of Plin1 and varying CGI-58 constructs under lipolysis stimulated conditions observed via immunofluorescence microscopy.** 58
Figure 27: **Estimation of amount of overexpressed CGI-58 in transformed E. coli cell lysates.**..... 65
Figure 28: **Plasmid map provided by Dr. Granneman (Wayne State University School of Medicine, Detroit) for the EYFP-plasmid containing the Perilipin-5-EYFP construct (FLmldp_EYFP).** 91
Figure 29: **Plasmid map provided by Dr. Granneman (Wayne State University School of Medicine, Detroit) for an EYFP-N1 plasmid containing the wild-type ABHD5-mCherry (=CGI-58-mCherry) gene** 91
Figure 30: **Sequence of mCGI-58 construct containing an N-terminal smt3 fusion tag, a 6XHIS-tag and a tobacco etch virus (TEV) protease cleavage site provided by Dr. M. Oberer (Karl-Franzens University Graz) A** 92
Figure 31: **DNA/amino acid sequence of murine wild-type perilipin 1 obtained from the NCBI database**..... 92
Figure 32: **DNA/amino acid sequence of murine wild-type perilipin 5 obtained from the NCBI database**..... 93
Figure 33: **DNA/amino acid sequence of murine wild-type ATGL obtained from the NCBI database** 93
Figure 34: **DNA/amino acid sequence of murine wild-type CGI-58 obtained from the NCBI database** 94
Figure 35: **DNA/amino acid sequence of human wild-type CG-58 obtained from the NCBI database** (..... 94
Figure 36: **DNA/amino acid sequence of murine G0S2 obtained from the NCBI database** 95
Figure 37: **DNA/amino acid sequence of human G0S2 obtained from the NCBI database** 95
Figure 38: **Sequencing result of murine CGI-58 wild-type cloned in vector pcDNA4/HisMax C.**. 96
Figure 39: **Sequencing result of murine CGI-58 S239A cloned in vector pcDNA4/HisMax C.**. 96
Figure 40: **Sequencing result of murine CGI-58 S239D cloned in vector pcDNA4/HisMax C.**. 97
Figure 41**: Sequencing result of murine CGI-58 Y330F cloned in vector pcDNA4/HisMax C.**..... 97
Figure 42: **Sequencing result of murine CGI-58 S239A Y330F cloned in vector pcDNA4/HisMax C**... 98
Figure 43: **Sequencing result of murine CGI-58 R236A cloned in vector pcDNA4/HisMax C.** 98
Figure 44: **Sequencing result of human CGI-58 wild-type cloned in vector pcDNA3.1.**. 99
Figure 45: **Sequencing result of human CGI-58 S239E cloned in vector pcDNA3.1.**. 99
Figure 46: **Sequencing result of murine ATGL C238S cloned in vector pcDNA4/HisMaxC.** 100
Figure 47: **Sequencing result of murine G0S2 wild-type cloned in vector pcDNA4/HisMaxC.**. 100
Figure 48**: Sequencing result of murine G0S2 S97A cloned in vector pcDNA4/HisMaxC**..... 101
Figure 49: **Sequencing result of murine G0S2 S97D cloned in vector pcDNA4/HisMaxC**..... 101

Figure 50: **Sequencing result of human G0S2 wild-type cloned in vector pcDNA4/HisMaxC.** 101
Figure 51: **Sequencing result of murine Plin5 wild-type cloned in vector pcDNA4/HisMaxC.** 102
Figure 52: **Sequencing result of murine Plin5 S155A cloned in vector pcDNA4/HisMaxC.** 102
Figure 53: **Sequencing result of murine mCGI-58-mCherry wild-type cloned in vector pEYFP-N1.** .103
Figure 54: **Sequencing result of murine mCGI-58-mCherry S239A cloned in vector pEYFP-N1.**. 103
Figure 55: **Sequencing result of murine mCGI-58-mCherry S239D cloned in vector pEYFP-N1.** 104
Figure 56: **Sequencing result of murine mCGI-58-mCherry Y330F cloned in vector pEYFP-N1.** 104
Figure 57: **Sequencing result of murine mCGI-58-mCherry S239A Y330F cloned in vector pEYFP-N1.** 105
Figure 58: **Sequencing result of murine ECFP-ATGL wild-type cloned in vector pECFP-C1.** 105
Figure 59: **Sequencing result of murine ECFP-ATGL C238S cloned in vector pEYCP-C1.**..... 106
Figure 60: **Sequencing result of murine Plin1-EYFP A508T Q512L cloned in vector pEYFP-N1.** 107
Figure 61**: Sequencing result of murine Plin1-EYFP A508T cloned in vector pEYFP-N1.**. 108
Figure 62: **Sequencing result of murine Plin1-EYFP wild-type cloned in vector pEYFP-N1.**. 109
Figure 63**: Sequencing result of murine Plin1-EYFP S433A S492A S517A cloned in vector pEYFP-N1**. 110
Figure 64: **Sequencing result of murine Plin5-EYFP wild-type cloned in vector pEYFP-N1.**. 111
Figure 65: **Sequencing result of murine Plin5-EYFP S155A cloned in vector pEYFP-N1**.. 112
Figure 66: **Additional information to human cGMP-dependent proteinkinase (PKG) provided by Dr. D. Bertinetti** 113

Appendix

Tables

Table 6: ***Summary of all provided plasmid templates listed with all contained mutations after first sequencing (column "contained construct").*** *The original vectors, the DNA was cloned into, can be found in column 2. Cloning sites of the contained constructs were listed if known. Column 4 shows the mutations that were introduced in following experiments. For better overview references to get further information to the original plasmids are listed in the far-right column.*

Contained Construct	**Original Vector**	**Cloning site**	**Consecutively introduced Mutations**	**References for plasmid information**
mG0S2	pcDNA/HisMaxC		S97A; S97D	[93]
hG0S2	pcDNA/HisMaxC		-	[93]
mCGI-58	pcDNA/HisMaxC		S239A; S239D; Y330F; S239A Y330F	[50]
hCGI-58-Yn	pcDNA3.1		S239E	[125]
ATGL	pcDNA/HisMaxC	KpnI/XhoI	C238S	[50]
Plin5	pcDNA/HisMaxC		S155A	[114]
ECFP-ATGL-R30H	ECFP-C1	HindIII/KpnI	C238S	[102]
mPlin1-A508T-Q512L - EYFP	EYFP-N1	KpnI/KpnI	T508A; L512Q	[102]
mPlin1-S433-S492A-S517A-EYFP	EYFP-N1	EcoRI/NotI	-	[102]
FL mPlin5-EYFP	EYFP-N1	HindIII/KpnI	S155A	[113] Figure 28 in appendix
WT mCGI-58-mCherry	EYFP-N1	AgeI/NotI	S239A; S239D; Y330F; S239A Y330F	[17] Figure 29 in appendix
6xHis-Smt-TEV-mCGI-58 WT	pET-28 b (+)	BamHI/XhoI	R236A	Figure 30 in appendix

Table 7: ***List of all designed SDM-primers with assigned names, 5'-3'-sequence, mutations that they were used to introduce and their respective designer.*** *Exchanged bases are marked fat and underlined.*

Primer Name	**Sequence 5' to 3'**	**Used for mutation**	**designed by**
Plin1_WT_Mut1A	CCGACTTCTTGCGCAGC**T**GGCTGTACTG	L512Q	Julia Kohlbacher
Plin1_WT_Mut1B	CAGTACAGCC**A**GCTGCGCAAGAAGTCGG	L512Q	
Plin1_WT_Mut2A	CTGTACTGCG**C**GCGGCCCAGGATGG	T508A	
Plin1_WT_Mut2B	CCATCCTGGGCCGC**G**CGCAGTACAG	T508A	
Plin5 S155A 1	CCGGCGTTGG**GC**TGGGGAGCTGAGG	S155A	
Plin5 S155A 2	CGCCTCAGCTCCCCA**GC**CCAACGCC	S155A	
mCGI58-S239A1	CTTCAAACATAGAGG**C**GTACTTCCGCTTGAAATC	S239A	
mCGI58-S239A2	GATTTCAAGCGGAAGTAC**G**CCTCTATGTTTGAAG	S239A	
mCGI58-S239D1	CTTCAAACATAGAG**TC**GTACTTCCGCTTGAAATC	S239D	
mCGI58-S239D2	GATTTCAAGCGGAAGTAC**GA**CTCTATGTTTGAAG	S239D	
mCGI58Y330Ffwd	GGGCGGGGCATT**T**TGTGTATGCAGATCAG"	Y330F	
mCGI58Y330Frev	CTGATCTGCATACACA**A**AATGCCCCGCCC"	Y330F	
mATGLC238Sfwd	CCTCCGAGAGATGT**C**CAAACAGGGCTAC"	C238S	
mATGLC238rev	GTAGCCCTGTTTG**G**ACATCTCTCGGAGG"	C238S	
mCGI58 R236A1	CAAACATAGAGGAGTACTTC**GC**CTTGAAATCAGGCCTCAAAC	R236A	
mCGI58 R236A2	GTTTGAGGCCTGATTTCAAG**GC**GAAGTACTCCTCTATGTTTG	R236A	
mABHD5-S239A1	GTCATCTTCAAACATAGAGG**C**GTACTTCCGCTTGAAATCAG	S239A	Anita Sahu
mABHD5-S239A2	CTGATTTCAAGCGGAAGTAC**G**CCTCTATGTTTGAAGATGAC	S239A	
mABHD5-S239D1	GTGTCATCTTCAAACATAGAG**TC**GTACTTCCGCTTGAAATCAGG	S239D	
mABHD5-S239D2	CCTGATTTCAAGCGGAAGTAC**GA**CTCTATGTTTGAAGATGACAC	S239D	
mG0S2-S97A1	CTGCCGGAGGGC**C**AGGGCCCGGC	S97A	
mG0S2-S97A2	GCCGGGCCCT**G**GCCCTCCGGCAG	S97A	
mG0S2-S97D1	GTGCTGCCGGAGG**TC**CAGGGCCCGGCTG	S97D	
mG0S2-S97D2	CAGCCGGGCCCTG**GA**CCTCCGGCAGCAC	S97D	
hABHD5_S237E AS	TCGTCTTCGAACATTGA**CTC**ATACTTTCGTTTGAAATCAGG-CCTTAAACGCTG	S237E	
hABHD5_S237E S	CAGCGTTTAAGGCCTGATTTCAAACGAAAGTAT**GAG**TCAA-TGTTCGAAGACGA	S237E	

Table 8: ***List of all designed sequencing primers, their 5'-3'-sequence, the plasmids they were used to sequence and their respective designer.*** *ABHD5-EYFP-N1_Cherry and ATGL fwd middle seq were designed using earlier sequencing results. Sequence templates for all other listed sequencing primers were found online [190].*

Primer Name	Sequence 5' to 3'	Used for Sequencing of	designed by
CMV (forward)	CGCAAATGGGCGGTAGGCGTG	EYFP-N1 Plasmids	[190]
EGFP-N (reverse)	CGTCGCCGTCCAGCTCGACCAG	EYFP-N1 Plasmids	
EGFP-C	CATGGTCCTGCTGGAGTTCGTG	ECFP-ATGL	
EBV Reverse	GTGGTTTGTCCAAACTCATC	not used	
T7 (fwd)	TAATACGACTCACTATAGGG	HisMaxC- & pET-28(+) Plasmids	
T7 Terminator	GCTAGTTATTGCTCAGCGG	pET-28(+) Plasmids	
BGH (rev)	TAGAAGGCACAGTCGAGG	HisMaxC Plasmids	
EBV (rev)	GTGGTTTGTCCAAACTCATC	Not used	
ABHD5- EYFP-N1_Cherry	ATGAACTCCTTGATGATGGCCATGTTA	ABHD5-mCherry	Julia Kohlbacher
ATGL fwd middle seq (fwd)	CTTTCCAACATGCTACCAGTGCGCCTG	ECFP-ATGL	

Table 9: ***Recipe for SOC-medium*** *Medium was used for the transformation of plasmids produced via SDM-reaction into XL-10- or SIG10-cells*

Reagent	**Final concentration**
Tryptone	2 % (w/v)
Yeast extract	0,5% (m/v)
NaCl	10 mM
KCl	2,5 mM
MgCl2	10 mM
Glucose	20 mM

Table 10: ***Reaction mixes used for PKA/PKG Assays.*** *After binding of CGI-58 constructs to the Ni-NTA Spin Columns and a buffer exchange, the according PKA-, PKG- or No PKA reaction mix was added to the columns to react with the CGI-58 construct bound on the column.*

PKG	
Solution	**V [µL]**
PKG Buffer	149
ATP (5mM)	40
DTT (25mM)	8
cGMP(100µM)	2
PKG	1

PKA	
Solution	**V [µL]**
PKA Buffer	151
ATP (5mM)	40
DTT (25mM)	8
PKA	1

NO PKA	
Solution	**V [µL]**
PKA Buffer	152
ATP (5mM)	40
DTT (25mM)	8

Table 11: ***List of CGI-58 peptides (AspN digest) for preferred fragmentation containing the phosphorylation site of interest.*** *Sequences, modification, sum formula and their mass to charge ratio (m/z) according to different charges (z) of all possibly interesting CGI-58 wild-type and CGI-58 R236A peptides used for preferred fragmentation during LC-MS/MS analysis*

CGI-58 wild-type peptides						
Sequence	**Modification 1**	**Modification 2**	**Sum formula**	**m/z z=1**	**m/z z=2**	**m/z z=3**
DFKRKYSSMFE			$C_{65}H_{96}N_{16}O_{19}S_1$	1436,68	719,35	479,90
DFKRKY[S]SMFE	Phos-Ser		$C_{65}H_{97}N_{16}O_{22}S_1P$	1516,64	759,33	506,55
DFKRKYSS[M]FE	Oxidation-M		$C_{65}H_{96}N_{16}O_{20}S_1$	1452,67	727,34	485,23
DFKRKY[S]S[M]FE	Phos-Ser	Oxidation-M	$C_{65}H_{97}N_{16}O_{23}S_1P$	1532,64	767,33	511,89
CGI-58 R236A peptides						
Sequence	**Modification 1**	**Modification 2**	**Sum formula**	**MW**	**z=2**	**z=3**
DFKAKYSSMFE			$C_{62}H_{89}N_{13}O_{19}S_1$	1351,61	676,81	451,54
DFKAKY[S]SMFE	Phos-Ser		$C_{62}H_{90}N_{13}O_{22}S_1P$	1431,58	716,80	478,20
DFKAKYSS[M]FE	Oxidation-M		$C_{62}H_{89}N_{13}O_{20}S_1$	1367,61	684,81	456,88
DFKAKY[S]S[M]FE	Phos-Ser	Oxidation-M	$C_{62}H_{90}N_{13}O_{23}S_1P$	1447,57	724,79	483,53

Figures

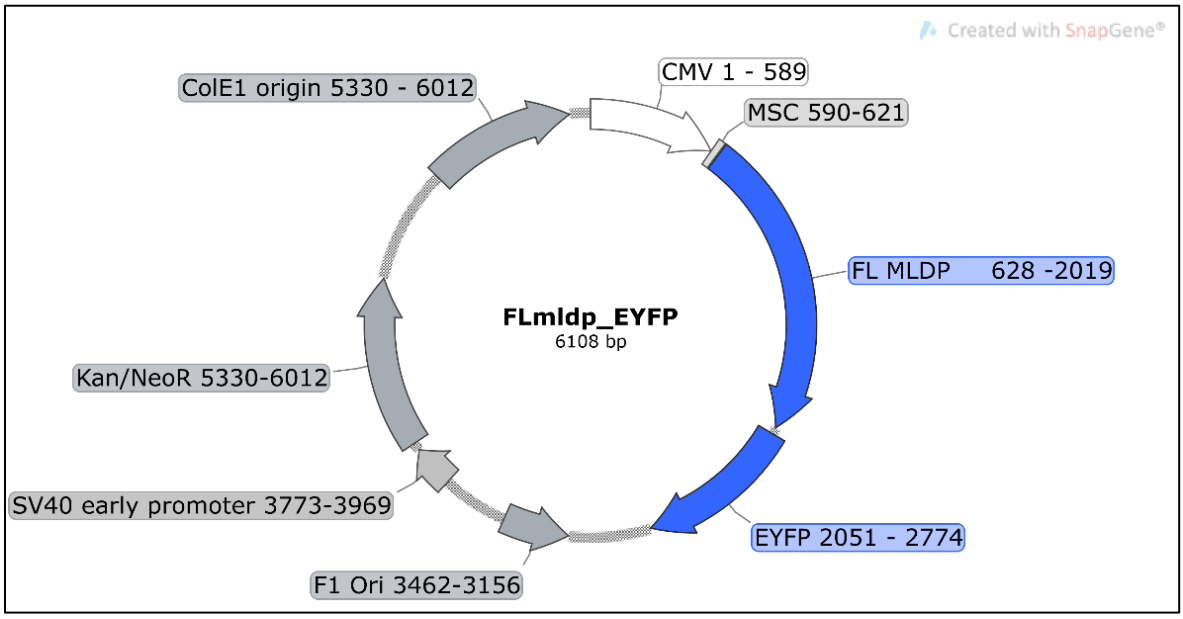

Figure 28: ***Plasmid map provided by Dr. Granneman (Wayne State University School of Medicine, Detroit) for the EYFP-plasmid containing the Perilipin-5-EYFP construct (FLmldp_EYFP).*** *Since only a paper copy of the plasmid map was delivered, the map was recreated with SnapGene®Viewer 4.1.9.*

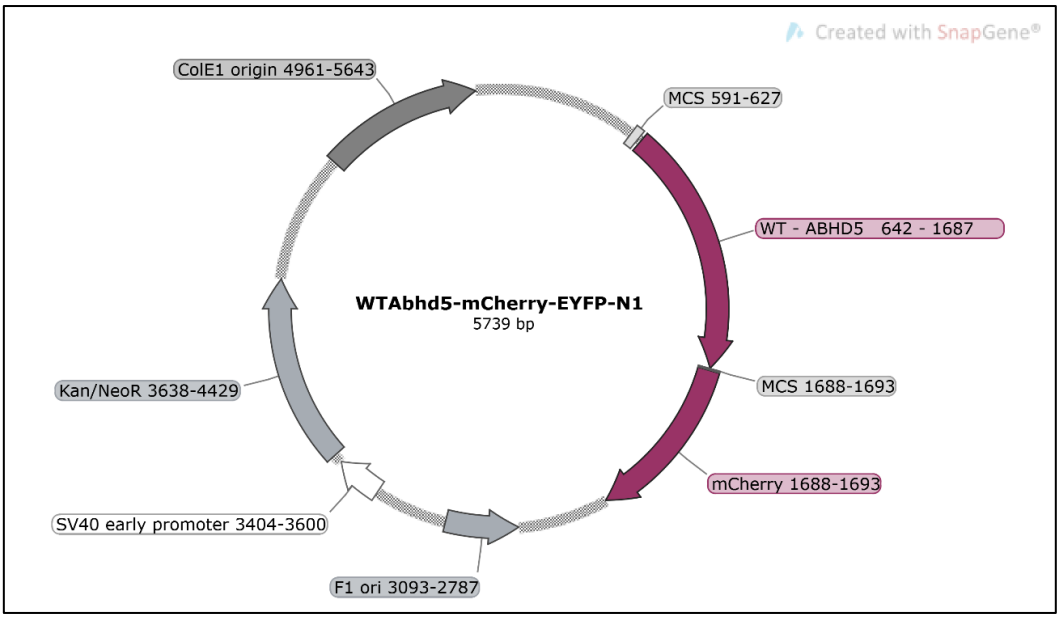

Figure 29: ***Plasmid map provided by Dr. Granneman (Wayne State University School of Medicine, Detroit) for an EYFP-N1 plasmid containing the wild-type ABHD5-mCherry (=CGI-58-mCherry) gene.*** *Since only a paper copy of the plasmid map was delivered, the map was recreated with SnapGene®Viewer 4.1.9.*

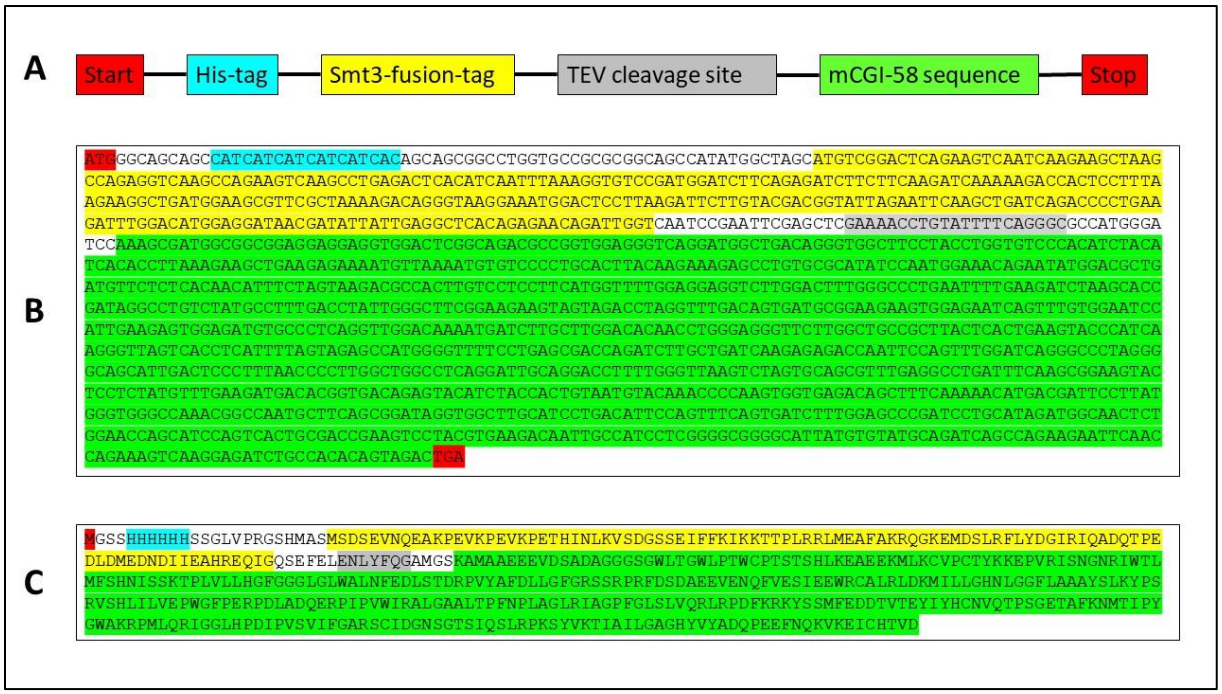

Figure 30: ***Sequence of mCGI-58 construct containing an N-terminal smt3 fusion tag, a 6XHIS-tag and a tobacco etch virus (TEV) protease cleavage site provided by Dr. M. Oberer (Karl-Franzens University Graz) A*** *Basic protein structure of CGI-58 construct* ***B*** *Nucleic acid sequence of CGI-58 construct Amino acid sequence of CGI-58 construct* ***A*** *plasmid map and further information can be found in the dissertation of Andras Boeszoermenyi titled "Structural Characterization of CGI-58 Interactions" (2014).*

Mus musculus perilipin 1 (Plin1)

NCBI Reference Sequence: NM_175640.2

DNA Sequence

ATGTCAATGAACAAGGGCCCAACCCTGCTGGATGGAGACCTCCCTGAGCAGGAGAACGTGCTCCAGAGAGTTCTG
CAGCTGCCTGTGGTGAGCGGGACCTGTGAGTGCTTCCAGAAGACCTACAACAGCACCAAAGAAGCCCACCCCCTG
GTGGCCTCTGTGTGCAATGCCTATGAGAAGGGTGTACAGGGTGCCAGCAACCTGGCTGCCTGGAGCATGGAGCCG
GTGGTCCGTCGGCTGTCCACCCAGTTCACAGCTGCCAATGAGTTGGCCTGCAGAGGCCTGGACCACCTGGAGGAA
AAGATCCCGGCTCTTCAATACCCTCCAGAAAAGATCGCCTCTGAACTGAAGGGCACCATCTCTACCCGCCTTCGA
AGCGCCAGGAACAGCATCAGTGTGCCCATTGCAAGCACCTCTGACAAGGTTCTGGGGGCCACTCTGGCCGGCTGC
GAGCTTGCCTTGGGGATGGCCAAAGAGACAGCAGAATATGCCGCCAACACCCGGGTTGGCCGACTGGCCTCTGGA
GGGGCTGATCTGGCTCTGGGAAGCATCGAGAAGGTGGTAGAGTTCCTCCTGCCACCAGACAAGGAGTCAGCCCCT
TCTTCCGGACGGCAGAGGACCCAGAAGGCTCCCAAGGCCAAACCAAGCCTTGTGAGGAGGGTCAGCACCCTGGCC
AACACTCTTTCTCGACACACCATGCAAACCACAGCATGGGCCCTGAAGCAGGGCCACTCTCTGGCCATGTGGATC
CCGGGTGTGGCACCCCTGAGCAGCCTGGCCCAGTGGGGCGCATCGGCAGCCATGCAGGTGGTGTCCCGGCGGCAG
AGTGAGGTGCGGGTGCCCTGGCTGCACAACCTGGCAGCCTCTCAGGATGAGAGCCATGACGACCAGACAGACACA
GAGGGAGAGGAGACAGACGACGAGGAGGAGGAAGAAGAGTCCGAGGCTGAGGAGAACGTGCTCAGAGAGGTTACA
GCCCTGCCCAACCCGAGAGGCCTCCTGGGTGGTGTGGTACACACCGTGCAGAACACTCTCCGGAACACCATCTCC
GCAGTGACCTGGGCACCTGCGGCTGTGCTGGGCACGGTGGGAAGGATCCTGCACCTCACACCAGCCCAGGCTGTC
TCCTCTACCAAAGGGAGGGCCATGTCCCTATCCGATGCCCTGAAGGGTGTTACGGATAACGTGGTAGACACTGTG
GTACACTATGTGCCGCTTCCCAGGCTGTCCCTGATGGAGCCCGAGAGCGAATTCCGAGACATCGATAACCCTTCA
GCAGAGGCGGAGCGCAAAGGGTCCGGGGCGCGGCCCGCCAGCCCGGAGTCCACCCCGCGCCCGGGCCAGCCCCGC
GGCAGCTTGCGCAGCGTGCGGGGTCTCAGCGCGCCCTCCTGCCCCGGCCTGGACGACAAAACCGAGGCGTCAGCG
CGTCCCGGCTTCCTGGCTATGCCCAGAGAGAAGCCTGCGCGCAGAGTCAGCGACAGCTTCTTCCGGCCCAGCGTC
ATGGAGCCCATCCTGGGCCGCGCGCAGTACAGCCAGCTGCGCAAGAAGAGCTGA

Amino Acid Sequence

MSMNKGPTLLDGDLPEQENVLQRVLQLPVVSGTCECFQKTYNSTKEAHPLVASVCNAYEKGVQGASNLAAWSMEP
VVRRLSTQFTAANELACRGLDHLEEKIPALQYPPEKIASELKGTISTRLRSARNSISVPIASTSDKVLGATLAGC
ELALGMAKETAEYAANTRVGRLASGGADLALGSIEKVVEFLLPPDKESAPSSGRQRTQKAPKAKPSLVRRVSTLA
NTLSRHTMQTTAWALKQGHSLAMWIPGVAPLSSLAQWGASAAMQVVSRRQSEVRVPWLHNLAASQDESHDDQTDT
EGEETDDEEEEEESEAEENVLREVTALPNPRGLLGGVVHTVQNTLRNTISAVTWAPAAVLGTVGRILHLTPAQAV
SSTKGRAMSLSDALKGVTDNVVDTVVHYVPLPRLSLMEPESEFRDIDNPSAEAERKGSGARPASPESTPRPGQPR
GSLRSVRGLSAPSCPGLDDKTEASARPGFLAMPREKPARRVSDSFFRPSVMEPILGRAQYSQLRKKS"

Figure 31: ***DNA/amino acid sequence of murine wild-type perilipin 1 obtained from the NCBI database*** *(reference sequence number can be found in the second line)*

Mus musculus perilipin 5 (Plin5)

NCBI Reference Sequence: NM_025874.3

DNA Sequence

```
ATGGACCAGAGAGGTGAAGACACCACCCTAGCGCCACACAGCAGAATGTCCGGTGATCAGACAGCTCAGGACCCT
GGATCCAGCCTGGGAGAACTGGACCAGCAGAATGTGGTGAATCGAGTGGTGGCTTTGCCCCTGGTCAAGGCCACG
TGCACTGCCGTGTCCAGTGCTTACAACTCGGCCAAGGACAGGCACCCGCTGCTGGGCTCCGCCTGCCGCCTTGCT
GAGCACTGTGTGTGTAGTGTGACTACCTGTGCCCTGGACCACGCACAGCCACTGCTGGAGCACCTGCAGCCCCAG
TTGGCCACAGTGAATGATCTTGCCTGCAGGGGACTAGACAAATTGGAAGAGAAGCTGCCCTTCCTGCAGCAGCCA
TCAGACATGGTGGTGACATCAGCCAAGGATACAGTGGCCAAAAGTGTCACAGGCATGGTGGACCTGGCCCAAAGG
GGCCGGCGTTGGAGTGGGGAGCTGAGGCGCTCCATGAGTCAAGCCATGGACATGGTGCTGGGCAAGTCGGAGAAG
CTGGTGGACCGCTTCCTGCCCATGACTGAGGCTGAGCTAGCAGTCCTGGCAGCTGAGGCCGAGGGCCCAGAAGTG
GGCACAGTGGAGGAGCAGAGGCAGCAACAGGGCTACTTTGTGCGTCTGGGGTCCCTATCGGCACGCCTCCGCCAT
CTCGCCTATGAACACTCTTTGGGGAAACTGAGGCAGAGCAAACACCGTACCCAGGAGATGCTGGCCCAGCTGCAG
GAAACGCTGGAGCTGATCCAGCATATGCAGAGAGGGGCAAGCCCTAGCCCTACTTTCCATCCCCCAAAGACTCAG
GAGCTGTGGGGGAGCTGGAGCCCGTGTCTAGAGAATGGCCGCAGCCACAGTGAGGTGGAGCTGGAGACACTGGCT
CTGTCTCGAAGTTTGACCCTGGAGCTGCAGAATGCAGTGGATGCCCTGGCAGGCTGTGTTCGGGGCCTGCCACCT
AGTGCCCAGGCCAAGGTGGCTGAGGTGCAGCGCAGCGTGGATGCTCTACAGGCCACCTTTGCTGATGCACACTGC
CTTGGTGATGTGGCACCCACTGCTCTGGCTGAGGGCCGGGGCAGTGTGGCCCGGGCACATGCCTGTGTGGATGAG
TTCCTGGATTTGGTCCTGCGGGCCATGCCACTGCCCTGGCTTGTGGGGCCCTTTGCACCCATCCTGGTGGAACAG
TCGGAGCCCCTGATCAACCTGGCCACCTGTGTGGACGAGGTGGTGGGTGACCCTGATCCTCGCTGGGCACACATG
GACTGGCCAGCCCAGAAGAGGGCCTGGGAGGCTGAGTCTGCAGATCCTGGGGGGCAAGAGGCTGAGCCCCCAAGG
GGGCAAGGCAAGCACACAATGATGCCAGAGCTGGACTTCTGA
```

Amino Acid Sequence

```
MDQRGEDTTLAPHSRMSGDQTAQDPGSSLGELDQQNVVNRVVALPLVKATCTAVSSAYNSAKDRHPLLGSACRLA
EHCVCSVTTCALDHAQPLLEHLQPQLATVNDLACRGLDKLEEKLPFLQQPSDMVVTSAKDTVAKSVTGMVDLAQR
GRRWSGELRRSMSQAMDMVLGKSEKLVDRFLPMTEAELAVLAAEAEGPEVGTVEEQRQQQGYFVRLGSLSARLRH
LAYEHSLGKLRQSKHRTQEMLAQLQETLELIQHMQRGASPSPTFHPPKTQELWGSWSPCLENGRSHSEVELETLA
LSRSLTLELQNAVDALAGCVRGLPPSAQAKVAEVQRSVDALQATFADAHCLGDVAPTALAEGRGSVARAHACVDE
FLDLVLRAMPLPWLVGPFAPILVEQSEPLINLATCVDEVVGDPDPRWAHMDWPAQKRAWEAESADPGGQEAEPPR
GQGKHTMMPELDF
```

Figure 32: ***DNA/amino acid sequence of murine wild-type perilipin 5 obtained from the NCBI database*** *(reference sequence number can be found in the second line)*

Mus musculus patatin-like phospholipase domain containing 2 (Pnpla2/ATGL)

NCBI Reference Sequence: NM_001163689.1

DNA Sequence

```
ATGTTCCCGAGGGAGACCAAGTGGAACATCTCATTCGCTGGCTGCGGCTTCCTCGGGGTCTACCACATTGGCGTG
GCCTCCTGCCTCCGTGAGCACGCGCCCTTCCTGGTGGCCAACGCCACTCACATCTACGGAGCCTCGGCAGGGGCG
CTCACCGCCACAGCGCTGGTCACTGGGGCCTGCCTGGGTGAAGCAGGTGCCAACATTATTGAGGTGTCCAAGGAG
GCCCGGAAGCGGTTCCTGGGTCCTCTGCATCCCTCCTTCAACCTGGTGAAGACCATCCGTGGCTGTCTACTAAAG
ACCCTGCCTGCTGATTGCCATGAGCGCGCCAATGGACGCCTGGGCATCTCCCTGACTCGTGTTTCAGACGGAGAG
AACGTCATCATATCCCACTTTAGCTCCAAGGATGAGCTCATCCAGGCCAATGTCTGCAGCACATTTATCCCGGTG
TACTGTGGCCTCATTCCTCCTACCCTCCAAGGGGTGCGCTATGTGGATGGCGGCATTTCAGACAACTTGCCACTT
TATGAGCTGAAGAATACCATCACAGTGTCCCCATTCTCAGGCGAGAGTGACATCTGCCCTCAGGACAGCTCCACC
AACATCCACGAGCTTCGCGTCACCAACACCAGCATCCAGTTCAACCTTCGCAATCTCTACCGCCTCTCGAAGGCT
CTCTTCCCGCCAGAGCCCATGGTCCTCCGAGAGATGTGCAAACAGGGCTACAGAGATGGACTTCGATTCCTTAGG
AGGAATGGCCTACTGAACCAACCCAACCCTTTGCTGGCACTGCCCCCAGTTGTCCCCCAGGAAGAGGATGCAGAG
GAAGCTGCTGTGGTGGAGGAGAGGGCTGGAGAGGAGGATCAATTGCAGCCTTATAGAAAAGATCGAATTCTAGAG
CACCTGCCTGCCAGACTCAATGAGGCCCTGCTGGAGGCCTGTGTGGAACCAAAGGACCTGATGACCACCCTTTCC
AACATGCTACCAGTGCGCCTGGCAACGGCCATGATGGTGCCCTATACTCTGCCGCTGGAGAGTGCAGTGTCCTTC
ACCATCCGCTTGTTGGAGTGGCTGCCTGATGTCCCTGAAGATATCCGGTGGATGAAAGAGCAGACGGGTAGCATC
TGCCAGTATCTGGTGATGAGGGCCAAGAGGAAATTGGGTGACCATCTGCCTTCCAGACTGTCTGAGCAGGTGGAA
CTGCGACGTGCCCAGTCTCTGCCCTCTGTGCCACTGTCTTGCGCCACCTACAGTGAGGCCCTACCCAACTGGGTA
CGAAACAACCTCTCACTGGGGGACGCGCTGGCCAAGTGGGAAGAATGCCAGCGTCAGCTACTGCTGGGTCTCTTC
TGCACCAATGTGGCCTTCCCGCCGGATGCCTTGCGCATGCGCGCACCTGCCAGCCCCACTGCCGCAGATCCTGCC
ACCCCACAGGATCCACCTGGCCTCCCGCCTTGCTGA
```

Amino Acid Sequence

```
MFPRETKWNISFAGCGFLGVYHIGVASCLREHAPFLVANATHIYGASAGALTATALVTGACLGEAGANIIEVSKE
ARKRFLGPLHPSFNLVKTIRGCLLKTLPADCHERANGRLGISLTRVSDGENVIISHFSSKDELIQANVCSTFIPV
YCGLIPPTLQGVRYVDGGISDNLPLYELKNTITVSPFSGESDICPQDSSTNIHELRVTNTSIQFNLRNLYRLSKA
LFPPEPMVLREMCKQGYRDGLRFLRRNGLLNQPNPLLALPPVVPQEEDAEEAAVVEERAGEEDQLQPYRKDRILE
HLPARLNEALLEACVEPKDLMTTLSNMLPVRLATAMMVPYTLPLESAVSFTIRLLEWLPDVPEDIRWMKEQTGSI
CQYLVMRAKRKLGDHLPSRLSEQVELRRAQSLPSVPLSCATYSEALPNWVRNNLSLGDALAKWEECQRQLLLGLF
CTNVAFPPDALRMRAPASPTAADPATPQDPPGLPPC
```

Figure 33: ***DNA/amino acid sequence of murine wild-type ATGL obtained from the NCBI database*** *(reference sequence number can be found in the second line)*

Mus musculus abhydrolase domain containing 5 (Abhd5/CGI-58)

NCBI Reference Sequence: NM_026179.2

DNA Sequence

```
ATGAAAGCGATGGCGGCGGAGGAGGAGGTGGACTCGGCAGACGCCGGTGGAGGGTCAGGATGGCTGACAGGGTGG
CTTCCTACCTGGTGTCCCACATCTACATCACACCTTAAAGAAGCTGAAGAGAAAATGTTAAAATGTGTCCCCTGC
ACTTACAAGAAAGAGCCTGTGCGCATATCCAATGGAAACAGAATATGGACGCTGATGTTCTCTCACAACATTTCT
AGTAAGACGCCACTTGTCCTCCTTCATGGTTTTGGAGGAGGTCTTGGACTTTGGGCCCTGAATTTTGAAGATCTA
AGCACCGATAGGCCTGTCTATGCCTTTGACCTATTGGGCTTCGGAAGAAGTAGTAGACCTAGGTTTGACAGTGAT
GCGGAAGAAGTGGAGAATCAGTTTGTGGAATCCATTGAAGAGTGGAGATGTGCCCTCAGGTTGGACAAAATGATC
TTGCTTGGACACAACCTGGGAGGGTTCTTGGCTGCCGCTTACTCACTGAAGTACCCATCAAGGGTTAGTCACCTC
ATTTTAGTAGAGCCATGGGGTTTTCCTGAGCGACCAGATCTTGCTGATCAAGAGAGACCAATTCCAGTTTGGATC
AGGGCCCTAGGGGCAGCATTGACTCCCTTTAACCCCTTGGCTGGCCTCAGGATTGCAGGACCTTTTGGGTTAAGT
CTAGTGCAGCGTTTGAGGCCTGATTTCAAGCGGAAGTACTCCTCTATGTTTGAAGATGACACGGTGACAGAGTAC
ATCTACCACTGTAATGTACAAACCCCAAGTGGTGAGACAGCTTTCAAAAACATGACGATTCCTTATGGGTGGGCC
AAACGGCCAATGCTTCAGCGGATAGGTGGCTTGCATCCTGACATTCCAGTTTCAGTGATCTTTGGAGCCCGATCC
TGCATAGATGGCAACTCTGGAACCAGCATCCAGTCACTGCGACCGAAGTCCTACGTGAAGACAATTGCCATCCTC
GGGGCGGGGCATTATGTGTATGCAGATCAGCCAGAAGAATTCAACCAGAAAGTCAAGGAGATCTGCCACACAGTA
GACTGA
```

Amino Acid Sequence

```
MKAMAAEEEVDSADAGGGSGWLTGWLPTWCPTSTSHLKEAEEKMLKCVPCTYKKEPVRISNGNRIWTLMFSHNIS
SKTPLVLLHGFGGGLGLWALNFEDLSTDRPVYAFDLLGFGRSSRPRFDSDAEEVENQFVESIEEWRCALRLDKMI
LLGHNLGGFLAAAYSLKYPSRVSHLILVEPWGFPERPDLADQERPIPVWIRALGAALTPFNPLAGLRIAGPFGLS
LVQRLRPDFKRKYSSMFEDDTVTEYIYHCNVQTPSGETAFKNMTIPYGWAKRPMLQRIGGLHPDIPVSVIFGARS
CIDGNSGTSIQSLRPKSYVKTIAILGAGHYVYADQPEEFNQKVKEICHTVD"
```

Figure 34: ***DNA/amino acid sequence of murine wild-type CGI-58 obtained from the NCBI database*** *(reference sequence number can be found in the second line)*

Homo sapiens abhydrolase domain containing 5 (ABHD5; CGI-58)

NCBI Reference Sequence: NM_016006.5

DNA Sequence

```
ATGGCGGCGGAGGAGGAGGAGGTGGACTCTGCCGACACCGGAGAGAGGTCAGGATGGCTAACTGGTTGGCTCCCC
ACATGGTGCCCTACGTCTATATCACACCTTAAAGAAGCTGAAGAGAAGATGTTAAAATGTGTGCCTTGCACATAC
AAAAAAGAACCTGTTCGTATATCTAATGGAAATAAAATATGGACACTGAAGTTCTCTCATAATATTTCAAATAAG
ACTCCACTTGTCCTTCTCCATGGTTTTGGAGGAGGTCTTGGGCTCTGGGCACTGAATTTTGGAGATCTTTGCACC
AACAGACCTGTCTATGCTTTTGACCTATTGGGTTTTGGACGAAGTAGTAGACCCAGGTTTGACAGTGATGCAGAA
GAAGTGGAGAATCAGTTTGTGGAATCCATTGAAGAGTGGAGATGTGCCCTAGGATTGGACAAAATGATCTTGCTT
GGGCACAACCTAGGTGGATTCTTGGCTGCTGCTTACTCGCTGAAGTACCCATCAAGGGTTAATCATCTCATTTTA
GTGGAGCCTTGGGGTTTCCCTGAACGACCAGACCTTGCTGATCAAGACAGACCAATTCCAGTTTGGATCAGAGCC
TTGGGAGCAGCATTGACTCCCTTTAACCCTTTAGCTGGCCTAAGGATTGCAGGACCCTTTGGTTTAAGTCTAGTG
CAGCGTTTAAGGCCTGATTTCAAACGAAAGTATTCTTCAATGTTCGAAGACGATACTGTGACAGAATACATCTAC
CACTGTAATGTGCAGACTCCAAGTGGTGAGACAGCTTTCAAGAATATGACTATTCCTTATGGATGGGCAAAAAGG
CCAATGCTCCAGCGAATTGGTAAAATGCACCCTGACATTCCAGTTTCAGTGATCTTTGGCGCCCGATCCTGCATA
GATGGCAATTCTGGCACCAGCATCCAGTCCTTACGACCACATTCATATGTGAAGACAATAGCTATTCTTGGGGCA
GGACATTATGTATATGCAGATCAACCAGAAGAATTCAACCAGAAAGTAAAGGAGATCTGCGACACTGTGGACTGA
```

Amino Acid Sequence

```
MAAEEEEVDSADTGERSGWLTGWLPTWCPTSISHLKEAEEKMLKCVPCTYKKEPVRISNGNKIWTLKFSHNISNK
TPLVLLHGFGGGLGLWALNFGDLCTNRPVYAFDLLGFGRSSRPRFDSDAEEVENQFVESIEEWRCALGLDKMILL
GHNLGGFLAAAYSLKYPSRVNHLILVEPWGFPERPDLADQDRPIPVWIRALGAALTPFNPLAGLRIAGPFGLSLV
QRLRPDFKRKYSSMFEDDTVTEYIYHCNVQTPSGETAFKNMTIPYGWAKRPMLQRIGKMHPDIPVSVIFGARSCI
DGNSGTSIQSLRPHSYVKTIAILGAGHYVYADQPEEFNQKVKEICDTVD"
```

Figure 35: ***DNA/amino acid sequence of human wild-type CG-58 obtained from the NCBI database*** *(reference sequence number can be found in the second line)*

Mus musculus G0/G1 switch gene 2 (G0s2)

NCBI Reference Sequence: NM_008059.3

DNA Sequence

```
ATGGAAAGTGTGCAGGAGCTGATCCCTCTGGCCAAGGAGATGATGGCGCAGAAGCCCCGAGGGAAGCTAGTGAAG
CTATACGTGCTGGGCAGTGTGCTGGCGCTCTTCGGTGTGGTGCTCGGCCTAGTTGAGACGGTGTGCAGCCCTTTC
ACAGCCGCCAGCCGTCTGCGCGACCAAGAGGCTGCAGTGGTGGAGCTGCGGGAAGCGTGTGAACAGCAGTCCCTC
CACAAGCAGGCCCTGCTGGCAGGAGGCAAGGCACAGGAGGCGACCCTGTGCAGCCGGGCCCTGTCCCTCCGGCAG
CACGCCTCTTAA
```

Amino Acid Sequence

```
MESVQELIPLAKEMMAQKPRGKLVKLYVLGSVLALFGVVLGLVETVCSPFTAASRLRDQEAAVVELREACEQQSL
HKQALLAGGKAQEATLCSRALSLRQHAS
```

*Figure 36: **DNA/amino acid sequence of murine G0S2 obtained from the NCBI database** (reference sequence number can be found in the second line)*

Homo sapiens G0/G1 switch 2 (G0S2)

NCBI Reference Sequence: NM_015714.3

DNA Sequence

```
ATGGAAACGGTCCAGGAGCTGATCCCCCTGGCCAAGGAGATGATGGCCCAGAAGCGCAAGGGGAAGATGGTGAAG
CTGTACGTGCTGGGCAGCGTGCTGGCCCTCTTCGGCGTGGTGCTCGGCCTGATGGAGACTGTGTGCAGCCCCTTC
ACGGCCGCCAGACGTCTGCGGGACCAGGAGGCAGCCGTGGCGGAGCTGCAGGCCGCCCTGGAGCGACAGGCTCTC
CAGAAGCAAGCCCTGCAGGAGAAAGGCAAGCAGCAGGACACGGTCCTCGGCGGCCGGGCCCTGTCCAACCGGCAG
CACGCCTCCTAG
```

Amino Acid Sequence

```
METVQELIPLAKEMMAQKRKGKMVKLYVLGSVLALFGVVLGLMETVCSPFTAARRLRDQEAAVAELQAALERQAL
QKQALQEKGKQQDTVLGGRALSNRQHAS
```

*Figure 37: **DNA/amino acid sequence of human G0S2 obtained from the NCBI database** (reference sequence number can be found in the second line)*

Sequencing Results

Explanations for any markings in sequencing results are explained by legends in Figure 5 and Figure 7 in Part I of the thesis.

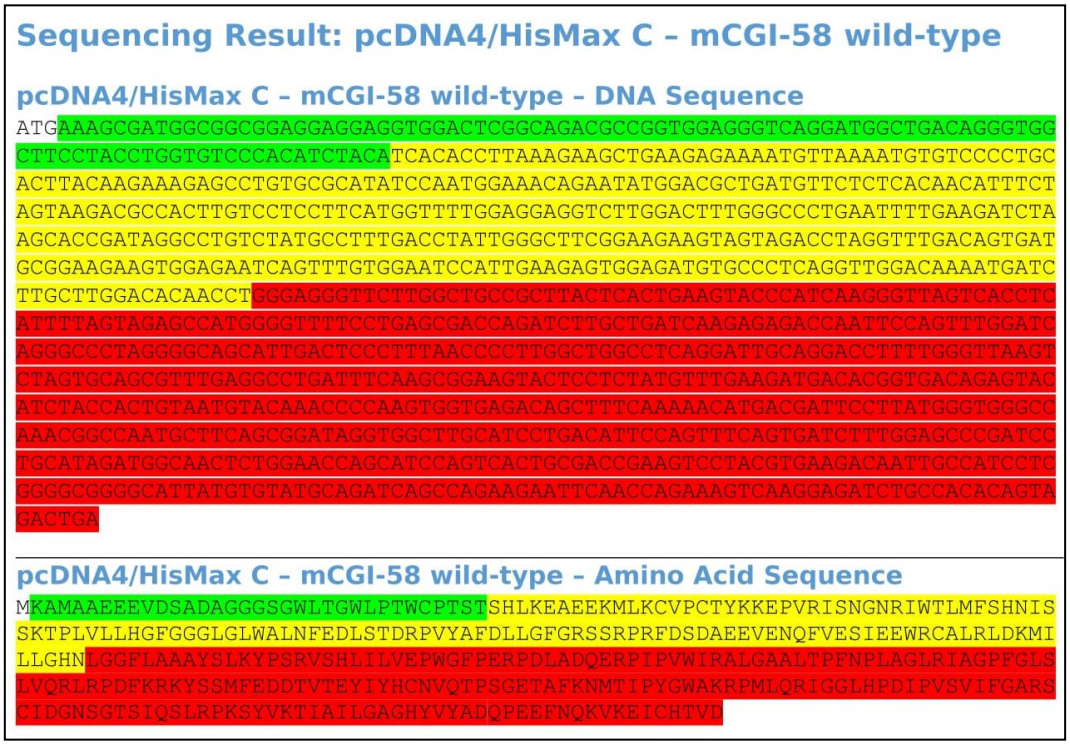

Figure 38: ***Sequencing result of murine CGI-58 wild-type cloned in vector pcDNA4/HisMax C.*** *The upper part shows the DNA sequencing result. The lower part shows the translated amino acid sequence.*

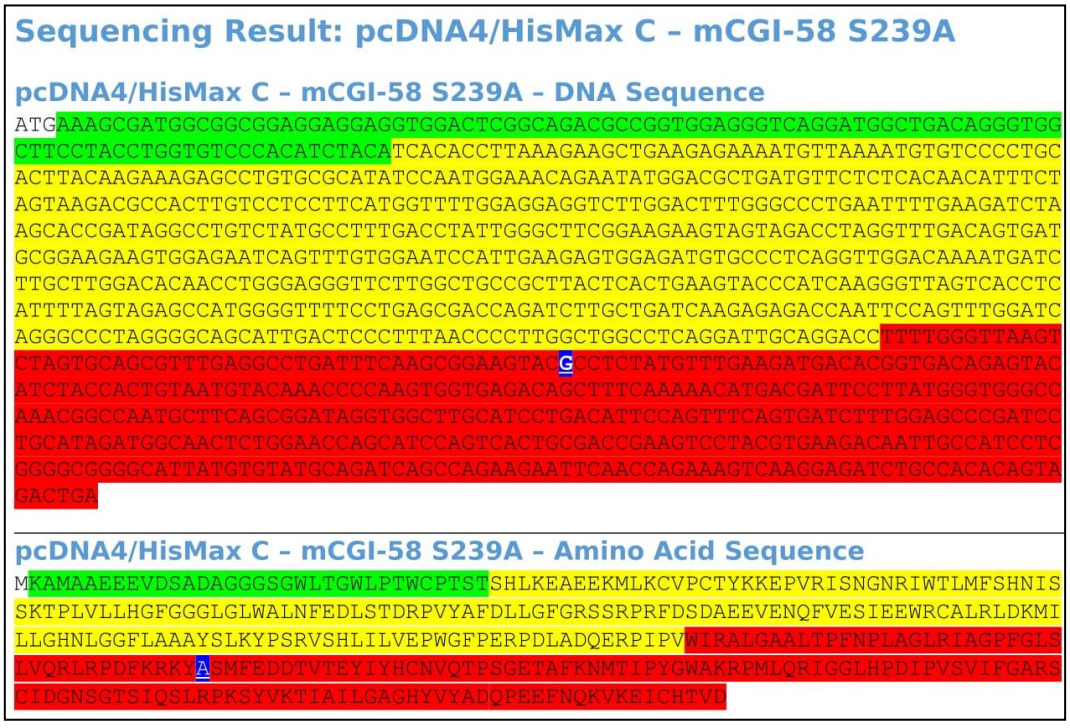

Figure 39: ***Sequencing result of murine CGI-58 S239A cloned in vector pcDNA4/HisMax C.*** *The upper part shows the DNA sequencing result. The lower part shows the translated amino acid sequence.*

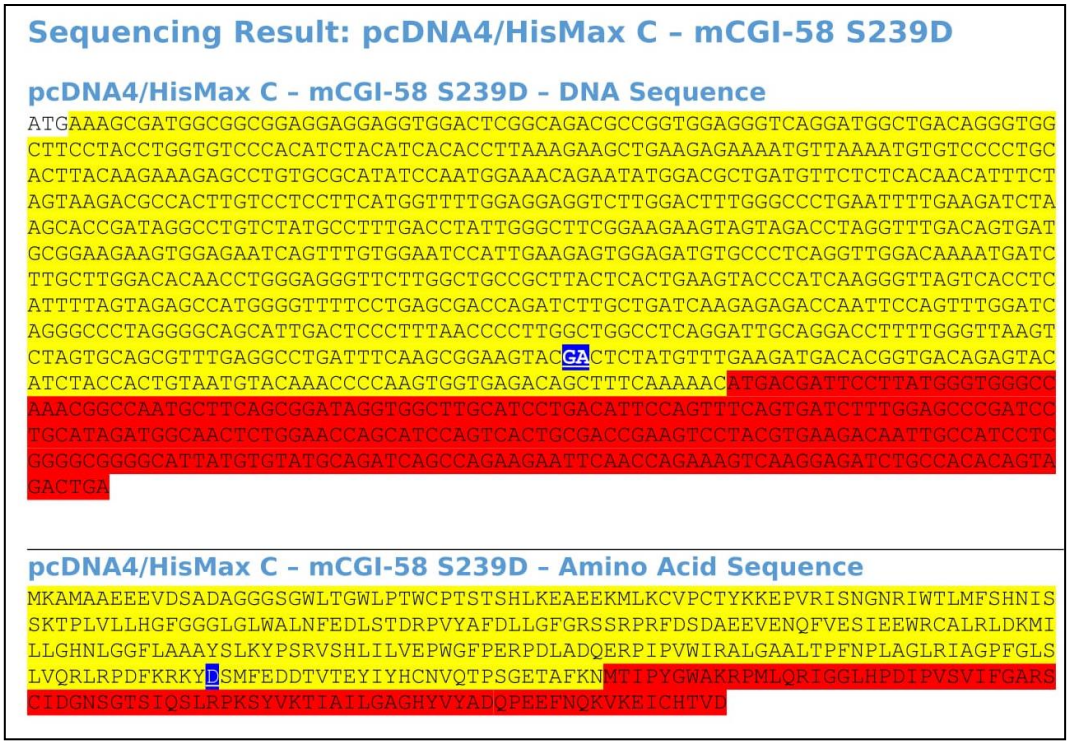

Figure 40: ***Sequencing result of murine CGI-58 S239D cloned in vector pcDNA4/HisMax C****. The upper part shows the DNA sequencing result. The lower part shows the translated amino acid sequence.*

Figure 41: ***Sequencing result of murine CGI-58 Y330F cloned in vector pcDNA4/HisMax C.*** *The upper part shows the DNA sequencing result. The lower part shows the translated amino acid sequence.*

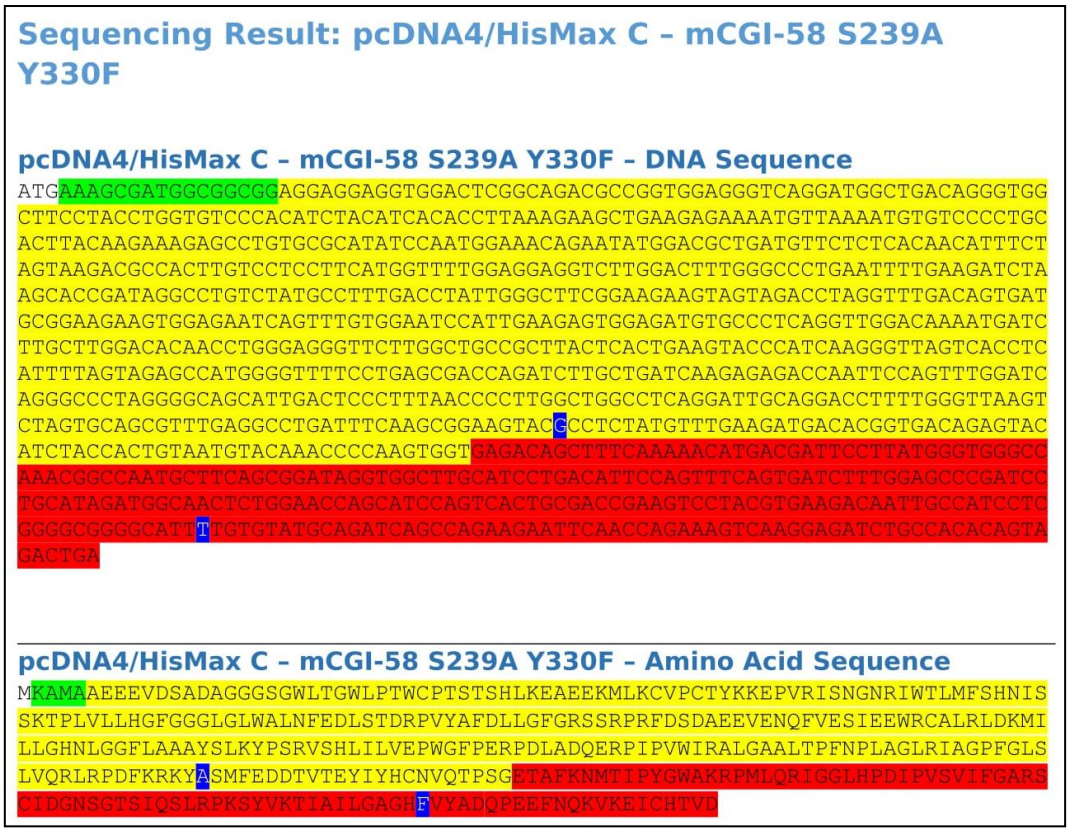

Figure 42: ***Sequencing result of murine CGI-58 S239A Y330F cloned in vector pcDNA4/HisMax C****. The upper part shows the DNA sequencing result. The lower part shows the translated amino acid sequence.*

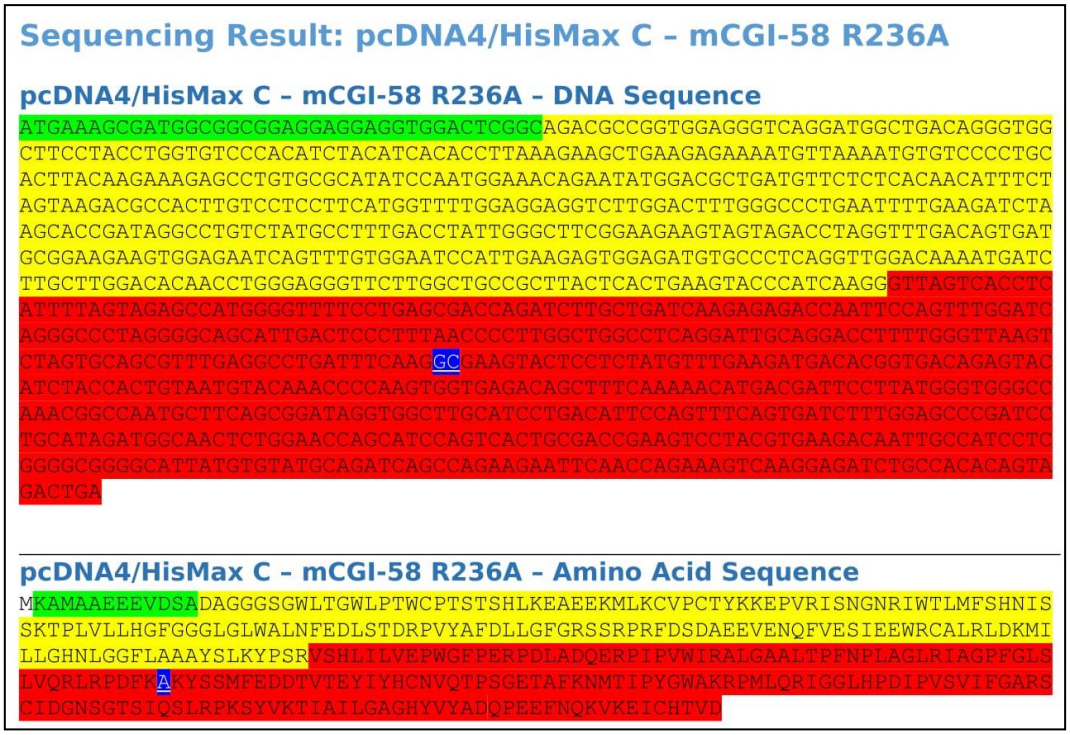

Figure 43: ***Sequencing result of murine CGI-58 R236A cloned in vector pcDNA4/HisMax C.*** *The upper part shows the DNA sequencing result. The lower part shows the translated amino acid sequence.*

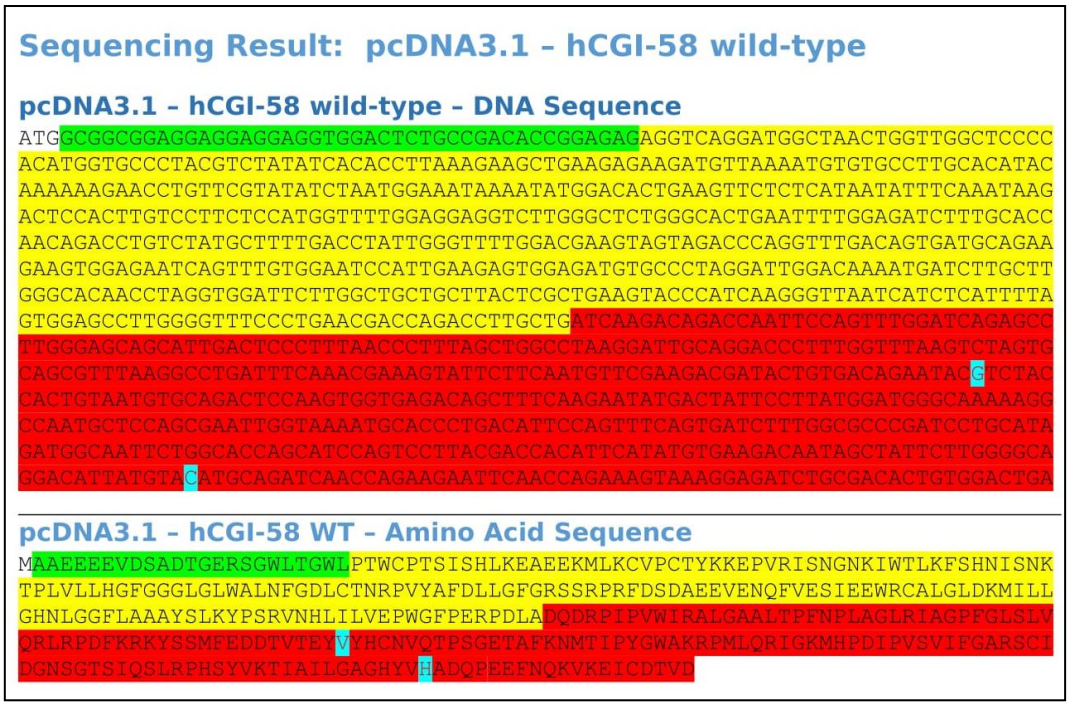

Figure 44: ***Sequencing result of human CGI-58 wild-type cloned in vector pcDNA3.1.*** *The upper part shows the DNA sequencing result. The lower part shows the translated amino acid sequence.*

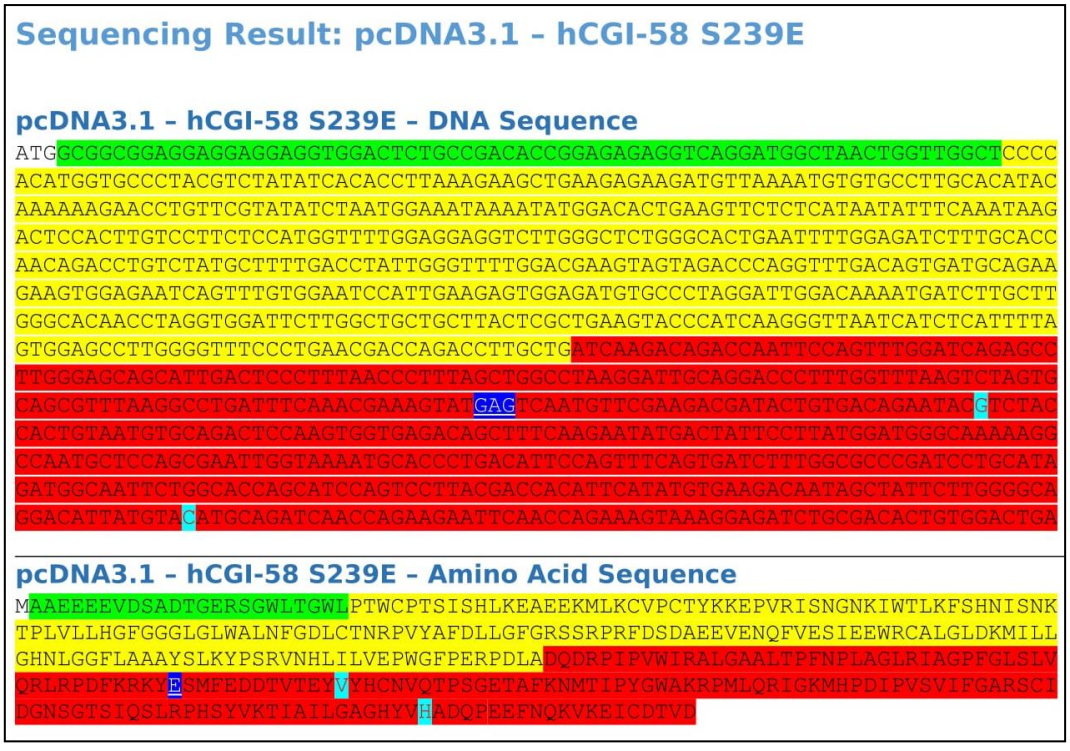

Figure 45: ***Sequencing result of human CGI-58 S239E cloned in vector pcDNA3.1.*** *The upper part shows the DNA sequencing result. The lower part shows the translated amino acid sequence.*

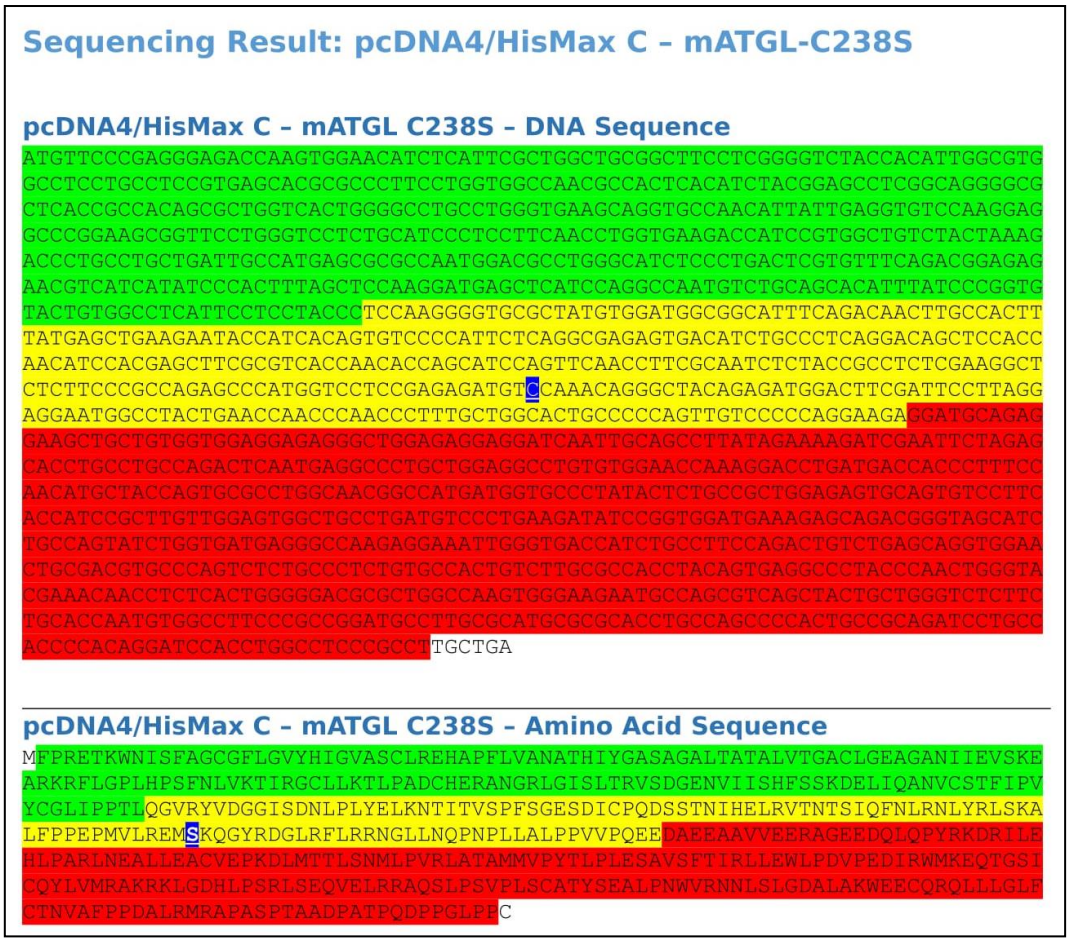

Figure 46: ***Sequencing result of murine ATGL C238S cloned in vector pcDNA4/HisMaxC.*** *The upper part shows the DNA sequencing result. The lower part shows the translated amino acid sequence.*

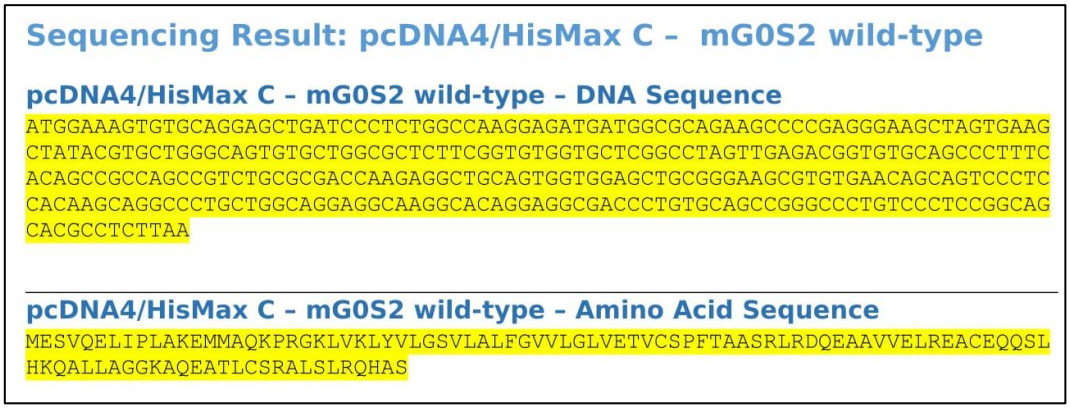

Figure 47: ***Sequencing result of murine G0S2 wild-type cloned in vector pcDNA4/HisMaxC.*** *The upper part shows the DNA sequencing result. The lower part shows the translated amino acid sequence.*

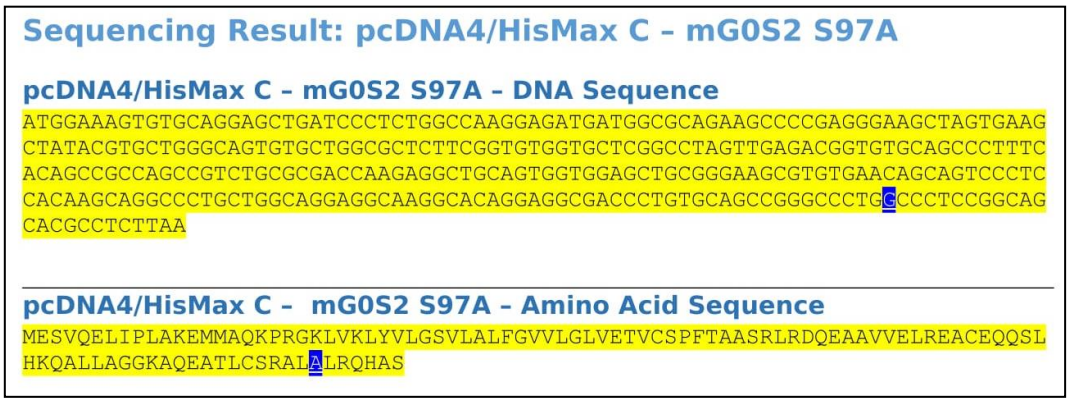

*Figure 48: **Sequencing result of murine G0S2 S97A cloned in vector pcDNA4/HisMaxC**. The upper part shows the DNA sequencing result. The lower part shows the translated amino acid sequence.*

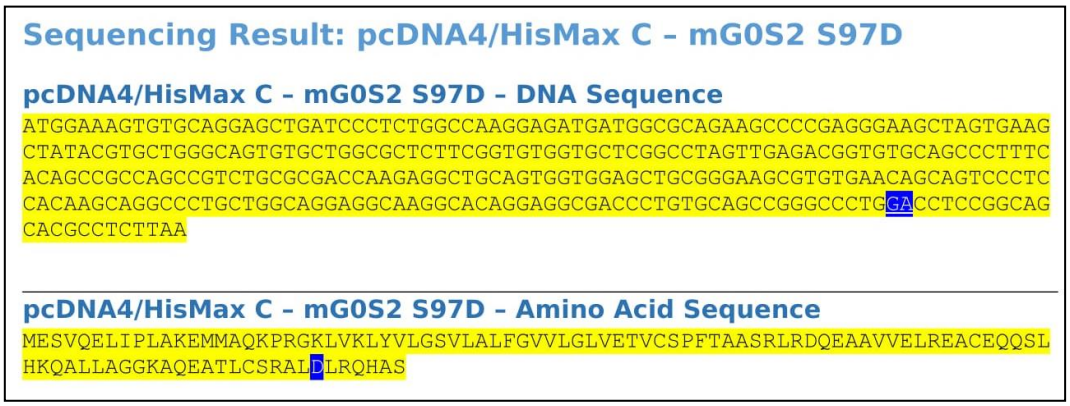

*Figure 49: **Sequencing result of murine G0S2 S97D cloned in vector pcDNA4/HisMaxC**. The upper part shows the DNA sequencing result. The lower part shows the translated amino acid sequence.*

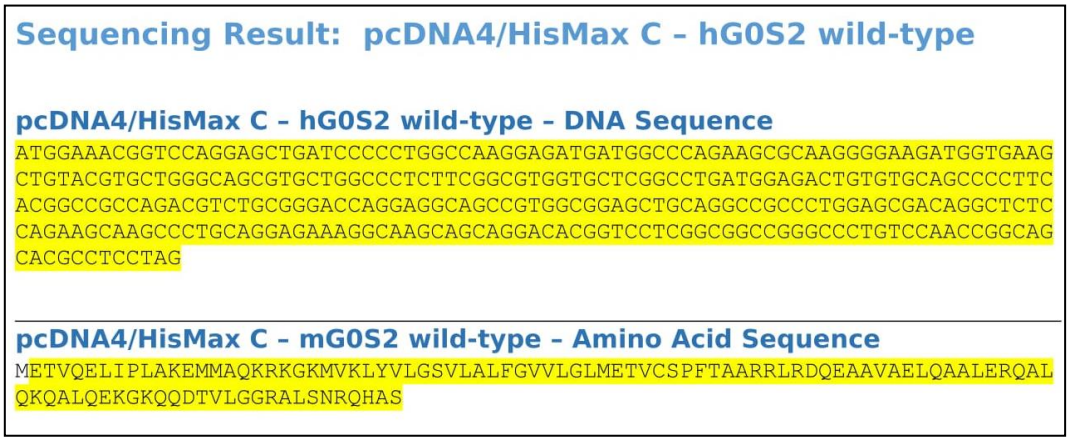

*Figure 50: **Sequencing result of human G0S2 wild-type cloned in vector pcDNA4/HisMaxC.** The upper part shows the DNA sequencing result. The lower part shows the translated amino acid sequence.*

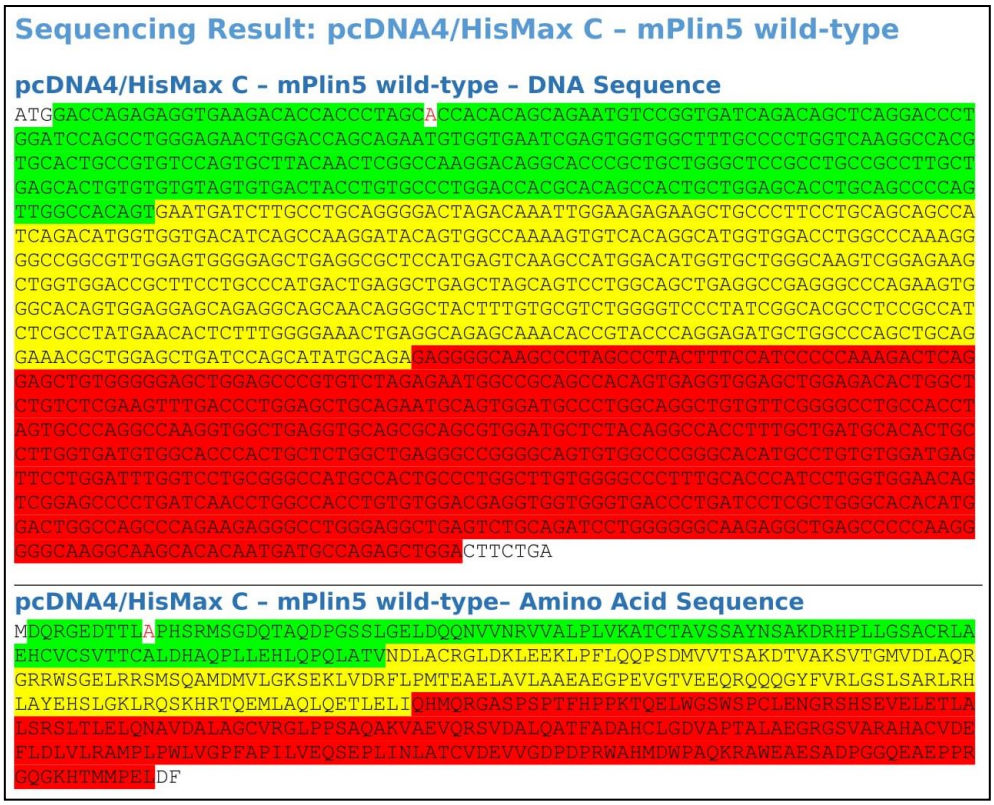

Figure 51: ***Sequencing result of murine Plin5 wild-type cloned in vector pcDNA4/HisMaxC.*** *The upper part shows the DNA sequencing result. The lower part shows the translated amino acid sequence.*

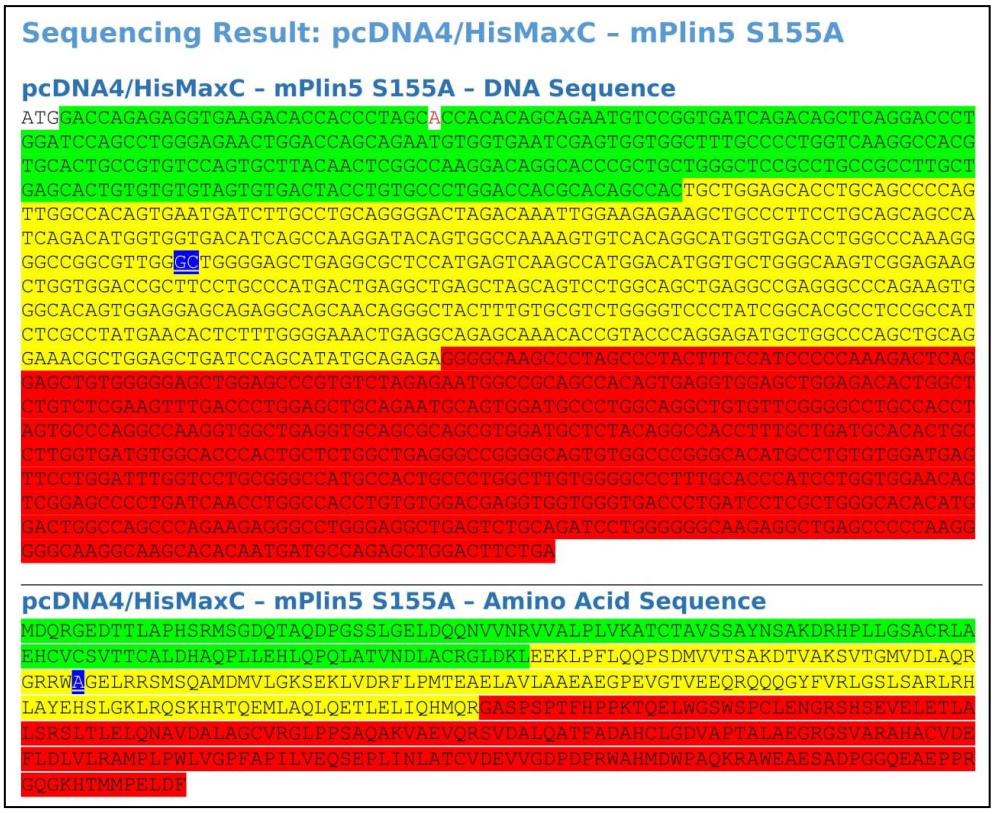

Figure 52: ***Sequencing result of murine Plin5 S155A cloned in vector pcDNA4/HisMaxC.*** *The upper part shows the DNA sequencing result. The lower part shows the translated amino acid sequence.*

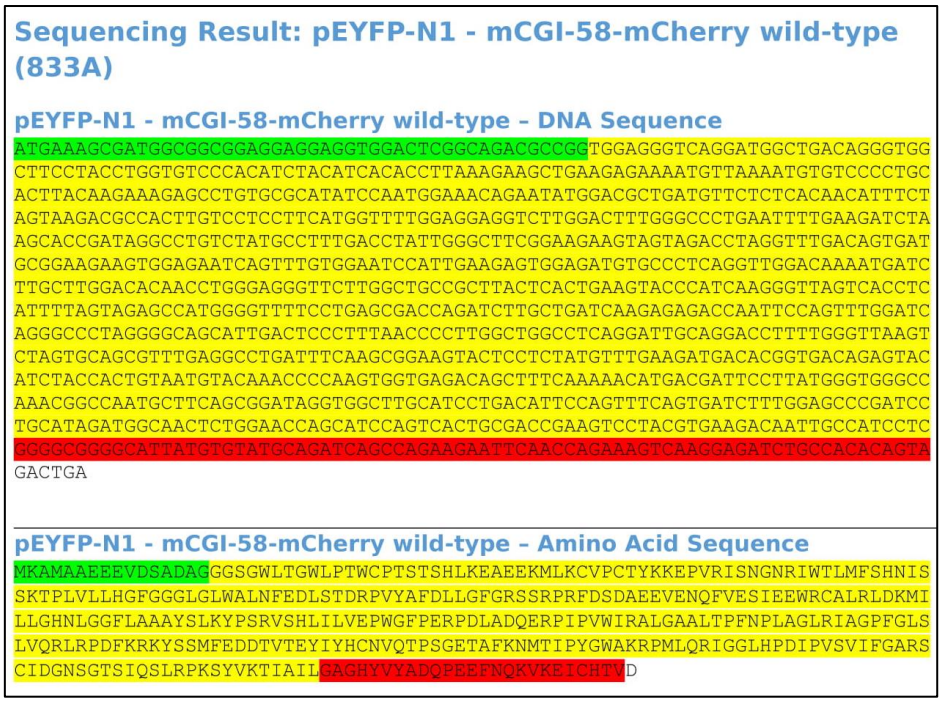

Sequencing Result: pEYFP-N1 - mCGI-58-mCherry wild-type (833A)

pEYFP-N1 - mCGI-58-mCherry wild-type – DNA Sequence

ATGAAAGCGATGGCGGCGGAGGAGGAGGTGGACTCGGCAGACGCCGGTGGAGGGTCAGGATGGCTGACAGGGTGG
CTTCCTACCTGGTGTCCCACATCTACATCACACCTTAAAGAAGCTGAAGAGAAAATGTTAAAATGTGTCCCCTGC
ACTTACAAGAAAGAGCCTGTGCGCATATCCAATGGAAACAGAATATGGACGCTGATGTTCTCTCACAACATTTCT
AGTAAGACGCCACTTGTCCTCCTTCATGGTTTTGGAGGAGGTCTTGGACTTTGGGCCCTGAATTTTGAAGATCTA
AGCACCGATAGGCCTGTCTATGCCTTTGACCTATTGGGCTTCGGAAGAAGTAGTAGACCTAGGTTTGACAGTGAT
GCGGAAGAAGTGGAGAATCAGTTTGTGGAATCCATTGAAGAGTGGAGATGTGCCCTCAGGTTGGACAAAATGATC
TTGCTTGGACACAACCTGGGAGGGTTCTTGGCTGCCGCTTACTCACTGAAGTACCCATCAAGGGTTAGTCACCTC
ATTTTAGTAGAGCCATGGGGTTTTCCTGAGCGACCAGATCTTGCTGATCAAGAGAGACCAATTCCAGTTTGGATC
AGGGCCCTAGGGGCAGCATTGACTCCCTTTAACCCCTTGGCTGGCCTCAGGATTGCAGGACCTTTTGGGTTAAGT
CTAGTGCAGCGTTTGAGGCCTGATTTCAAGCGGAAGTACTCCTCTATGTTTGAAGATGACACGGTGACAGAGTAC
ATCTACCACTGTAATGTACAAACCCCAAGTGGTGAGACAGCTTTCAAAAACATGACGATTCCTTATGGGTGGGCC
AAACGGCCAATGCTTCAGCGGATAGGTGGCTTGCATCCTGACATTCCAGTTTCAGTGATCTTTGGAGCCCGATCC
TGCATAGATGGCAACTCTGGAACCAGCATCCAGTCACTGCGACCGAAGTCCTACGTGAAGACAATTGCCATCCTC
GGGGCGGGGCATTATGTGTATGCAGATCAGCCAGAAGAATTCAACCAGAAAGTCAAGGAGATCTGCCACACAGTA
GACTGA

pEYFP-N1 - mCGI-58-mCherry wild-type – Amino Acid Sequence

MKAMAAEEEVDSADAGGGSGWLTGWLPTWCPTSTSHLKEAEEKMLKCVPCTYKKEPVRISNGNRIWTLMFSHNIS
SKTPLVLLHGFGGGLGLWALNFEDLSTDRPVYAFDLLGFGRSSRPRFDSDAEEVENQFVESIEEWRCALRLDKMI
LLGHNLGGFLAAAYSLKYPSRVSHLILVEPWGFPERPDLADQERPIPVWIRALGAALTPFNPLAGLRIAGPFGLS
LVQRLRPDFKRKYSSMFEDDTVTEYIYHCNVQTPSGETAFKNMTIPYGWAKRPMLQRIGGLHPDIPVSVIFGARS
CIDGNSGTSIQSLRPKSYVKTIAILGAGHYVYADQPEEFNQKVKEICHTVD

Figure 53: ***Sequencing result of murine mCGI-58-mCherry wild-type cloned in vector pEYFP-N1.*** *The upper part shows the DNA sequencing result. The number 833A was assigned by the group of Dr. Granneman and is added here for future use in the laboratory. The lower part shows the translated amino acid sequence.*

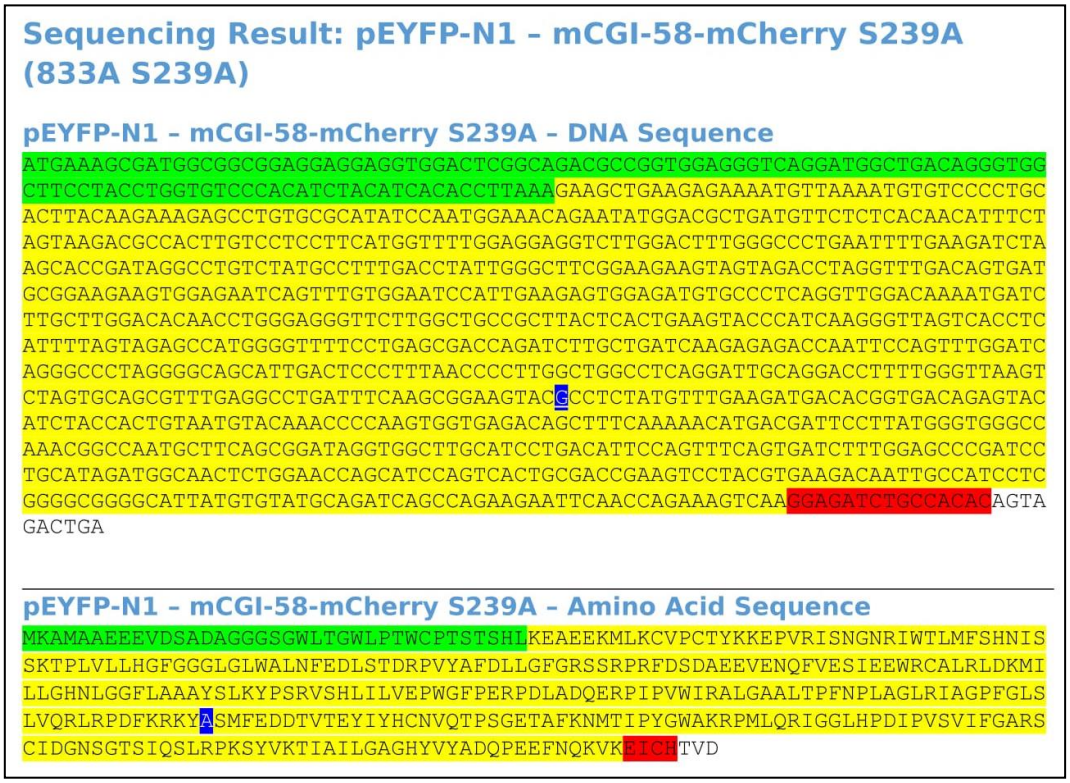

Sequencing Result: pEYFP-N1 – mCGI-58-mCherry S239A (833A S239A)

pEYFP-N1 – mCGI-58-mCherry S239A – DNA Sequence

ATGAAAGCGATGGCGGCGGAGGAGGAGGTGGACTCGGCAGACGCCGGTGGAGGGTCAGGATGGCTGACAGGGTGG
CTTCCTACCTGGTGTCCCACATCTACATCACACCTTAAAGAAGCTGAAGAGAAAATGTTAAAATGTGTCCCCTGC
ACTTACAAGAAAGAGCCTGTGCGCATATCCAATGGAAACAGAATATGGACGCTGATGTTCTCTCACAACATTTCT
AGTAAGACGCCACTTGTCCTCCTTCATGGTTTTGGAGGAGGTCTTGGACTTTGGGCCCTGAATTTTGAAGATCTA
AGCACCGATAGGCCTGTCTATGCCTTTGACCTATTGGGCTTCGGAAGAAGTAGTAGACCTAGGTTTGACAGTGAT
GCGGAAGAAGTGGAGAATCAGTTTGTGGAATCCATTGAAGAGTGGAGATGTGCCCTCAGGTTGGACAAAATGATC
TTGCTTGGACACAACCTGGGAGGGTTCTTGGCTGCCGCTTACTCACTGAAGTACCCATCAAGGGTTAGTCACCTC
ATTTTAGTAGAGCCATGGGGTTTTCCTGAGCGACCAGATCTTGCTGATCAAGAGAGACCAATTCCAGTTTGGATC
AGGGCCCTAGGGGCAGCATTGACTCCCTTTAACCCCTTGGCTGGCCTCAGGATTGCAGGACCTTTTGGGTTAAGT
CTAGTGCAGCGTTTGAGGCCTGATTTCAAGCGGAAGTACGCCTCTATGTTTGAAGATGACACGGTGACAGAGTAC
ATCTACCACTGTAATGTACAAACCCCAAGTGGTGAGACAGCTTTCAAAAACATGACGATTCCTTATGGGTGGGCC
AAACGGCCAATGCTTCAGCGGATAGGTGGCTTGCATCCTGACATTCCAGTTTCAGTGATCTTTGGAGCCCGATCC
TGCATAGATGGCAACTCTGGAACCAGCATCCAGTCACTGCGACCGAAGTCCTACGTGAAGACAATTGCCATCCTC
GGGGCGGGGCATTATGTGTATGCAGATCAGCCAGAAGAATTCAACCAGAAAGTCAAGGAGATCTGCCACACAGTA
GACTGA

pEYFP-N1 – mCGI-58-mCherry S239A – Amino Acid Sequence

MKAMAAEEEVDSADAGGGSGWLTGWLPTWCPTSTSHLKEAEEKMLKCVPCTYKKEPVRISNGNRIWTLMFSHNIS
SKTPLVLLHGFGGGLGLWALNFEDLSTDRPVYAFDLLGFGRSSRPRFDSDAEEVENQFVESIEEWRCALRLDKMI
LLGHNLGGFLAAAYSLKYPSRVSHLILVEPWGFPERPDLADQERPIPVWIRALGAALTPFNPLAGLRIAGPFGLS
LVQRLRPDFKRKYASMFEDDTVTEYIYHCNVQTPSGETAFKNMTIPYGWAKRPMLQRIGGLHPDIPVSVIFGARS
CIDGNSGTSIQSLRPKSYVKTIAILGAGHYVYADQPEEFNQKVKEICHTVD

Figure 54: ***Sequencing result of murine mCGI-58-mCherry S239A cloned in vector pEYFP-N1.*** *The upper part shows the DNA sequencing result. The number 833A was assigned by the group of Dr. Granneman and is added here for future use in the laboratory. The lower part shows the translated amino acid sequence.*

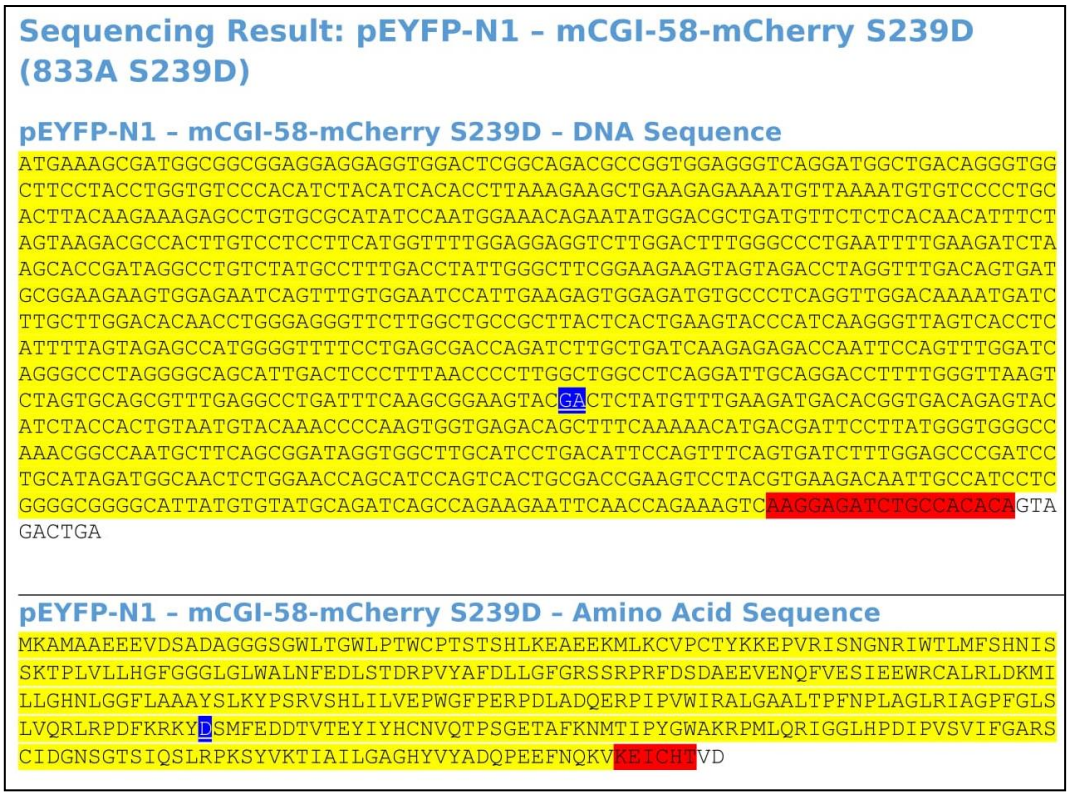

Figure 55: ***Sequencing result of murine mCGI-58-mCherry S239D cloned in vector pEYFP-N1.*** *The upper part shows the DNA sequencing result. The number 833A was assigned by the group of Dr. Granneman and is added here for future use in the laboratory. The lower part shows the translated amino acid sequence.*

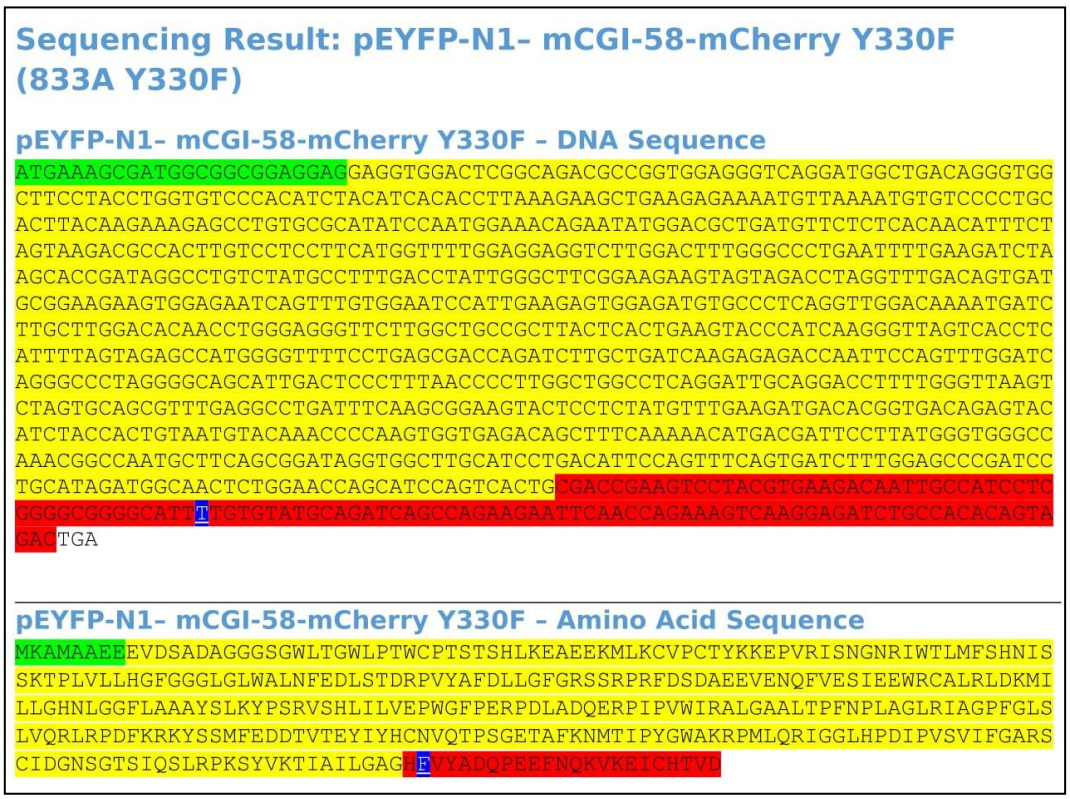

Figure 56: ***Sequencing result of murine mCGI-58-mCherry Y330F cloned in vector pEYFP-N1.*** *The upper part shows the DNA sequencing result. The number 833A was assigned by the group of Dr. Granneman and is added here for future use in the laboratory. The lower part shows the translated amino acid sequence.*

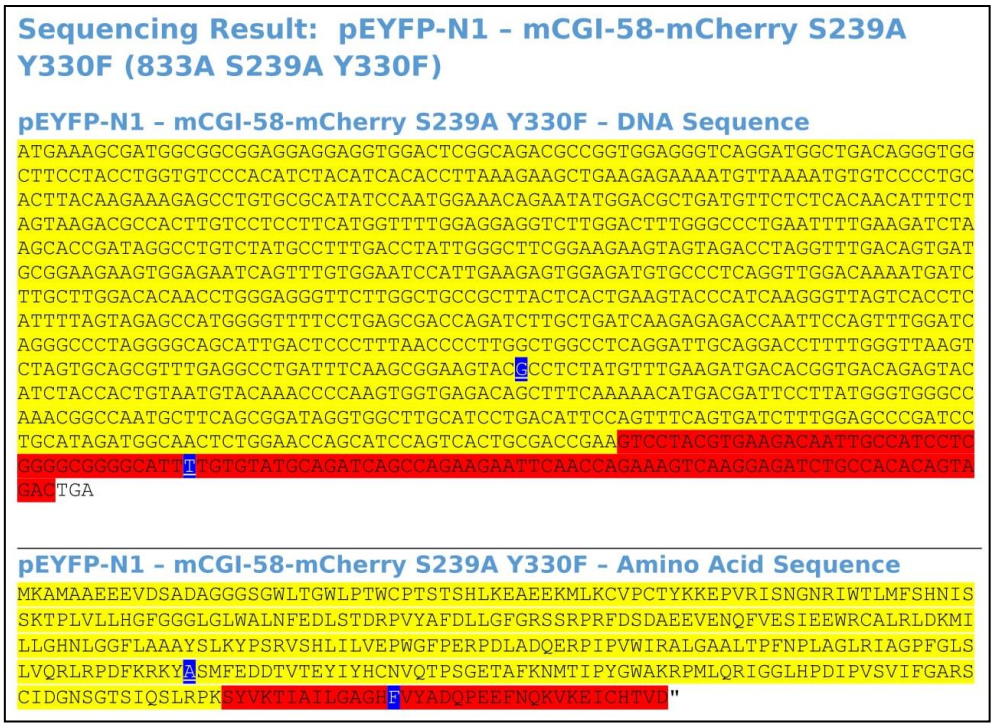

Sequencing Result: pEYFP-N1 – mCGI-58-mCherry S239A Y330F (833A S239A Y330F)

pEYFP-N1 – mCGI-58-mCherry S239A Y330F – DNA Sequence

ATGAAAGCGATGGCGGCGGAGGAGGAGGTGGACTCGGCAGACGCCGGTGGAGGGTCAGGATGGCTGACAGGGTGG
CTTCCTACCTGGTGTCCCACATCTACATCACACCTTAAAGAAGCTGAAGAGAAAATGTTAAAATGTGTCCCCTGC
ACTTACAAGAAAGAGCCTGTGCGCATATCCAATGGAAACAGAATATGGACGCTGATGTTCTCTCACAACATTTCT
AGTAAGACGCCACTTGTCCTCCTTCATGGTTTTGGAGGAGGTCTTGGACTTTGGGCCCTGAATTTTGAAGATCTA
AGCACCGATAGGCCTGTCTATGCCTTTGACCTATTGGGCTTCGGAAGAAGTAGTAGACCTAGGTTTGACAGTGAT
GCGGAAGAAGTGGAGAATCAGTTTGTGGAATCCATTGAAGAGTGGAGATGTGCCCTCAGGTTGGACAAAATGATC
TTGCTTGGACACAACCTGGGAGGGTTCTTGGCTGCCGCTTACTCACTGAAGTACCCATCAAGGGTTAGTCACCTC
ATTTTAGTAGAGCCATGGGGTTTTCCTGAGCGACCAGATCTTGCTGATCAAGAGAGACCAATTCCAGTTTGGATC
AGGGCCCTAGGGGCAGCATTGACTCCCTTTAACCCCTTGGCTGGCCTCAGGATTGCAGGACCTTTTGGGTTAAGT
CTAGTGCAGCGTTTGAGGCCTGATTTCAAGCGGAAGTACGCCTCTATGTTTGAAGATGACACGGTGACAGAGTAC
ATCTACCACTGTAATGTACAAACCCCAAGTGGTGAGACAGCTTTCAAAAACATGACGATTCCTTATGGGTGGGCC
AAACGGCCAATGCTTCAGCGGATAGGTGGCTTGCATCCTGACATTCCAGTTTCAGTGATCTTTGGAGCCCGATCC
TGCATAGATGGCAACTCTGGAACCAGCATCCAGTCACTGCGACCGAAGTCCTACGTGAAGACAATTGCCATCCTC
GGGGCGGGGCATTTTGTGTATGCAGATCAGCCAGAAGAATTCAACCAGAAAGTCAAGGAGATCTGCCACACAGTA
GACTGA

pEYFP-N1 – mCGI-58-mCherry S239A Y330F – Amino Acid Sequence

MKAMAAEEEVDSADAGGGSGWLTGWLPTWCPTSTSHLKEAEEKMLKCVPCTYKKEPVRISNGNRIWTLMFSHNIS
SKTPLVLLHGFGGGLGLWALNFEDLSTDRPVYAFDLLGFGRSSRPRFDSDAEEVENQFVESIEEWRCALRLDKMI
LLGHNLGGFLAAAYSLKYPSRVSHLILVEPWGFPERPDLADQERPIPVWIRALGAALTPFNPLAGLRIAGPFGLS
LVQRLRPDFKRKYASMFEDDTVTEYIYHCNVQTPSGETAFKNMTIPYGWAKRPMLQRIGGLHPDIPVSVIFGARS
CIDGNSGTSIQSLRPKSYVKTIAILGAGHFVYADQPEEFNQKVKEICHTVD"

Figure 57: ***Sequencing result of murine mCGI-58-mCherry S239A Y330F cloned in vector pEYFP-N1.*** *The upper part shows the DNA sequencing result. The number 833A was assigned by the group of Dr. Granneman and is added here for future use in the laboratory. The lower part shows the translated amino acid sequence.*

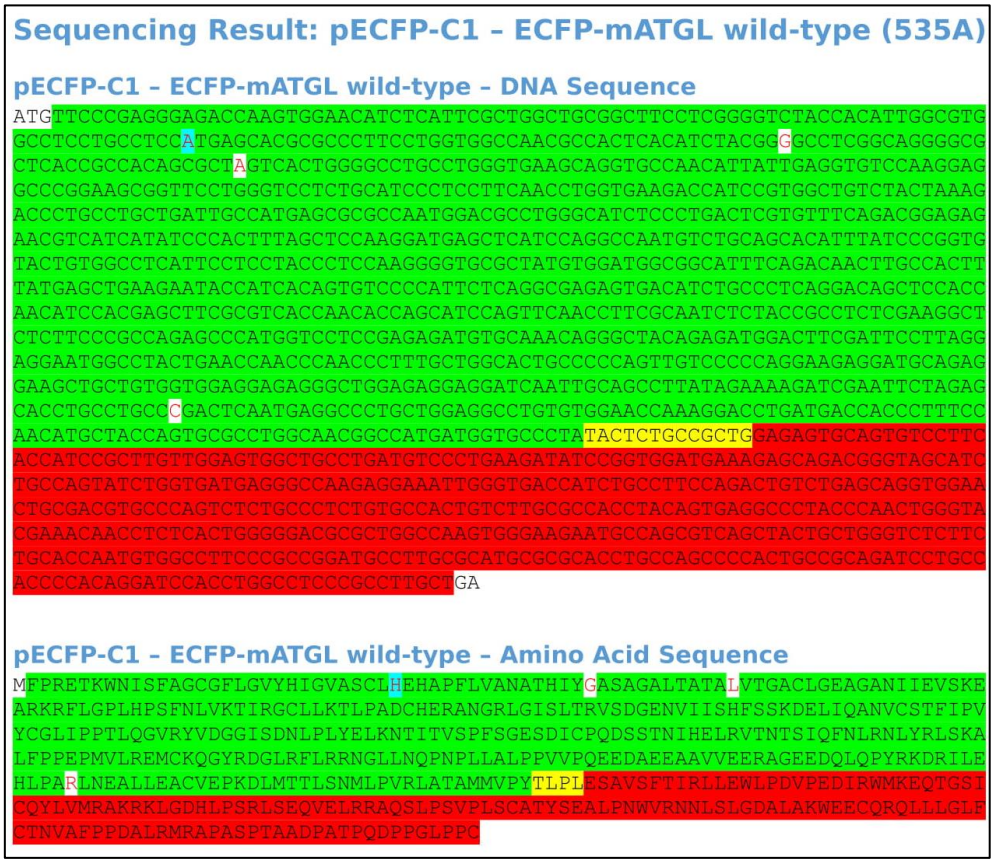

Sequencing Result: pECFP-C1 – ECFP-mATGL wild-type (535A)

pECFP-C1 – ECFP-mATGL wild-type – DNA Sequence

ATGGTTCCCGAGGGAGACCAAGTGGAACATCTCATTCGCTGGCTGCGGCTTCCTCGGGGTCTACCACATTGGCGTG
GCCTCCTGCCTCCATGAGCACGCGCCCTTCCTGGTGGCCAACGCCACTCACATCTACGGGGCCTCGGCAGGGGCG
CTCACCGCCACAGCGCTAGTCACTGGGGCCTGCCTGGGTGAAGCAGGTGCCAACATTATTGAGGTGTCCAAGGAG
GCCCGGAAGCGGTTCCTGGGTCCTCTGCATCCCTCCTTCAACCTGGTGAAGACCATCCGTGGCTGTCTACTAAAG
ACCCTGCCTGCTGATTGCCATGAGCGCGCCAATGGACGCCTGGGCATCTCCCTGACTCGTGTTTCAGACGGAGAG
AACGTCATCATATCCCACTTTAGCTCCAAGGATGAGCTCATCCAGGCCAATGTCTGCAGCACATTTATCCCGGTG
TACTGTGGCCTCATTCCTCCTACCCTCCAAGGGGTGCGCTATGTGGATGGCGGCATTTCAGACAACTTGCCACTT
TATGAGCTGAAGAATACCATCACAGTGTCCCCATTCTCAGGCGAGAGTGACATCTGCCCTCAGGACAGCTCCACC
AACATCCACGAGCTTCGCGTCACCAACACCAGCATCCAGTTCAACCTTCGCAATCTCTACCGCCTCTCGAAGGCT
CTCTTCCCGCCAGAGCCCATGGTCCTCCGAGAGATGTGCAAACAGGGCTACAGAGATGGACTTCGATTCCTTAGG
AGGAATGGCCTACTGAACCAACCCAACCCTTTGCTGGCACTGCCCCCAGTTGTCCCCCAGGAAGAGGATGCAGAG
GAAGCTGCTGTGGTGGAGGAGAGGGCTGGAGAGGAGGATCAATTGCAGCCTTATAGAAAAGATCGAATTCTAGAG
CACCTGCCTGCCCGACTCAATGAGGCCCTGCTGGAGGCCTGTGTGGAACCAAAGGACCTGATGACCACCCTTTCC
AACATGCTACCAGTGCGCCTGGCAACGGCCATGATGGTGCCCTATACTCTGCCGCTGGAGAGTGCAGTGTCCTTG
ACCATCCGCTTGTTGGAGTGGCTGCCTGATGTCCCTGAAGATATCCGGTGGATGAAAGAGCAGACGGGTAGCATC
TGCCAGTATCTGGTGATGAGGGCCAAGAGGAAATTGGGTGACCATCTGCCTTCCAGACTGTCTGAGCAGGTGGAA
CTGCGACGTGCCCAGTCTCTGCCCTCTGTGCCACTGTCTTGCGCCACCTACAGTGAGGCCCTACCCAACTGGGTA
CGAAACAACCTCTCACTGGGGGACGCGCTGGCCAAGTGGGAAGAATGCCAGCGTCAGCTACTGCTGGGTCTCTTC
TGCACCAATGTGGCCTTCCCGCCGGATGCCTTGCGCATGCGCGCACCTGCCAGCCCCACTGCCGCAGATCCTGCC
ACCCCACAGGATCCACCTGGCCTCCCGCCTTGCTGA

pECFP-C1 – ECFP-mATGL wild-type – Amino Acid Sequence

MFPRETKWNISFAGCGFLGVYHIGVASCLHEHAPFLVANATHIYGASAGALTATALVTGACLGEAGANIIEVSKE
ARKRFLGPLHPSFNLVKTIRGCLLKTLPADCHERANGRLGISLTRVSDGENVIISHFSSKDELIQANVCSTFIPV
YCGLIPPTLQGVRYVDGGISDNLPLYELKNTITVSPFSGESDICPQDSSTNIHELRVTNTSIQFNLRNLYRLSKA
LFPPEPMVLREMCKQGYRDGLRFLRRNGLLNQPNPLLALPPVVPQEEDAEEAAVVEERAGEEDQLQPYRKDRILE
HLPARLNEALLEACVEPKDLMTTLSNMLPVRLATAMMVPYTLPLESAVSFTIRLLEWLPDVPEDIRWMKEQTGSI
CQYLVMRAKRKLGDHLPSRLSEQVELRRAQSLPSVPLSCATYSEALPNWVRNNLSLGDALAKWEECQRQLLLGLF
CTNVAFPPDALRMRAPASPTAADPATPQDPPGLPPC

Figure 58: ***Sequencing result of murine ECFP-ATGL wild-type cloned in vector pECFP-C1.*** *The upper part shows the DNA sequencing result. The number 535A was assigned by the group of Dr. Granneman and is added here for future use in the laboratory. The lower part shows the translated amino acid sequence.*

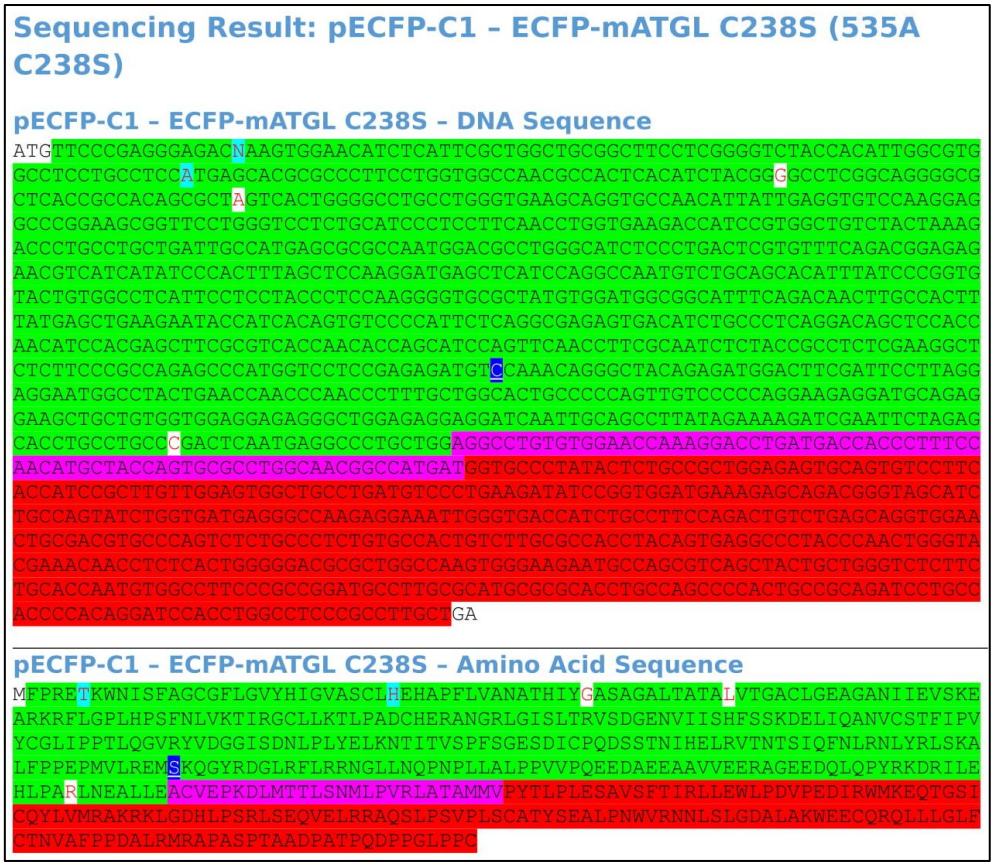

Figure 59: ***Sequencing result of murine ECFP-ATGL C238S cloned in vector pEYCP-C1.*** *The upper part shows the DNA sequencing result. The number 535A was assigned by the group of Dr. Granneman and is added here for future use in the laboratory. The lower part shows the translated amino acid sequence.*

Figure 60: ***Sequencing result of murine Plin1-EYFP A508T Q512L cloned in vector pEYFP-N1.*** *The upper part shows the DNA sequencing result. The number 602A was assigned by the group of Dr. Granneman and is added here for future use in the laboratory. The lower part shows the translated amino acid sequence.*

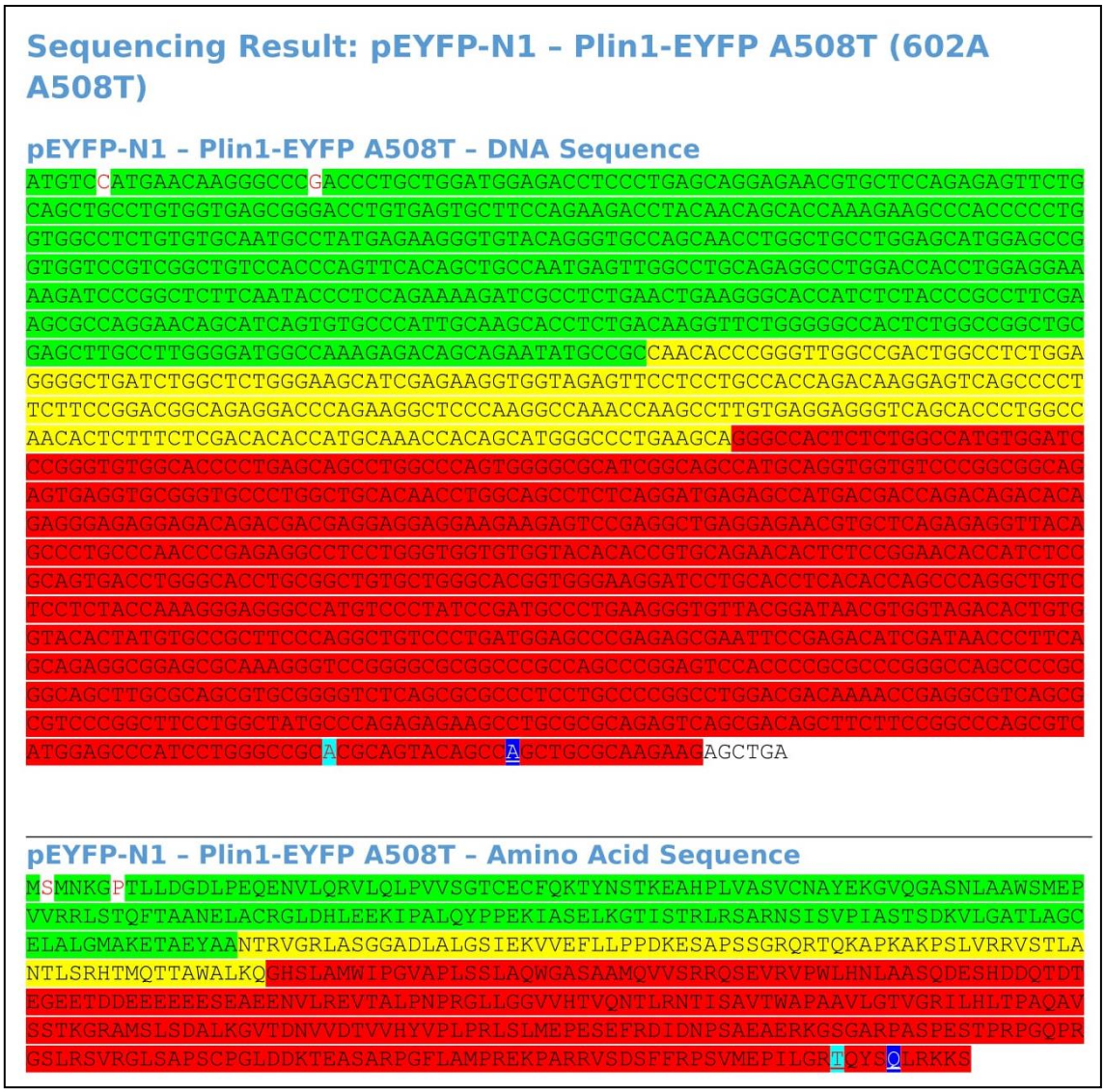

*Figure 61: **Sequencing result of murine Plin1-EYFP A508T cloned in vector pEYFP-N1.** The upper part shows the DNA sequencing result. The number 602A was assigned by the group of Dr. Granneman and is added here for future use in the laboratory. The lower part shows the translated amino acid sequence.*

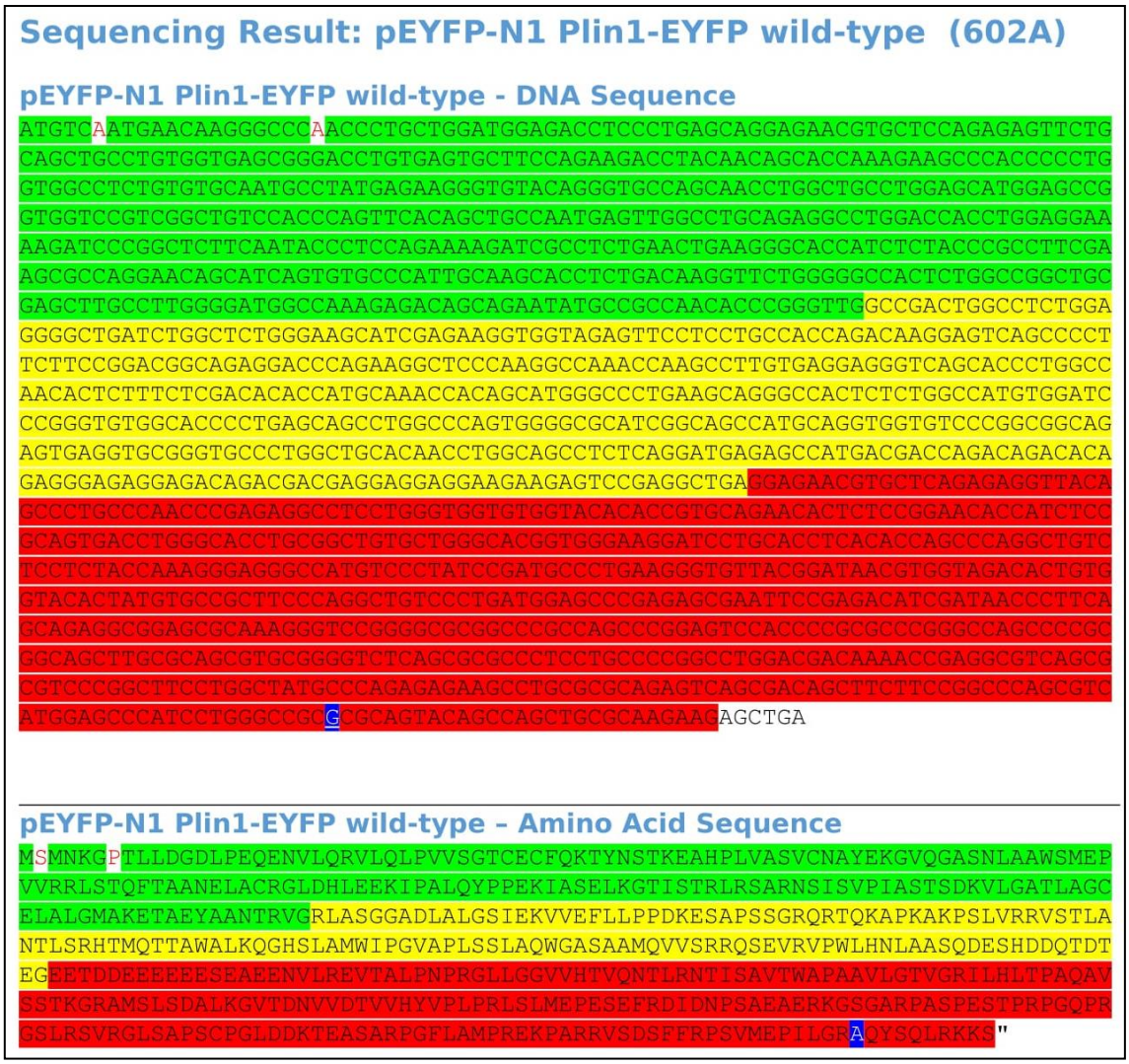

Figure 62: ***Sequencing result of murine Plin1-EYFP wild-type cloned in vector pEYFP-N1.*** *The upper part shows the DNA sequencing result. The number 602A was assigned by the group of Dr. Granneman and is added here for future use in the laboratory. The lower part shows the translated amino acid sequence.*

*Figure 63: **Sequencing result of murine Plin1-EYFP S433A S492A S517A cloned in vector pEYFP-N1**. The upper part shows the DNA sequencing result. The number 771A was assigned by the group of Dr. Granneman and is added here for future use in the laboratory. The lower part shows the translated amino acid sequence.*

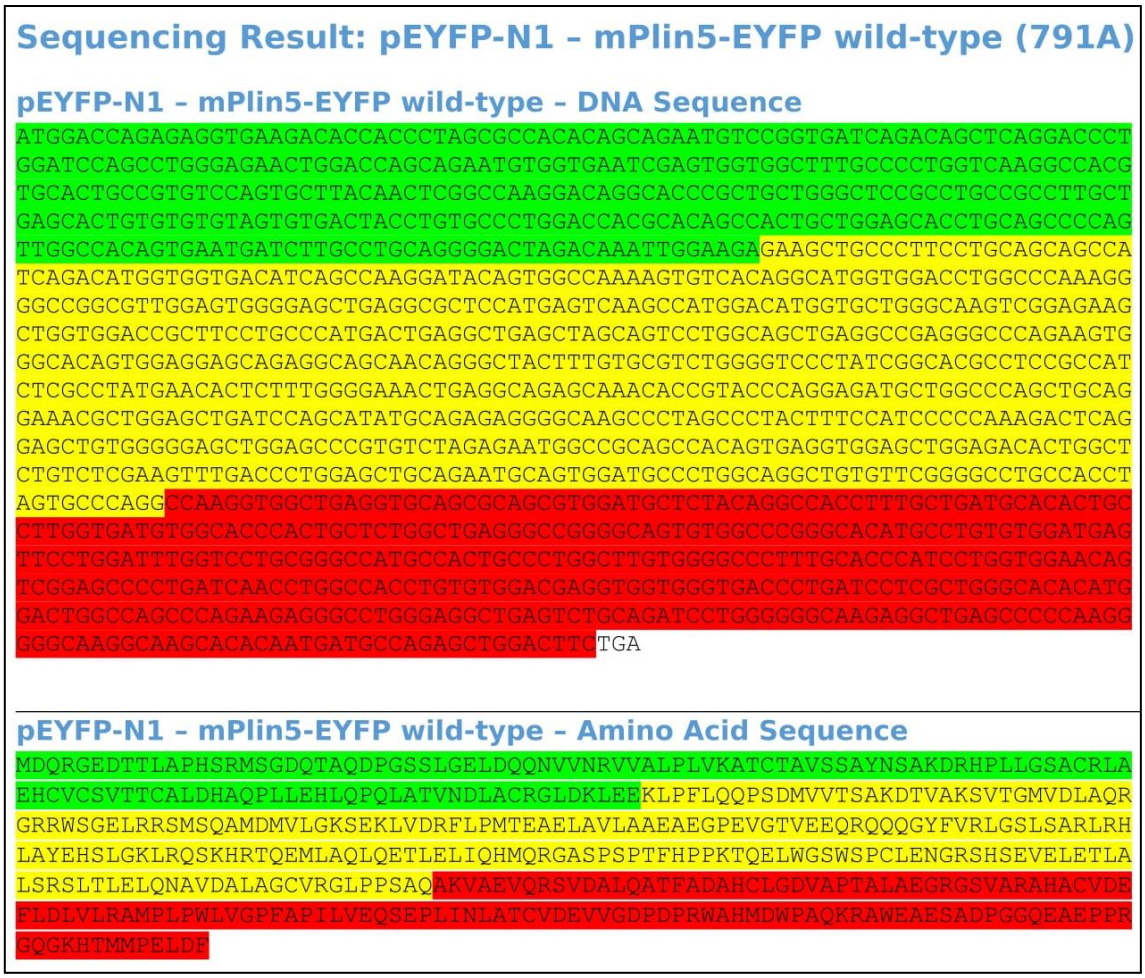

Figure 64: ***Sequencing result of murine Plin5-EYFP wild-type cloned in vector pEYFP-N1.*** *The upper part shows the DNA sequencing result. The number 791A was assigned by the group of Dr. Granneman and is added here for future use in the laboratory. The lower part shows the translated amino acid sequence.*

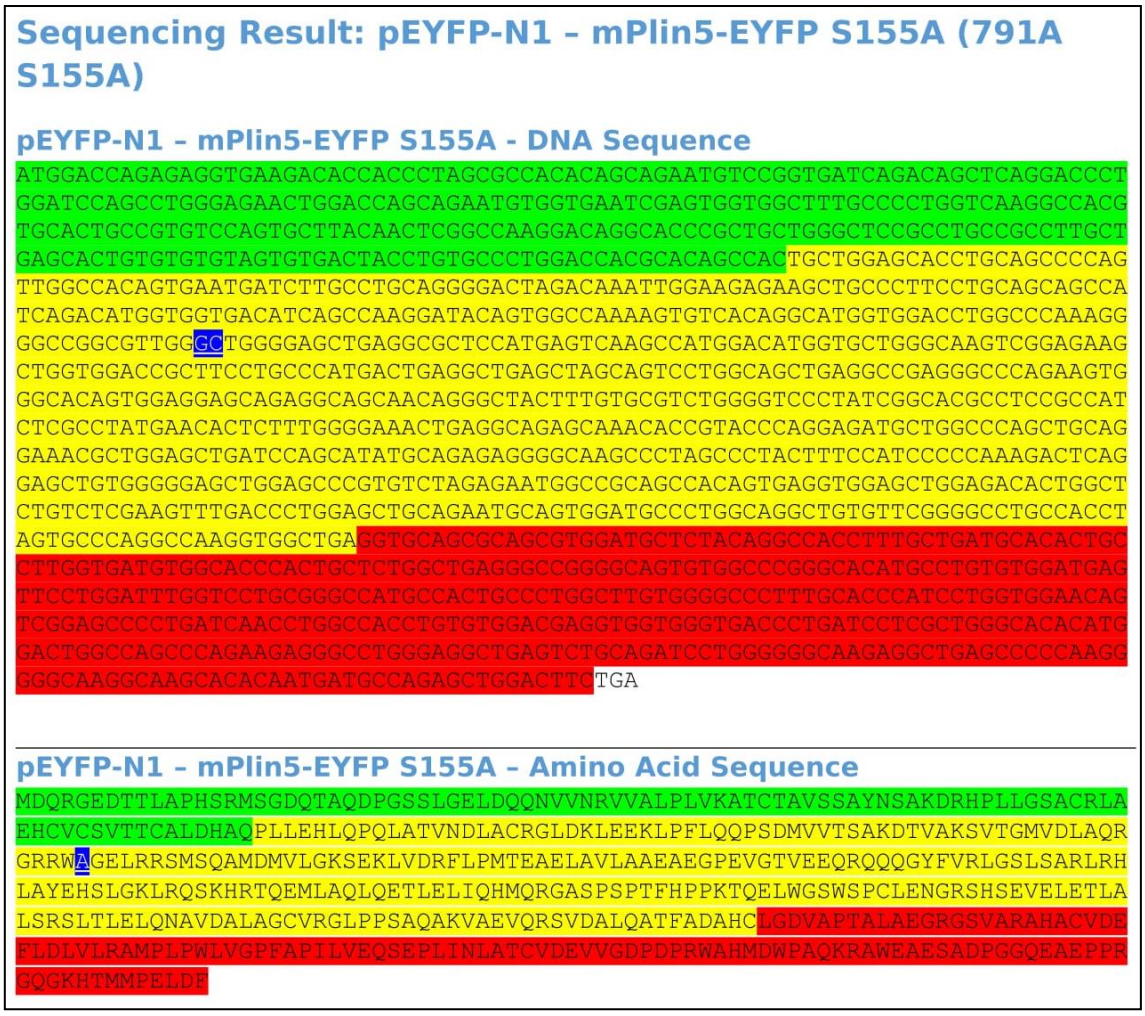

Sequencing Result: pEYFP-N1 – mPlin5-EYFP S155A (791A S155A)

pEYFP-N1 – mPlin5-EYFP S155A - DNA Sequence

```
ATGGACCAGAGAGGTGAAGACACCACCCTAGCGCCACACAGCAGAATGTCCGGTGATCAGACAGCTCAGGACCCT
GGATCCAGCCTGGGAGAACTGGACCAGCAGAATGTGGTGAATCGAGTGGTGGCTTTGCCCCTGGTCAAGGCCACG
TGCACTGCCGTGTCCAGTGCTTACAACTCGGCCAAGGACAGGCACCCGCTGCTGGGCTCCGCCTGCCGCCTTGCT
GAGCACTGTGTGTGTAGTGTGACTACCTGTGCCCTGGACCACGCACAGCCACTGCTGGAGCACCTGCAGCCCCAG
TTGGCCACAGTGAATGATCTTGCCTGCAGGGGACTAGACAAATTGGAAGAGAAGCTGCCCTTCCTGCAGCAGCCA
TCAGACATGGTGGTGACATCAGCCAAGGATACAGTGGCCAAAAGTGTCACAGGCATGGTGGACCTGGCCCAAAGG
GGCCGGCGTTGGGCTGGGGAGCTGAGGCGCTCCATGAGTCAAGCCATGGACATGGTGCTGGGCAAGTCGGAGAAG
CTGGTGGACCGCTTCCTGCCCATGACTGAGGCTGAGCTAGCAGTCCTGGCAGCTGAGGCCGAGGGCCCAGAAGTG
GGCACAGTGGAGGAGCAGAGGCAGCAACAGGGCTACTTTGTGCGTCTGGGGTCCCTATCGGCACGCCTCCGCCAT
CTCGCCTATGAACACTCTTTGGGGAAACTGAGGCAGAGCAAACACCGTACCCAGGAGATGCTGGCCCAGCTGCAG
GAAACGCTGGAGCTGATCCAGCATATGCAGAGAGGGGCAAGCCCTAGCCCTACTTTCCATCCCCCAAAGACTCAG
GAGCTGTGGGGGAGCTGGAGCCCGTGTCTAGAGAATGGCCGCAGCCACAGTGAGGTGGAGCTGGAGACACTGGCT
CTGTCTCGAAGTTTGACCCTGGAGCTGCAGAATGCAGTGGATGCCCTGGCAGGCTGTGTTCGGGGCCTGCCACCT
AGTGCCCAGGCCAAGGTGGCTGAGGTGCAGCGCAGCGTGGATGCTCTACAGGCCACCTTTGCTGATGCACACTGC
CTTGGTGATGTGGCACCCACTGCTCTGGCTGAGGGCCGGGGCAGTGTGGCCCGGGCACATGCCTGTGTGGATGAG
TTCCTGGATTTGGTCCTGCGGGCCATGCCACTGCCCTGGCTTGTGGGGCCCTTTGCACCCATCCTGGTGGAACAG
TCGGAGCCCCTGATCAACCTGGCCACCTGTGTGGACGAGGTGGTGGGTGACCCTGATCCTCGCTGGGCACACATG
GACTGGCCAGCCCAGAAGAGGGCCTGGGAGGCTGAGTCTGCAGATCCTGGGGGGCAAGAGGCTGAGCCCCCAAGG
GGGCAAGGCAAGCACACAATGATGCCAGAGCTGGACTTCTGA
```

pEYFP-N1 – mPlin5-EYFP S155A - Amino Acid Sequence

```
MDQRGEDTTLAPHSRMSGDQTAQDPGSSLGELDQQNVVNRVVALPLVKATCTAVSSAYNSAKDRHPLLGSACRLA
EHCVCSVTTCALDHAQPLLEHLQPQLATVNDLACRGLDKLEEKLPFLQQPSDMVVTSAKDTVAKSVTGMVDLAQR
GRRWAGELRRSMSQAMDMVLGKSEKLVDRFLPMTEAELAVLAAEAEGPEVGTVEEQRQQQGYFVRLGSLSARLRH
LAYEHSLGKLRQSKHRTQEMLAQLQETLELIQHMQRGASPSPTFHPPKTQELWGSWSPCLENGRSHSEVELETLA
LSRSLTLELQNAVDALAGCVRGLPPSAQAKVAEVQRSVDALQATFADAHCLGDVAPTALAEGRGSVARAHACVDE
FLDLVLRAMPLPWLVGPFAPILVEQSEPLINLATCVDEVVGDPDPRWAHMDWPAQKRAWEAESADPGGQEAEPPR
GQGKHTMMPELDF
```

Figure 65: ***Sequencing result of murine Plin5-EYFP S155A cloned in vector pEYFP-N1****. The upper part shows the DNA sequencing result. The number 791A was assigned by the group of Dr. Granneman and is added here for future use in the laboratory. The lower part shows the translated amino acid sequence.*

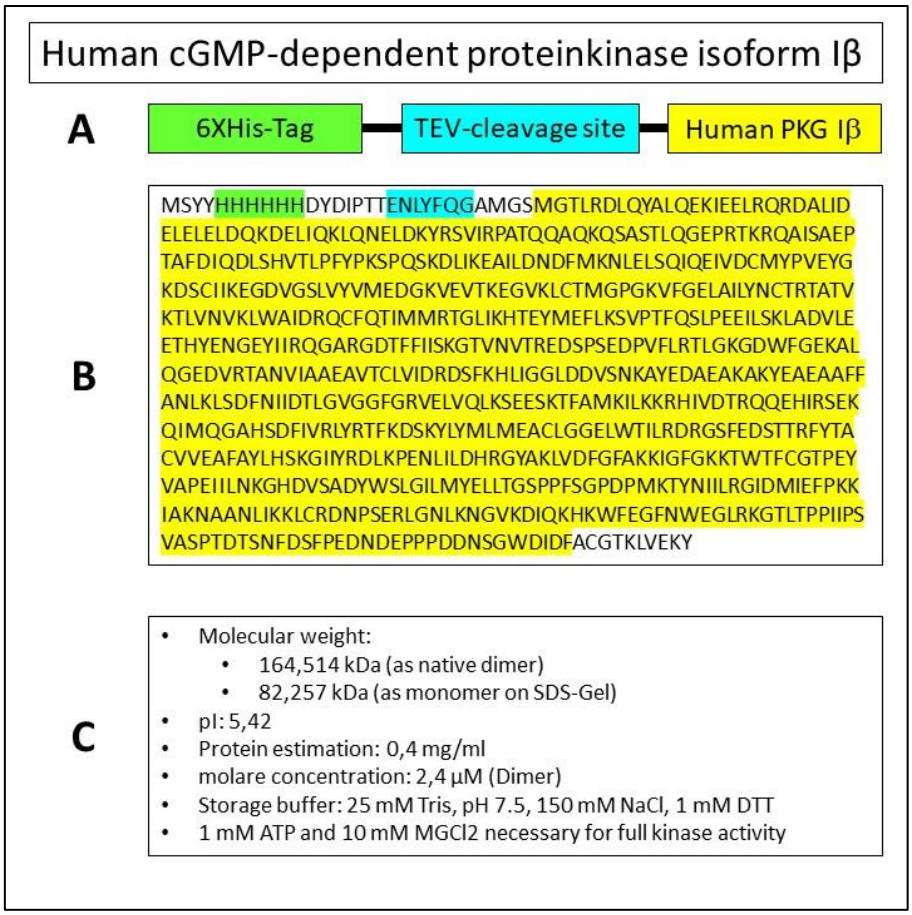

Figure 66: ***Additional information to human cGMP-dependent proteinkinase (PKG) provided by Dr. D. Bertinetti A*** *basic protein structure of PKG* ***B*** *Amino acid sequence of PKG* ***C*** *Properties of PKG*